Bachelor Thesis

Bachelor's degree in Industrial Technologies Engineering
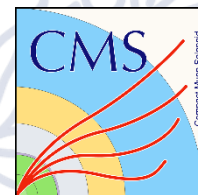
Mechanical Design of the HGCal Wedges with Thermal Gradient

Thesis

Author: Teresa Ramos García

Directors: Hubert Gerwig (CERN)

              Jordi Guilera (ETSEIB)

Semester: September 2021 – February 2022

Submission date: January 22, 2022

ETSEIB

Barcelona School of Industrial
Engineering

UPC

CMS

European Organisation
for Nuclear Research

CERN

Declaration

I hereby declare that I have written the presented thesis on my own and without any help from others. Text passages that are based literally or in meaning on publications or lectures of other authors are marked as such.

The paper has not yet been submitted to any other examination authority and has not yet been published.

Meyrin, 22.01.22

Maria Teresa RAMOS GARCIA

Acknowledgements

Abstract

After the discovery of the Higgs Boson, the purpose of the world's largest and most powerful particle accelerator, the Large Hadron Collider (LHC), seemed to have been achieved. Despite the fact that the Standard Model apparently complies with most experimental data up to this day, the majority of particle physicists feel that it is not a complete framework [1]. Therefore, there are still many unresolved problems in the physics of elementary particles. That is the reason why, in 2013, the European Strategy for Particle Physics announced its update.

The High-Luminosity Large Hadron Collider (HL-LHC) project aims to increase luminosity by a factor of 10 beyond the LHC's design. The higher the luminosity, the more data the experiments can gather to allow scientists to observe rare processes. Its development depends on several technological innovations, like the High-Granularity Calorimeter (HGCal), a major upgrade of the Compact Muon Solenoid (CMS) detector. [2]

This project analyses the design and optimisation processes of the supports (wedges) which join the calorimeter (HGCal) to the related parts of the CMS detector. Specifically, the study focuses on the intermediate wedges. The main challenge is to create an optimal configuration for both the operational (vertical) and the assembly (horizontal) position. For this reason, a series of mechanical, magnetic and thermal considerations must be taken into account. This includes withstanding a mass of 200 tons and 50 $°C$ of thermal difference.

In order to achieve this goal, it is first necessary to analyse the functionality of the detector. This in-depth research allows a precise problem definition. Later, the preliminary design of the intermediate wedges is studied. By analysing the finite element results, the optimisation steps are established. At the end, the final version, the results of its analyses and some suggestions for the building process are presented.

In the final result analyses, a hybrid configuration of fixed and hinged intermediate wedges was presented. In the operational position, stresses and vertical load values were lowered. In addition, a thermal analysis concluded that the heat transfer was sufficient for meeting the given requirements. In the assembly analysis, it was verified that the supports are not buckling or permanently deforming.

Abstracto

Después del descubrimiento del bosón de Higgs, el propósito del acelerador de partículas más grande y potente del mundo, el *Large Hadron Collider* (LHC), parecía haberse logrado. A pesar de que el modelo estándar aparentemente cumple con la mayoría de los datos experimentales conocidos hasta la fecha, la mayoría de los físicos de partículas presienten que no es un marco completo [1]. Por lo tanto, todavía quedan muchos problemas sin resolver en la física de partículas elementales y, en 2013, la Estrategia Europea para la Física de Partículas anunció su actualización.

El proyecto *High-Luminosity Large Hadron Collider* (HL-LHC) tiene como objetivo aumentar la luminosidad en un factor de 10 respecto la del LHC. Cuanto mayor sea la luminosidad, más datos pueden recopilar los experimentos para permitir a los científicos observar procesos raros. Su desarrollo depende de varias innovaciones tecnológicas, como el *High-Granularity Calorimeter* (HGCal), una importante actualización del detector *Compact Muon Solenoid* (CMS). [2]

Este proyecto analiza los procesos de diseño y optimización de los soportes (*wedges*) que unen el calorímetro (HGCal) al resto del detector CMS. En concreto, el estudio se centra en los *intermediate wedges*. El principal desafío es crear una configuración óptima tanto para la posición operativa (vertical) como para la de ensamblaje (horizontal). Por ello, se deben tener en cuenta una serie de consideraciones mecánicas, magnéticas y térmicas. Esto incluye soportar una masa de 200 toneladas y 50 °C de diferencia térmica.

Para lograr este objetivo, primero es necesario investigar el funcionamiento de los detectores. Esto permite definir el problema. Posteriormente, se estudia el diseño preliminar y, analizando los resultados de los elementos finitos, se establecen los pasos de la optimización. Para acabar, se expone la versión final, los resultados de sus análisis y algunas sugerencias para su construcción.

Durante los análisis definitivos, se presentó una configuración híbrida de cuñas fijas y articuladas. En la posición operativa, se redujeron los valores de tensión y carga vertical. Además, un análisis térmico concluyó que la transferencia de calor era lo suficientemente buena. En el de montaje, se comprobó que los soportes no pandearán ni se deformarán permanentemente.

Contents

1. Glossary

1.1. List of Figures

1.2.   List of Tables

1.3.   Acronyms

ADP	Abiotic Depletion Potential
ALICE	A Large Ion Collider Experiment
AP	Acidification Potential
ATLAS	A Toroidal LHC ApparatuS
CAD	Computer-Aided Design
CE-E	Electromagnetic compartment
CE-H	Hadronic compartment
CERN	European Organisation for Nuclear Research
CMS	Compact Muon Solenoid detector
CNC	Computer Numerical Control
DC	Direct Current
ECAL	Electromagnetic Calorimeter
EP	Eutrophication Potential
ETL	Endcap Timing Layer
FEA	Finite Element Analysis
FEM	Finite Element Method
FHVX	Fixed-Hinged Version X (X is a number)
FVX	Fixed Version X (X is a number)
GWP100	Global Warming Potential
HCAL	Hadronic Calorimeter
HGCal	High-Granularity Calorimeter
HL-LHC	High-Luminosity Large Hadron Collider
HTP	Human Toxicity Potential
HV	High-Voltage
HVX	Hinged Version X (X is a number)
LCA	Life Cycle Analysis
LHC	Large Hadron Collider
LHC-b	LHC-beauty
ME	Muon Endcap
ODP	Ozone Layer Depletion Potential
PCB	Printed Circuit Board
PM	Particle Moderator
POCP	Photochemical Ozone Creation Potential
PTFE	Polytetrafluoroethylene
SS	Stainless Steel
SV	Sliding Version
Ti	Titanium alloy
UXC	Underground Collision hall
VOCs	Volatile Organic Compounds
YE	Yoke Endcap

1.4.   List of Symbols

4.1.3. Regulations

γ_s	Load/Safety factor
γ_1	Load factor that covers the model uncertainty of the FEM
γ_2	Load factor that covers the scatter of the loading and resistance models
γ_{M1}	Load factor that covers the scatter of the loading and resistance models when instability governs
γ_{M2}	Load factor that covers the scatter of the loading and resistance models when fracture governs

4.2. Material Selection

ρ	Density
σ	Tensile yield strength
E	Young's modulus
$K_{1.1}$	Index of a uniform cross section bar tested on tension & compression to check the stiffness of a material
$K_{1.2}$	Index of a uniform cross section bar tested on flexion to check the yield strength of a material
$K_{2.1}$	Index of a uniform cross section bar tested on tension & compression to check the stiffness of a material
$K_{2.2}$	Index of a uniform cross section bar tested on flexion to check the yield strength of a material

4.3. Maximum Permissible Force, Dispersion and Characteristic Values

F_{hw_1}	Back disk weight / Compression force supported by the intermediate and 3 & 9 o'clock wedges in the second step of the assembly of the endcap suspension system
F_{hw,i_1}	Force supported by a wedge in the second step of the assembly of the endcap suspension system
F_{hw_2}	Final assembly weight / HGCal self-weight / Compression force supported by all the wedges in the last step of the assembly
F_{hw,i_2}	Force supported by a wedge in the last step of the assembly
F_{hw}	Maximum permissible force in the assembly position (horizontal)
$F_{hw,i}$	Maximum permissible force per wedge in the assembly position (horizontal)
F_{vw}	Final assembly weight / HGCal self-weight / Shear force produced by the self-weight and supported by 3 & 9 o'clock wedges
$F_{sf,3}, F_{sf,9}$	Self-weight supported by 3 & 9 o'clock wedges
M_{vw}	Bending moment produced by the self-weight
$F_{bm,12}, F_{bm,6}$	Bending moment force supported by 12 & 6 o'clock wedges

4.4.2. Prototype Construction

R	Radius
D	Diameter
DIA	Normal Diameter
L	Length
T	Thickness
W	Width
H	Height
C	Clearance

5. Model definition

a_m	Magnetic acceleration
A	Compression force supported by a wedge in the Eigenvalue Buckling hyperstatic analysis
E	Relative error

6. Result Analysis

L	Intermediate wedges' length
$y_{g,i}$	Gravity force Y component of the wedge i
$y_{m,i}$	Magnetic force Y component of the wedge i
F_g	Gravity force
F_m	Magnetic force
F_{x1}, F_{x2}	Force reaction x of surfaces 1 and 2
F_{y1}, F_{y2}	Force reaction y of surfaces 1 and 2
F_{z1}, F_{z2}	Force reaction z of surfaces 1 and 2
R_1, R_2	Resultant force of surface 1 and 2
M_{x1}, M_{x2}	Moment reaction x of surfaces 1 and 2
M_{y1}, M_{y2}	Moment reaction y of surfaces 1 and 2
M_{z1}, M_{z2}	Moment reaction z of surfaces 1 and 2
M_1, M_2	Resultant moment of surface 1 and 2
σ_I, σ_{III}	Principal stresses

7. Design Optimisation

X, Y, Z	X, Y and Z components of the centroid in the Simplified hinged model
x_i, y_i, z_i	X, Y and Z components of the part i centroid in the Simplified hinged model
m_i	Mass of the part i in the Simplified hinged model
P, F	Applied force
R	Reaction force
T, V	Shear force
N	Normal force
M	Applied/ reaction moment
p	Uniformly increasing load
q	Uniformly distributed load
d	Diameter of the pin
e_1	Thickness of the link or arm
e_2	Thickness of the lug or base plate
a	Length of the bonded part of the pin without stress
b	Length of the bonded part of the pin with stress
t_1	Distance between the centre of the pin and the edge of the lug/ link
t_2	Half of the width of the lug/ link
b	Width of the lug/ link
n	Number of shear planes
f_y	Yield strength
$R_{p0.2}$	0.2% offset yield strength
R_{p1}	1% offset yield strength
SF	Safety factor
K_t	Lug/ link constant to calculate maximum stresses
I_z	Moment of inertia
σ_{all}	Equivalent stress allowed
τ_{all}	Shear stress allowed
σ'_{all}	Bearing normal stress allowed
$\tau_{xy, shear}$	Shear stress of the XY plane for shear failure
$\sigma_{y, bearing}$	Normal stress in the Y direction for bearing failure
$\sigma_{x, bending}$	Normal stress in the X direction for bending failure
σ_{eq}	Equivalent stress

8.1. Final Design

A	Thickness of the rod end stem
B	Thickness of the rod end ball
d_1	Outer diameter of the rod end ball
d_2	Outer diameter of the rod end stem
d_3	Rod end male thread
l_1	Rod end male thread length
l_2	Rod end total height
l_3	Rod end height from the ball centroid to the end of the thread
h	Height of the lug/ link
S	Stress surface

2. Introduction

2.1. On the Importance of Modelling and Simulation for Engineering Problem Solving

Modelling and simulation have always played a central role in engineering problem-solving. For engineers, models provide a mechanism for learning about artefacts before and after they have been built. Models are enabling engineers to examine different options and weigh the choices of structural elements, materials and components against one another. However, physical prototypes are expensive and time consuming to create and often unreliable, and digital tools are cost-efficient and easily available. They provide the basis for digital models that assist in abstracting physical phenomena, allowing engineers to experiment, simulate and play with different options whilst engaging with a range of interested parties. This is leading to a new culture of prototyping in which traditional practices of design are being opened to more concurrent diagnostic enquiries. [3]

2.2. Origin of the Project and Motivation

In order to obtain professional experience before finishing my studies, in mid-2020 I started looking for internships in international companies and organisations.

Among them I found the CERN Technical Student Programme, which is offering a practical training period and a position to complete the bachelor or master thesis.

Thanks to my knowledge in ANSYS Workbench, a finite element analysis software, I received an offer for a position in the Integration Engineering department. Here, I focused my project on the design and optimisation processes of several supports using computer-aided design (CAD) and finite element analysis (FEA), modelling and simulating technological platforms.

2.3. Objectives

For a good project performance, the following tasks and objectives are set:

- Learning accelerators and detectors' operation
- Defining the project task
- Studying the existing model and analysis
- Deepening ANSYS knowledge on Static Structural, Eigenvalue Buckling and Thermal analyses
- Optimising the design of the wedges to improve stress and load value distributions
- Comparing analytical and theoretical results and checking their similarity
- Drawing plans of the final design

However, all of them can be summarised in one main goal: developing technical and non-technical designing skills. These skills include analytical, open-ended problem solving, a view for total engineering, interpersonal and team skills, communication skills, as well as fluency with modern tools and techniques used in engineering design [4].

ETSEIB

2.4.   Preliminary Requirements

For the realisation of the project, several subjects of my study program will be linked to the carried-out tasks:

- During the **Continuum Mechanics** course, in groups of three students and the help of a finite element software (ANSYS), a mechanical design project is carried out. Thanks to the report that was planned to be presented together with the prototype of the designed piece, I learnt how these kind of projects are structured. I used this knowledge to organise my thesis.
- In **Numerical Methods** I learnt the mathematical models behind the finite element software. This will help me to choose the mesh element type.
- Thanks to **Strength of Materials,** I will be able to predict where the maximum equivalent stresses are found in simplified beam geometries.
- With the knowledge acquired in some chapters of **Technology and Selection of Materials** and **Manufacturing Systems** I will be able to develop the selection of the material and understand that my designs should respect several limits due to the fabrication technique.
- Finally, in **Engineering Drawing** I learnt how to use SolidWorks.

2.5.   Scope of the Project

By focusing the study on the intermediate wedges, the main scope of this project is to create an optimal configuration for both the operational (vertical) and the assembly (horizontal) position. For this reason, a series of mechanical, magnetic and thermal considerations must be taken into account. This includes withstanding a mass of 200 tons and $50\,°C$ of thermal difference. For this purpose, different models and simulations will be created, enabling to compare the deformation, stresses and force reaction results of the different versions of the intermediate wedges.

3.   About CERN

3.1.   Introduction

Founded in 1954, the European Organisation for Nuclear Research, known as CERN, is a European research organisation that operates the largest particle physics laboratory in the world astride the Franco-Swiss border. [5]

Subatomic particles are made to collide together at velocities close to the speed of light. The process gives us clues about how the particles interact, and provides insights into the fundamental laws of nature. The instruments used are purpose-built **particle accelerators** and **detectors**. [5]

- **Accelerators** boost beams of particles to high energies before the beams are made to collide with each other or with stationary targets. [5]
- **Detectors** observe and record the results of these collisions. [5]

Several important achievements have been made through experiments at CERN such as the discovery of the Higgs boson, the asymmetry problem, the birth of the web, etc. Nowadays, the **High-Luminosity Large Hadron Collider (HL-LHC)** project aims to improve the performance of the LHC in order to study known mechanisms (such as the Higgs boson) in greater detail. [5]

3.2.   The (High-Luminosity) Large Hadron Collider

The **Large Hadron Collider (LHC)** represented in Figure 3.1 is the world's largest and most powerful particle accelerator. It consists of a 27 kilometre ring of superconducting magnets with a number of accelerating structures to boost the energy of the particles along the way. [2]

Inside the accelerator, two high-energy particle beams travel at velocities close to the speed of light before they are made to collide at four locations around the accelerator ring, corresponding to the positions of four particle detectors – A Toroidal LHC ApparatuS (ATLAS), **Compact Muon Solenoid (CMS)**, A Large Ion Collider Experiment (ALICE) and LHC-beauty (LHCb). [6] At these points, the energy of the particle collisions gets transformed into mass, spraying particles in all directions. [2]

It first started up on 10 September 2008 and after several years of discoveries, in 2013 the European Strategy for Particle Physics announced its update. The **High-Luminosity Large Hadron Collider (HL-LHC)** project aims to increase luminosity by a factor of 10 beyond the LHC's design. [2]

Luminosity is an important indicator of the performance of an accelerator: it is proportional to the number of collisions that occur in a given amount of time. The higher the luminosity, the more data the experiments can gather to allow the scientists to observe rare processes. Its development depends on several technological innovations, like the **High-Granularity Calorimeter (HGCal)**, a major upgrade of the **CMS**. [2]

Figure 3.1: LHC Experimental programme *[7]*

3.3.   **The Compact Muon Solenoid Detector**

The content of chapter 3.3 is based upon the following source: [8]

The **Compact Muon Solenoid detector (CMS)** acts as a giant, high-speed camera, taking 3D "photographs" of particle collisions from all directions up to 40 million times each second. Although most of the particles produced in the collisions are "unstable", they transform rapidly into stable particles that can be detected by CMS. By identifying (nearly) all the stable particles produced in each collision, measuring their momenta and energies, and then piecing together the information, the detector can recreate an "image" of the collision for further analysis.
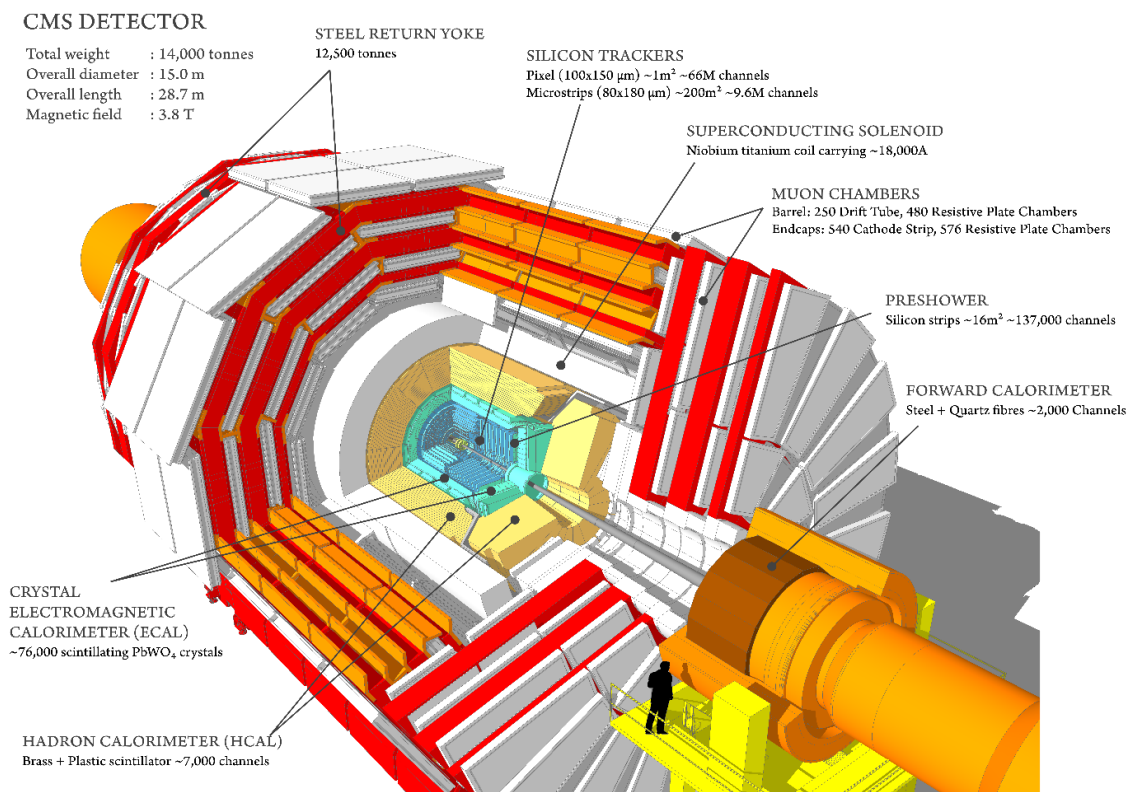
Figure 3.2: CMS detector pieces

3.3.1. Bending Particles

Bending the trajectories of the particles serves two purposes:

1) It helps to identify the charge of the particle: positively and negatively charged particles bend in opposite directions in the same magnetic field.
2) It allows us to measure the momentum of the particle: in an identical magnetic field, high-momentum particles bend less compared to low-momentum ones.

For this reason, a powerful magnet formed by a cylindrical coil of superconducting fibres is needed. When electricity (18,500 A) is circulated within these coils, they encounter no resistance and can generate a magnetic field of around 4 T, which is about 100,000 times the strength of the Earth's magnetic field. This high magnetic field must be confined by the steel "yoke" to the volume of the detector.

The tracker and calorimeter detectors (ECAL and HCAL) fit snugly inside the magnet coil whilst the muon detectors are interleaved with a 12-sided iron structure that surrounds the magnet coils and contains and guides the field. It also provides most of the experiment's structural support, and must be very strong itself to withstand the forces of its own magnetic field.

3.3.2. Identifying Tracks

Momentum of particles is crucial in building up a picture of events at the heart of the collision. One method to calculate the momentum of a particle is to track its path through a magnetic field.

The **CMS tracker,** placed in the inner most part of the detector, is made of around 75 million individual electronic lightweight silicon sensors arranged in concentric layers. It records particle paths by taking position measurements so accurate (10 µm) that tracks can be reliably reconstructed using just a few measurement points. As particles travel through the tracker the pixels and microstrips produce tiny electric signals that are amplified and detected.

3.3.3. Measuring Energy

Information about the energies of the various particles produced in each collision is crucial to understand what is occurring at the collision point. This information is collected from two kinds of "calorimeters" in CMS:

Electromagnetic Calorimeter (ECAL)

The ECAL is the inner layer of the two and measures the energy of electrons and photons by stopping them completely.

It consists of 76,000 lead tungstate crystals, high-density crystals that produce light "scintillates" in fast, short, well-defined photon bursts. Light is proportional to the energy of the particle.

Photodetectors glued onto the back of each of the crystals detect the scintillation light and convert it to an electric signal that is amplified and sent for analysis.

Hadronic Calorimeter (HCAL)

Hadrons, which are composite particles made up of quarks and gluons, fly through the ECAL and are stopped by the outer layer called the HCAL.

As these particles decay, they may produce new particles that do not leave record of their presence in any part of the CMS detector. To spot these, the HCAL must be "hermetic" and built in a staggered configuration so that there are no gaps in direct lines that a familiar particle might escape through. This way if we see particles shoot out one side of the detector, but not the other, with an imbalance in the momentum and energy (measured in the sideways "transverse" direction relative to the beam line), we can deduce that we are producing "invisible" particles.

The HCAL is a sampling calorimeter, meaning it finds a particle's position, energy and arrival time using alternating layers of "absorber" and fluorescent "scintillator" materials that produce a rapid light pulse when the particle passes through (absorber layers produce secondary particles and scintillator ones emit blue-violet light when the shower develops and a particle passes through). Special optic fibres collect this light and feed it into readout boxes where photodetectors amplify the signal. When the amount of light in a given region is summed up over many layers of tiles in depth, called a "tower", this total amount of light is a measurement of the energy of a particle.

3.3.4.   Detecting Muons

The final particle that CMS observes directly is the muon. Muons belong to the same family of particles as electrons, although they are around 200 times heavier. They are not stopped by the calorimeters, so special sub-detectors (**muon chambers**) must be built, interleaved with the return yoke of the solenoid. In total, there are 1,400 muon chambers.

3.4.   The High-Granularity Calorimeter

The content of the chapter 3.4 is based upon the following source: [9]

The HL-LHC will integrate ten times more luminosity than the LHC, posing significant challenges for radiation tolerance and event pileup on detectors, especially for calorimetry in the forward region. As part of its HL-LHC upgrade programme, the CMS Collaboration is proposing to build a **High-Granularity Calorimeter (HGCal)** to replace the existing endcap calorimeters (ECAL and HCAL). This high granularity has potential benefits for the reconstruction of physics objects.

Simulations indicate that high radiation levels will be encountered at the inner radii of the silicon tracker. In order to reliably operate **silicon sensors** after irradiation, and to keep a sufficiently low energy equivalent of electronics noise, they must be operated at -35 °C. Then, the whole calorimeter sits in a thermally shielded volume that will be cooled by a **two-phase CO_2 system** and maintained at −35 °C.

The HGCal (Figure 3.3) consists of an **electromagnetic compartment (CE-E)** followed by a **hadronic compartment (CE-H)**. Design parameter values are summarised in Table 3.1.

Table 3.1: HGCal parameters

	CE-E	CE-H	
	Si	Si	Scintillator
Area (m²)	368	215	487
Channels (k)	3916	1939	389
Si modules (Tileboards)	16008	8868	(3960)
Partial modules	1008	1452	-
Weight (t)	23	205	
Si-only planes	28	8	
Mixed (Si+Scint) planes		16	
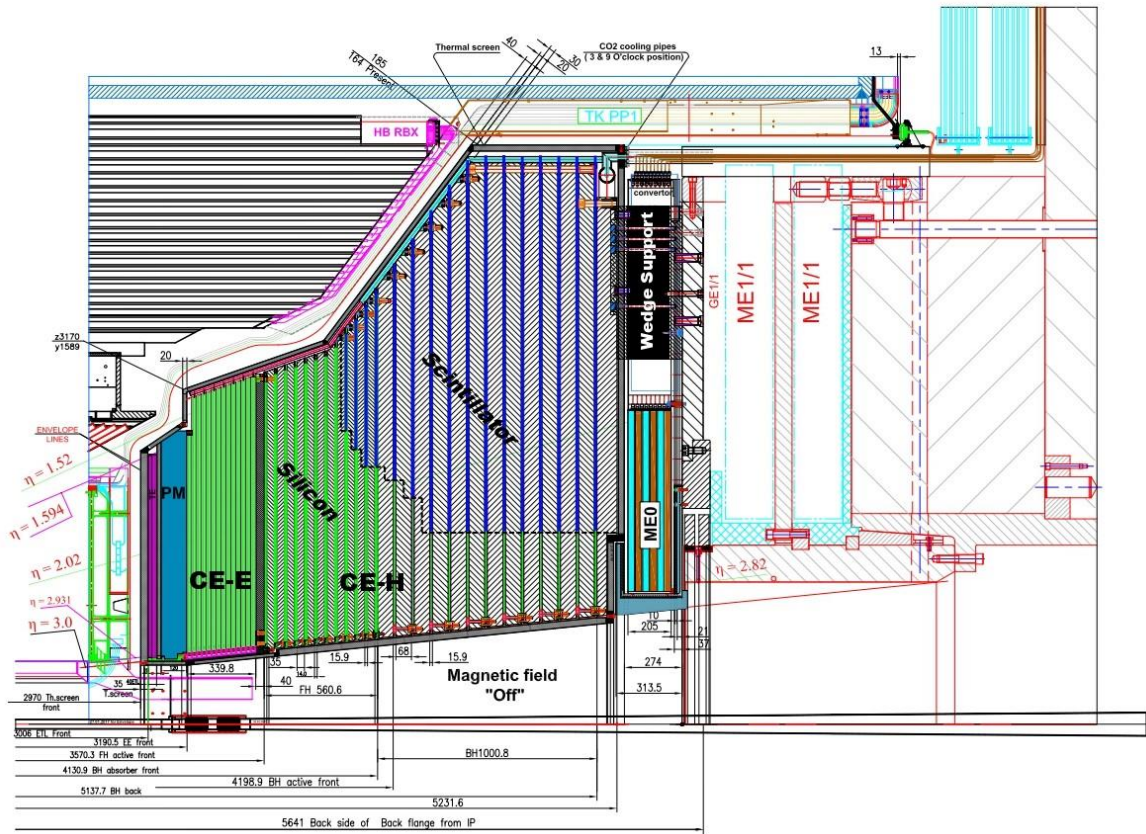
Figure 3.3: Longitudinal cross section of the upper half of one endcap calorimeter

3.4.1.   Active Elements

Silicon modules:

The HGCal requires approximately 27,000 silicon detector modules to be assembled and installed in its electromagnetic (CE-E) section and part of the hadronic (CE-H) section. A CE-E module is a stack of components, improving thermal contact (Figure 3.4).
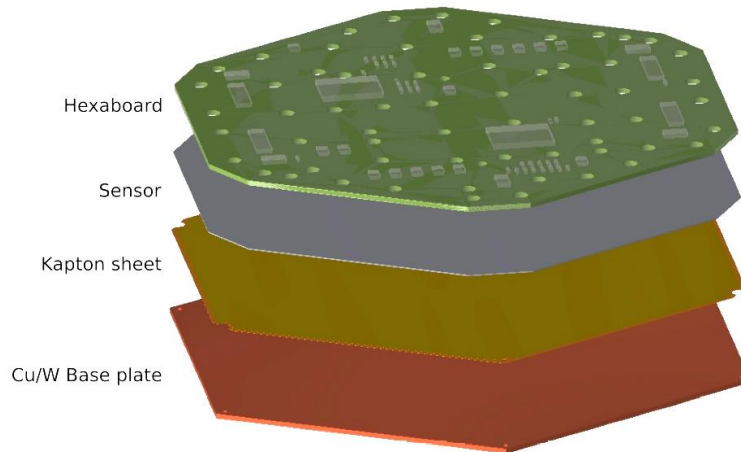
Figure 3.4: CE-E silicon module, showing stacked layers

- The **Cu/W base plate** is a sintered WCu metal matrix composite which provides excellent thermal conductivity and reduces the coefficient of thermal expansion.
- The **Kapton sheet** consists of a thick Kapton foil coated with a thin layer of gold. This layer provides the HV bias connection to the sensor back-plane. The Kapton itself provides electrical insulation of the sensor back-plane from the baseplate, which is held at ground.
- The **silicon sensors** are planar DC-coupled hexagonal silicon sensors fabricated on 8 inch (8") wafers. The vertices of the hexagonal sensors are truncated, allowing clearance for the mounting/fixation system, and further increasing the use of the wafer surface. Sensors will have three different active thicknesses (300, 200 and 120 μm) in order to optimise the charge collection and operation conditions.
- The ground return from each individual cell is provided through the DC connection to the corresponding front-end amplifier. In addition, the signals from the sensor pads are routed to the **hexaboard** for on-board signal digitization.

The baseplate, Kapton, silicon sensor, and hexaboard are bonded together with epoxy to form a single physical unit. Sets of multiple wirebonds are made and protected by encapsulating them with a silicon elastomer.

Scintillator tile-modules:

The hadronic calorimeter will use scintillator as the active material in regions where the integrated dose is low-enough and the fluency limited. An additional advantage is that this also enables a good efficiency for muon identification.

The scintillator is formed into small **tiles** and scintillation light is directly read out by a **SiPM** that is optically coupled through a small "**dimple**" in the centre of one face of the tile. The SiPMs are mounted on a **printed circuit board** which is then mated with the appropriate tiles. This system is illustrated in Figure 3.5.
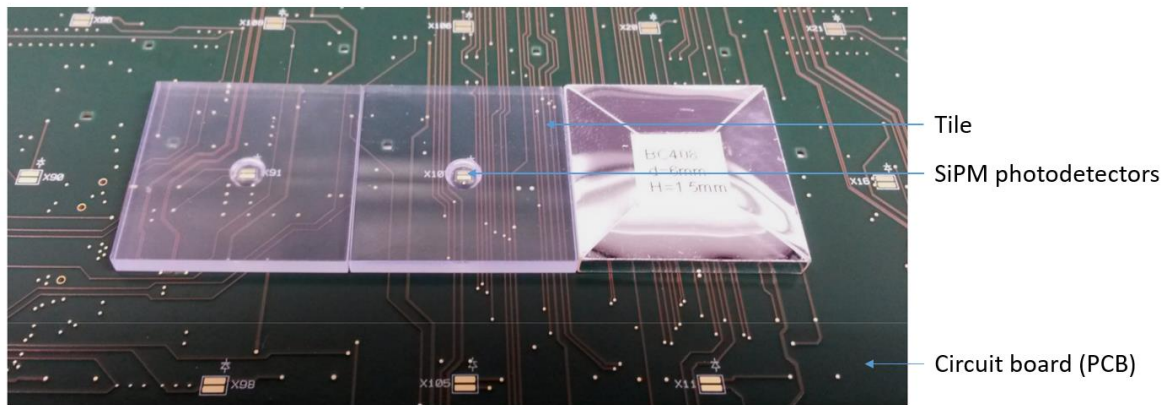
Figure 3.5: Scintillator tiles mounted on a PCB that holds one SIPM per tile. The two left scintillators are unwrapped to show the SiPM within the small dome, while the right tile is wrapped with reflective foil

3.4.2.   Cassettes

The sensors in each layer of the HGCal are grouped into 30° or 60° wedges called **cassettes**. The three different types of cassettes – CE-E, CE-H (silicon) and CE-H (mixed) – have different thicknesses and layouts determined by their respective components: cooling plate, silicon or scintillator sensors, electronics, and covers/absorbers.
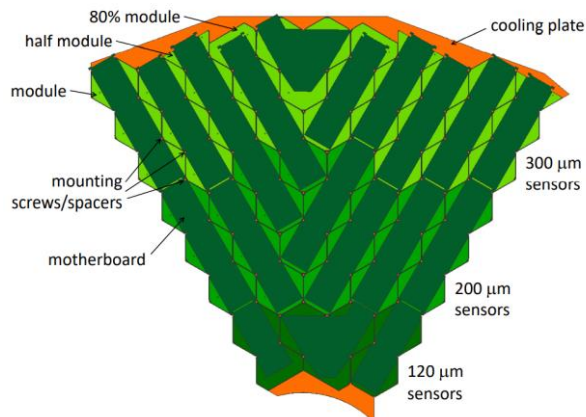
Figure 3.6: Schematic layout of a CE-E cassette showing the layout of the silicon modules and a possible motherboard configuration
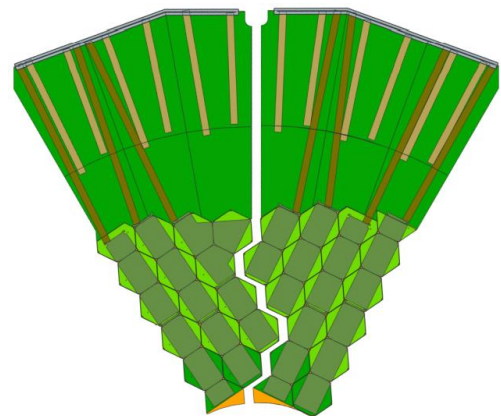
Figure 3.7: Schematic layout of a CE-H mixed silicon/ scintillator cassette ready to be joined into a 60° unit insertion
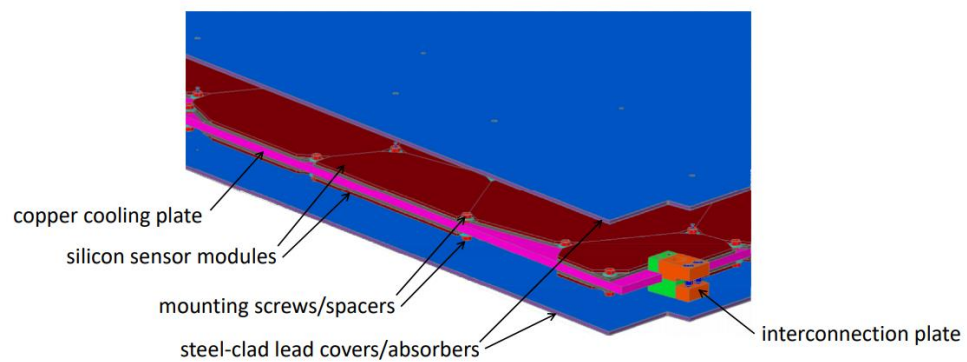
Figure 3.8: 3D model of the outer edge of a CE-E cassette, showing silicon modules mounted on the two sides of the cooling plate and the stainless steel clad lead covers/absorbers

The **CE-E cassette** (Figure 3.6 and Figure 3.8) is built by tiling the hexagonal **silicon modules** on both sides of the central **cooling plate,** which carries high-pressure two-phase CO_2 fluid through 4 mm inner diameter thin-wall stainless steel tubes**.** The first 500 mm of the cooling tube is a reduced inner diameter capillary to equalize the flow among different size cooling plates. In addition, tubes follow a serpentine path to minimise the temperature difference across the surface of the cassette. **Motherboards** are mounted on rows of modules and joined end-to-end to form a continuous line which brings low-voltage power and control signals to the individual modules. Two 2.1 mm thick stainless **steel clad lead covers/absorbers** close the cassette on both sides. Special **screw assemblies** secure the modules at their corners and serve as spacers to define the gap between the cooling plate and the covers in which the active detector elements are located. The modules and cassettes are also azimuthally aligned with each other for structural reasons in a way that the spacers align in all layers.

Cassettes with silicon modules are used in the **first eight layers of the CE-H**. They are of similar design to those in the CE-E, with the following differences: the cassettes are single-sided with modules mounted on only one side of the cooling plate; the cover serves only as a mechanically and electrically protective layer and is therefore made of 1 mm thick copper; they are built in 30° units; and 60° pairs of cassettes are connected to the adjacent steel absorber layer rather than to each other.

Starting in CE-H layer 9, the outer silicon modules are replaced by scintillator/SiPM panels, and the fraction of scintillator used grows progressively towards the back of the CE-H (Figure 3.7). The scintillator area fraction varies from 40% in CE-H layer 9 to 90% in layers 16-24. Scintillator tiles are arranged in an r-ϕ grid. Therefore, the smaller sized tiles at small radii give larger signals where the radiation damage to the scintillator and the SiPM noise will be the largest. The $\Delta\varphi$ angular size of the cells is chosen to keep the size of the scintillator cell similar in physical size to the silicon trigger cells at the boundary between the scintillator and the silicon.

3.4.3.   Structural Design

The mechanical structure of the endcap calorimeter, shown in Figure 3.3, consists of a set of steel disks that is used as absorber material for the CE-H, a structure for supporting the stack of cassettes for the CE-E, and a polyethylene neutron moderator, whose purpose is to reduce the neutron flux in the Tracker.

Electromagnetic calorimeter (CE-E)

The structure of the electromagnetic section (CE-E) consists of **14 layers of cassettes** providing a total of 28 sampling layers. In CE-E, each mechanical layer (two detector layers) consists of a disk formed by joining six 60° cassettes where the absorber layers are integrated.

Cassettes are joined to the next with **connection plates** at the outer radius and an **interconnection ring** that fits around the central cone. Finally, they are stabilized in their longitudinal position by **brackets** located at the outer radius every 30°.

The whole structure is supported by a 40 mm thick stainless steel **back disk** and a 10 mm thick aluminium **support cone** (Figure 3.9).
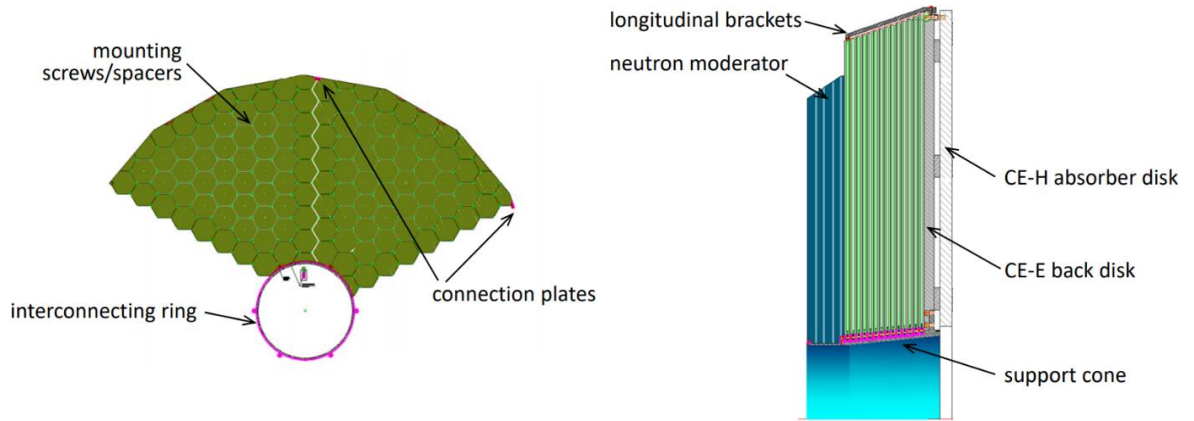
Figure 3.9: The structure of the CE-E shown in the operation position with the main elements indicated

Hadronic calorimeter (CE-H)

The hadronic calorimeter structure consists of 11 **stainless steel disks** of 35 mm thickness, 12 disks of 68 mm thickness and a 94 mm thick **back disk**. Between these absorber plates silicon modules and scintillator tileboards are mounted on 6 mm thick copper cooling plates to form 30° wide **cassettes**. The stainless steel back disk of the CE-E serves as the absorber in front of the first CE-H detector layer. **Spacers, bolts and tie rods** are placed between the absorber plates every 30° around the outer and inner peripheries. The spacers define the cassette slot thickness and also serve as shear keys to transfer the weight from one layer to the next and ultimately to the back disk. The cantilevered moment of the structure is taken by the bolts and tie rods that pass through the centres of the spacers (Figure 3.10).
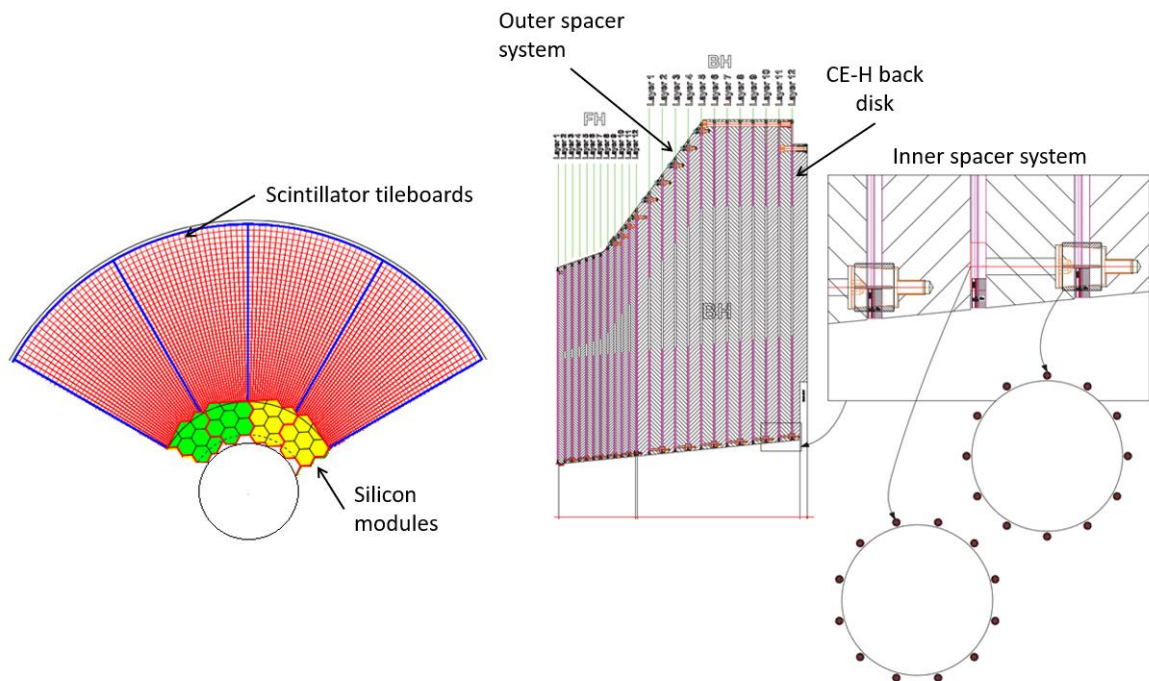
Figure 3.10: (Left) Layout of wafers and tiles in a layer where both are present. (Right) The structure of the CE-E shown in the operation position with the main elements indicated

Endcap suspension system

As shown in Figure 3.11, the entire endcap calorimeter is supported in a cantilevered fashion from the nose of Yoke Endcap 1 (YE1). The **back disk** is connected through a set of wedge-shaped blocks to a similar disk called the **back flange**, which then transfers the weight of the endcap to a large diameter steel **support tube** connected to the YE1 disk.

The **wedge supports** serve to:

- transfer both the vertical load and rotational moment of the HGCal to the back flange.
- provide thermal isolation between the HGCal, which operates at −35 °C, and the room temperature.
- provide sliding surfaces that allow approximately 2 mm radius reduction of the HGCal when cooled to -35 °C.
- define the space between the back disk and back flange that is occupied by the Muon Endcap 0 (ME0) and electrical services for the CE.

The rotational moment of the HGCal about the end of the support tube is taken by a set of special **brackets**, that connect the outer radius of the back flange to the YE1 while allowing access to the ME1/1 chambers.

When the solenoid is energized, the YE1 structure is pulled towards the centre of the CMS. The magnetic force is restrained by a set of **"Z" stop blocks**. Nevertheless, some measurements of the deflections with the existing endcap show that there is approximately 2 mm relative motion between the brackets and the support tube. Therefore, a flexible **ring connection** structure is required.
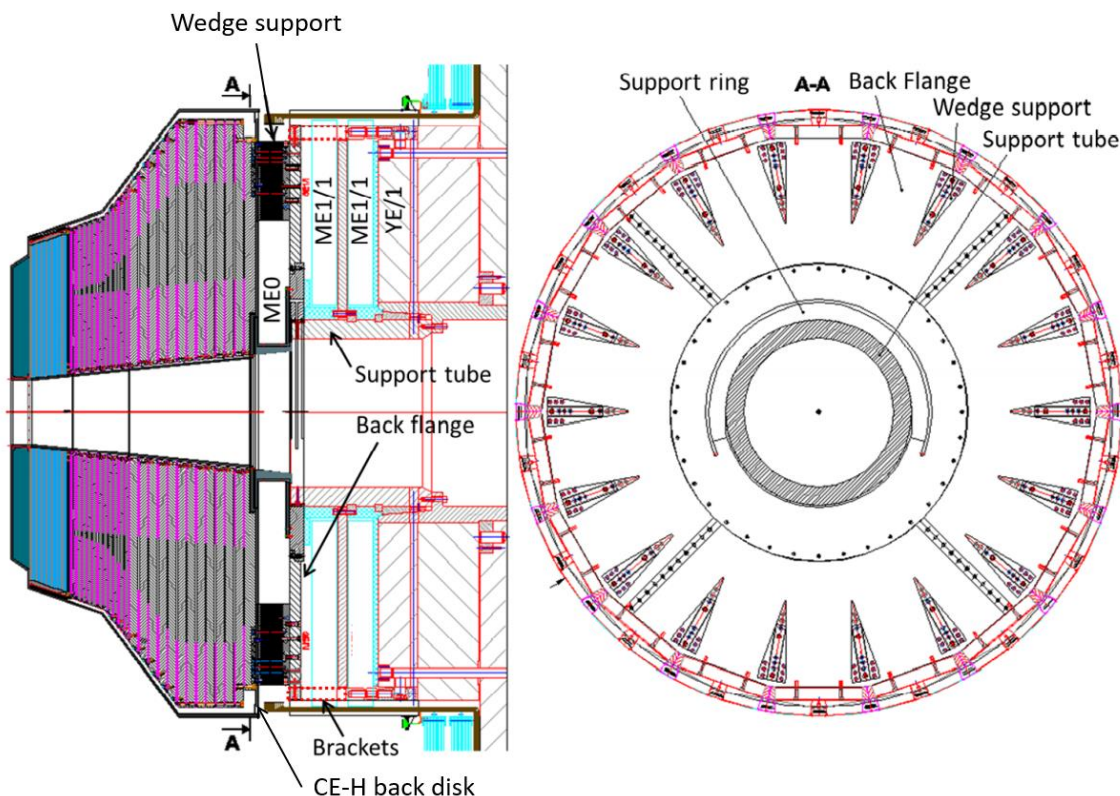
Figure 3.11: Endcap suspension system

3.4.4. Cooling and Environmental Control

The **cooling system** is responsible for removing the heat load and maintaining the silicon sensors at a temperature of −35 °C or lower. It is based on two-phase CO_2 fluid and will be designed for an electrical power of 300 kW at a nominal operating temperature of −35 °C.

A **thermal screen** will surround the detector to separate the cold dry detector volume from the ambient conditions in the cavern. It will be continuously flushed with dry nitrogen during operations and dry air for safety reasons.

3.4.5. Services

Services required for the operation of the HGCal include **CO_2 cooling**, **low-voltage** for the electronics and **high-voltage** to bias the silicon detectors, **optical fibres** for data trigger information and a **dry gas system**.

3.4.6. Assembly, Installation and Commissioning

The two endcap calorimeters will be assembled on the surface and completely tested before lowering it into the underground collision hall, UXC, and mounting on the YE1. The assembly sequence is summarised in four main steps as shown in Figure 3.12:

a) stacking CE-E cassettes on the CE-E support structure. Attachment of the neutron moderator to the front of the completed CE-E.
b) assembly of the endcap suspension system and the CE-H absorber structure.
c) insertion of ME0 muon chambers and CE-H cassettes, and dressing with electrical, optical and cooling services.
d) assembly of the CE-E to the front of the CE-H. Electrical, optical and cooling services installation. Testing at operating temperature. Rotation to the vertical orientation.
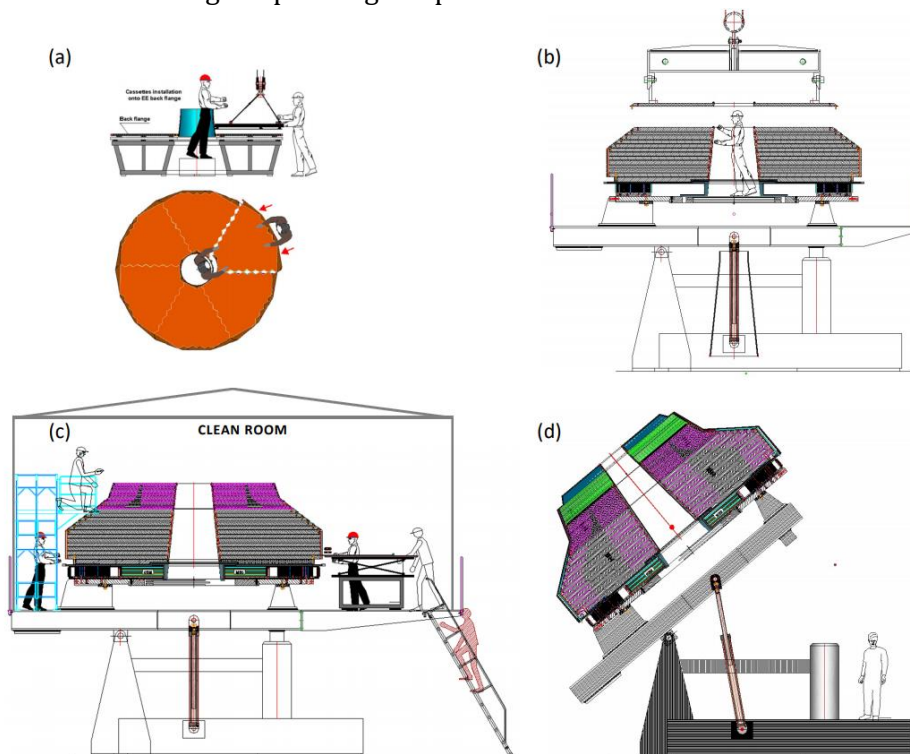
Figure 3.12: Summary of the detector assembly sequence

4.   Research and Preliminary Designs

4.1.   Introduction

Having briefly described the purpose of the organisation and the functioning of the accelerator and the detector that will be updated, I embraced the challenge of designing the wedge-shaped blocks that will connect the back disk to the back flange.

At this moment, there are four types of wedges as shown in Figure 4.1. In future analysis, it might change and two different kinds of intermediate wedges may be created. Each of them has a main function and several secondary ones. The difference will be revealed later on.

Specifically, I resolve to develop the **intermediate wedges design optimisation**.
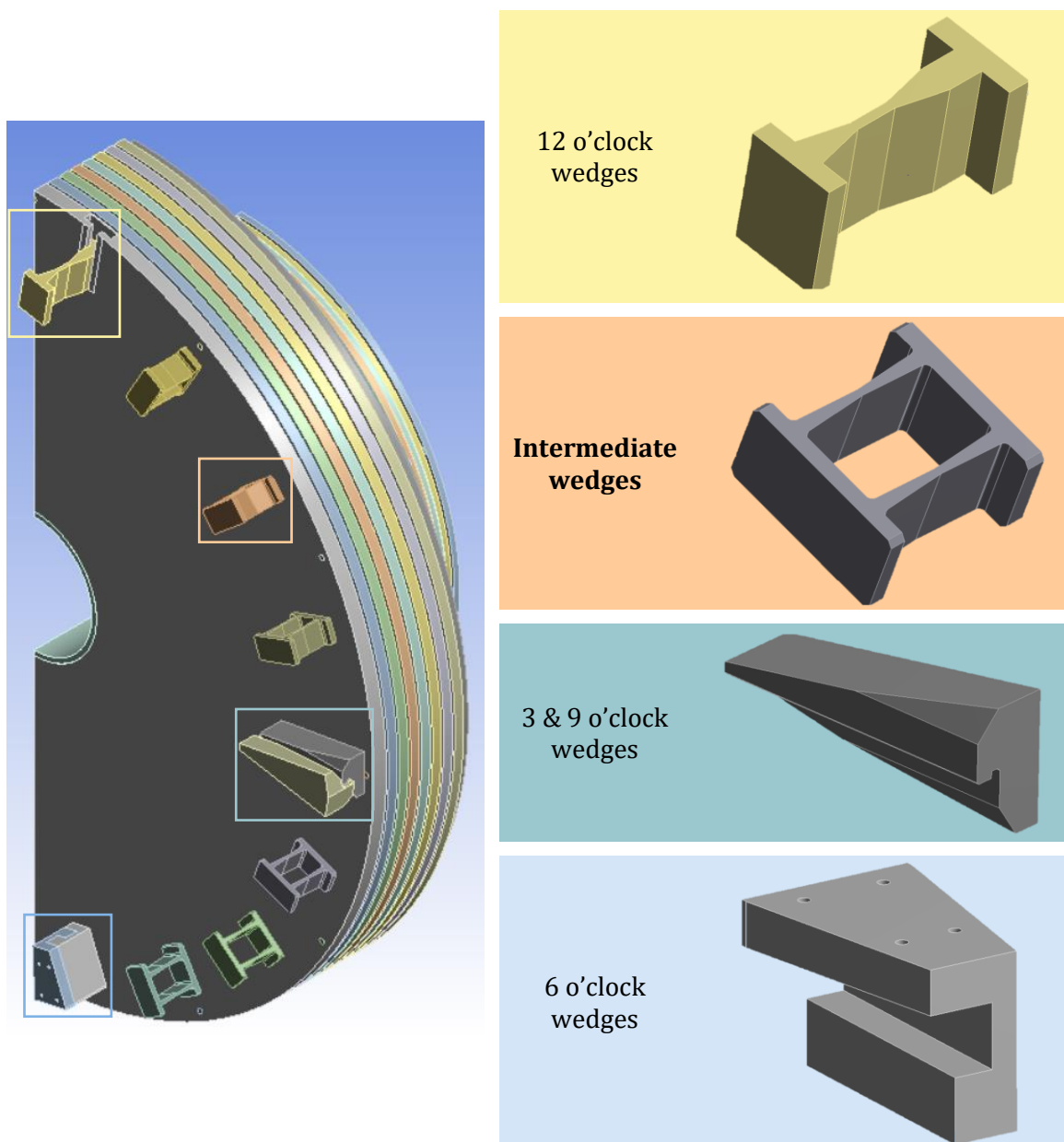
Figure 4.1: Different types of wedges. Preliminary shape and location

4.1.1. Basic Functions and Operating Mechanics

As already briefly described in section 3.4.3, wedges serve to:

- **transfer** both the **vertical load** and **rotational moment** of the HGCal to the back flange.
- **provide thermal isolation** between the HGCal, which operates at −35 °C, and the room temperature.
- **provide sliding surfaces** that allow approximately 2 mm radius reduction of the HGCal when cooled to -35 °C.
- **define** the **space between** the **back disk and back flange** that is occupied by the ME0 and electrical services for the CE.
- **allow horizontal assembly** without structure bending.
- **maintain parallelism** between the back disk and the back flange.

Therefore, wedges' basic function is closely related to the operating mechanics.

As schematised in Figure 4.2, in the **operation position (vertical)**, three loads act on the system. Self-weight creates a shear force and a bending moment respectively offset by 3 & 9 o'clock and 12 & 6 o'clock wedges. Furthermore, the 6 o'clock wedges must cancel out the seismic force. Finally, magnetic force will pull the whole structure towards the centre of the CMS. As explained above, in section 3.4.3, the structure will be restrained by the "Z" stop blocks and the ring connection, parts which do not belong to this study.

In the **assembly position (horizontal)**, only self-weight acts. In addition to that, a compression force which bends the structure of the calorimeter is occurring. Consequently, another type of wedge supports need to be created: the **intermediate wedges**.
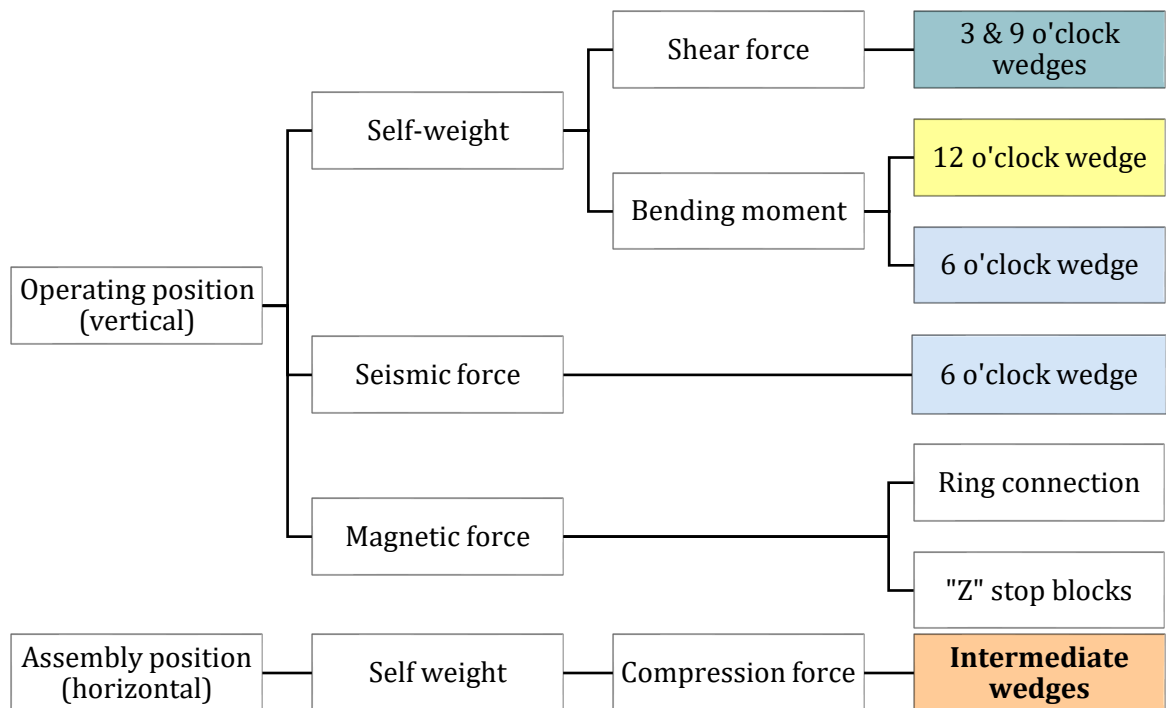
Figure 4.2: Different types of loads and their structural solution

As seen above, these different applications define different kind of supports, with their respective forms and functions. Next, in Figure 4.3, we will specify for each of them its main and secondary functions.

	3 & 9 o'clock wedges	12 o'clock wedges	6 o'clock wedges	**Intermediate wedges**
Basic function	Transfer shear force	Transfer bending moment (compression)	Transfer bending moment (tension) + seismic force	Maintain parallelism / Transfer compression force
Thermal isolation	Material	Material	Material	Material
Sliding surfaces	Design - degrees of freedom	Design - degrees of freedom	Design - degrees of freedom	Material

Figure 4.3: Main and secondary functions of the four different kinds of wedges

4.1.2. General Requirements

In order for wedges to function properly, the following essential goals must be achieved:

- For transferring loads without plastic deformation, it is necessary to reach a **high yield strength** coefficient.
- To provide sliding surfaces, a flexible material (with a **low Young's modulus**) or a sliding/ hinged mechanism is required.
- With the purpose of achieving thermal isolation, a **low thermal conductivity coefficient** is needed.
- The **minimum service temperature** required is **-35 °C**.
- A **low thermal expansion coefficient** allows the maintenance of parallelism and the predefined space between the back disk and the back flange.
- To avoid creating a magnetic force component, **non-magnetic materials** must be used.

4.1.3. Regulations

The standards on which the project is based are described in **Eurocode 3**. It is divided into several parts, three of which are of special interest for our study [10]:

- *Eurocode 3 - Design of steel structures - Part 1-5: Plated structural elements* [11] & *Part 1-4: General rules - Supplementary rules for stainless steels* [12], as CE-H is a structure formed by stainless steel disks.
- *Eurocode 3 - Design of steel structures - Part 1-8: Design of joints* [13], because it contains bolts and dowel pins that keep the construction compact.

In none of these documents there is any reference on how wedges have to be designed. However, in [11, p. 49], [12, p. 12] and [14, pp. 101-114] it is specified how to determine a parameter of vital importance for our study, the **safety factor** ($\boldsymbol{\gamma_s}$).

In short, it should be verified that:

$$\boldsymbol{\gamma_s} > \gamma_1 \cdot \gamma_2 \qquad \textit{(Eq. 4.1)}$$

where,

- γ_1 covers the model uncertainty of the FE-modelling used. It should be obtained from evaluations of test calibrations, see Annex D to EN 1990. However, as we are in an early stage of design, this test has not yet been carried out.

- γ_2 covers the scatter of the loading and resistance models. It may be taken as γ_{M1} if instability governs and γ_{M2} if fracture governs. In our case, instability governs because buckling is expected. So, the following value is recommended:

$$\gamma_2 = \gamma_{M1} = 1.1$$

In conclusion, the used safety factor should verify

$$\boldsymbol{\gamma_s} > 1.1$$

and, ideally, it should be

$$\boldsymbol{\gamma_s} > 1.5$$

4.2.   Material Selection

To determine which material will be needed to build the wedges, Ansys Granta EduPack 2019 is used. This program facilitates materials' selection through Ashby diagrams and bar charts.

Firstly, the problem must be defined (Figure 4.4):

Function	• Wedge a heavy, thermally insulated structure
Restrictions	• Low Young's modulus • High yield strength • Low thermal conductivity • Low thermal expansion coefficient • Minimum service temperature: -35°C • Non-magnetic
Objectives	• Minimise mass • Economic
Variables	• Material selection

Figure 4.4: Problem definition

Secondly, in order to pursue the goals described above, restrictions will be imposed one by one rejecting step by step a series of materials.

Step 1: Stiffness

Wedge supports have to be elastic and provide sliding surfaces when the calorimeter structure cools to -35 °C. The stiffness of a material can be quantified through the Young's modulus.

If the goal is to minimise the mass, we approximate the wedges' geometry to a uniform cross section bar which is tested on tension, compression and flexion. Therefore, the performance indexes that have to be minimised are:

Tension & compression   *Flexion*

$$K_{1.1} = \frac{E}{\rho} \qquad\qquad\qquad K_{1.2} = \frac{E^{1/2}}{\rho} \qquad \textit{(Eq. 4.2)}$$

and applying logarithms:

$$\log E = \log K_{1.1} + \log \rho \qquad\qquad \log E = 2 \log K_{1.2} + 2 \log \rho \qquad \textit{(Eq. 4.3)}$$

Then, when maximising the index, a slope of 1 and 2 will be drawn on the diagram in Figure 4.5 and moved downwards.
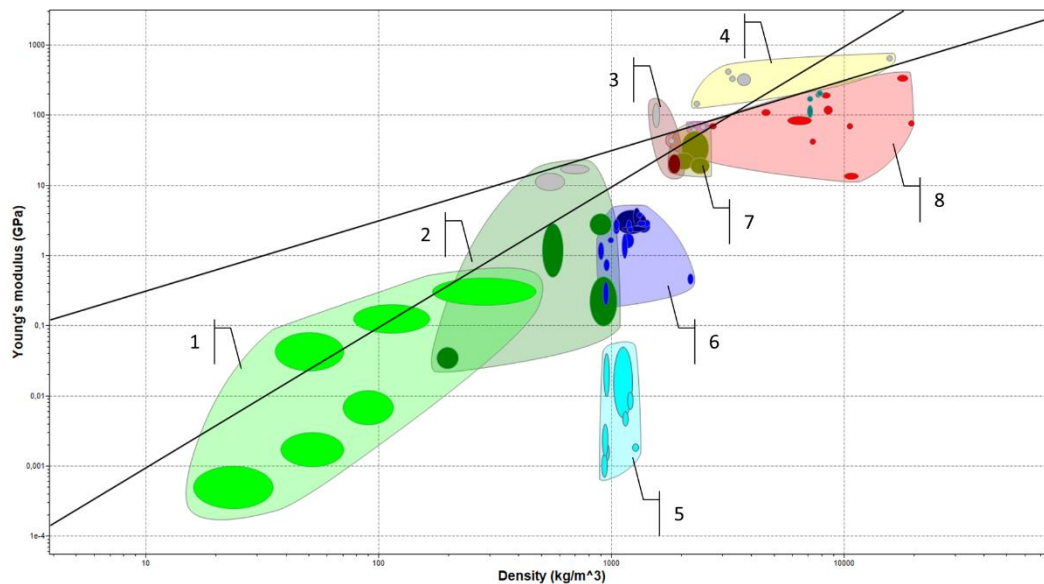
Figure 4.5: Density – Young's modulus Ashby diagram [ANSYS GRANTA]

The following Table 4.1 summarises the 56 materials that have appeared in the first selection:

Table 4.1: First materials' selection

1	Foams	Flexible Polymer Foam (LD, MD & VLD), Rigid Polymer Foam (HD, LD & MD)
2	Natural materials	Cork, Leather, Paper and cardboard, Wood
3	Composites	GFRP
4	Technical ceramics	Not analysed in the study
5	Elastomers	IIR, SBR, EVA, NR, CR, PUR, Silicon (SI, Q)
6	Polymers	ABS, CA, EP, ION, P, PA, PC, PEEK, PE, PET, PMMA, POM, PP, PS, PTFE, PVC, UP
7	Non-technical ceramics	Brick, Concrete, Stone
8	Metals	Aluminium alloys, Cast iron (ductile & gray), Copper alloys, Gold, High carbon steel, Low alloy steel, Low carbon steel, Medium carbon steel, Stainless steel, Lead alloys, Nickel alloys, Silver, Tin, Titanium alloys, Tungsten alloys, Zinc alloys

ETSEIB   CMS

Step 2: Strength of Materials

It is very important that the supports do not suffer permanent deformation in nominal conditions. Consequently, the elastic limit of the chosen material has to be high.

If the goal is to minimise the mass, we approximate the wedges' geometry to a uniform cross section bar which is tested on tension, compression, and flexion. Therefore, the performance indexes that have to be maximised are:

$$\text{Tension \& compression} \qquad\qquad \text{Flexion}$$
$$K_{2.1} = \frac{\sigma}{\rho} \qquad\qquad\qquad K_{2.2} = \frac{\sigma^{2/3}}{\rho} \qquad\qquad \textit{(Eq. 4.4)}$$

and applying logarithms:

$$\log \sigma = \log K_{2.1} + \log \rho \qquad\qquad \log \sigma = \frac{3}{2} \log K_{2.2} + \frac{3}{2} \log \rho \qquad \textit{(Eq. 4.5)}$$

Then, when maximising the index, a slope of 1 and 3/2 will be drawn on the diagram in Figure 4.6 and moved upwards.
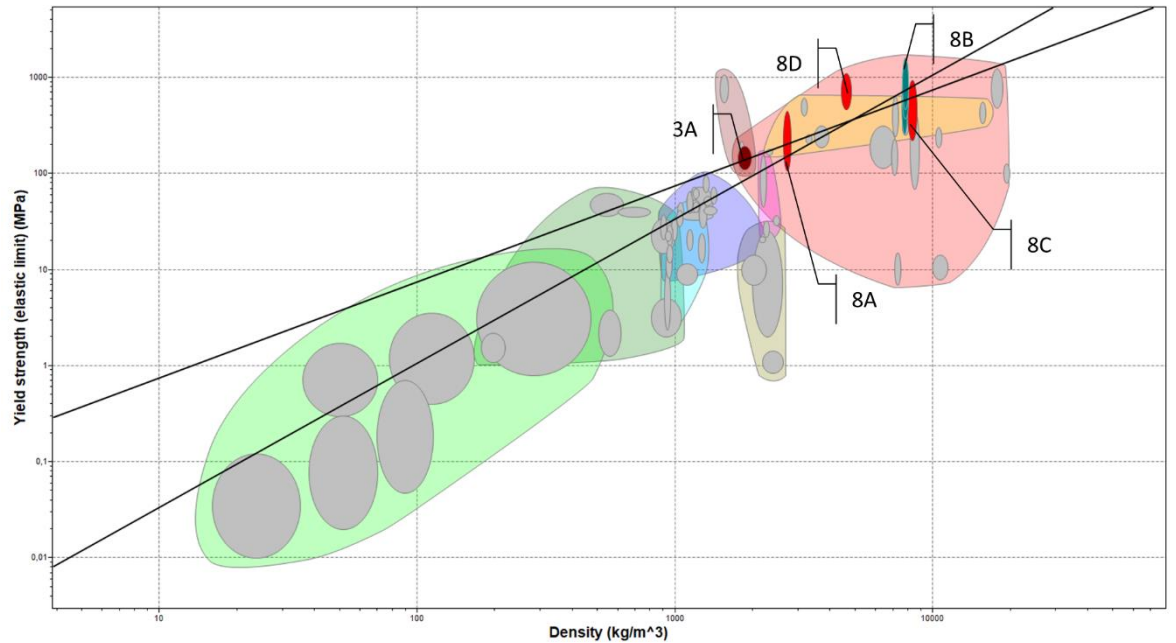
Figure 4.6: Density – Yield strength Ashby diagram [ANSYS GRANTA]

The following Table 4.2 summarises the 8 materials that have appeared in the second selection:

Table 4.2: Second materials' selection

3	■	Composites	GFRP (A)
8	■	Metals	Aluminium alloys (A), High carbon steel (B), Low alloy steel (B), Medium carbon steel (B), Stainless steel (B), Nickel alloys (C), Titanium alloys (D)

Step 3: Thermal Conductivity

Wedges join two regions of the detector that are at different temperatures. On the one hand, the HGCal operates at -35 °C. On the other hand, the back flange finds itself at room temperature (22 °C).

Therefore, to ensure that the calorimeter is thermally insulated, it is proposed to choose a material with a low thermal conductivity coefficient.

The following Table 4.3 summarises the 7 materials that have appeared in the third selection, after choosing those materials with lowest thermal conductivity coefficient in Figure 4.7:

Table 4.3: Third materials' selection

8		Metals	Aluminium alloys (A), High carbon steel (B.I), Low alloy steel (B.II), Medium carbon steel (B.III), Stainless steel (B.IV), Nickel alloys (C), Titanium alloys (D)

Step 4: Thermal Expansion Coefficient

In addition, to ensure parallelism once the structure is cooled down, it is proposed to choose a material with a low thermal expansion coefficient.

The following Table 4.4 summarises the 7 materials that have appeared in the fourth selection, after choosing those materials with lowest thermal conductivity coefficient in Figure 4.8:

Table 4.4: Fourth materials' selection

8		Metals	Aluminium alloys (A), High carbon steel (B.I), Low alloy steel (B.II), Medium carbon steel (B.III), Stainless steel (B.IV), Nickel alloys (C), Titanium alloys (D)

Step 5: Minimum Service Temperature

As the HGCal operates at -35 °C, the selected material should be able to withstand this temperature without becoming fragile or unsafe.

The following Table 4.5 summarises the 5 materials that have appeared in the fifth selection and can operate at -35 °C as shown in Figure 4.9:

Table 4.5: Fifth materials' selection

8		Metals	Aluminium alloys, Low alloy steel, Stainless steel, Nickel alloys, Titanium alloys

Step 6: Magnetic Polarisation

As the HGCal operates in a magnetic field, the selected material must be non-magnetic so that the structure is not pushed towards the centre of the CMS.

The following Table 4.6 summarises the 3 materials that have appeared in the sixth selection and are non-magnetic as shown in Figure 4.10:

Table 4.6: Sixth materials' selection

8		Metals	Aluminium alloys, Stainless steel, Titanium alloys

ETSEIB

CMS
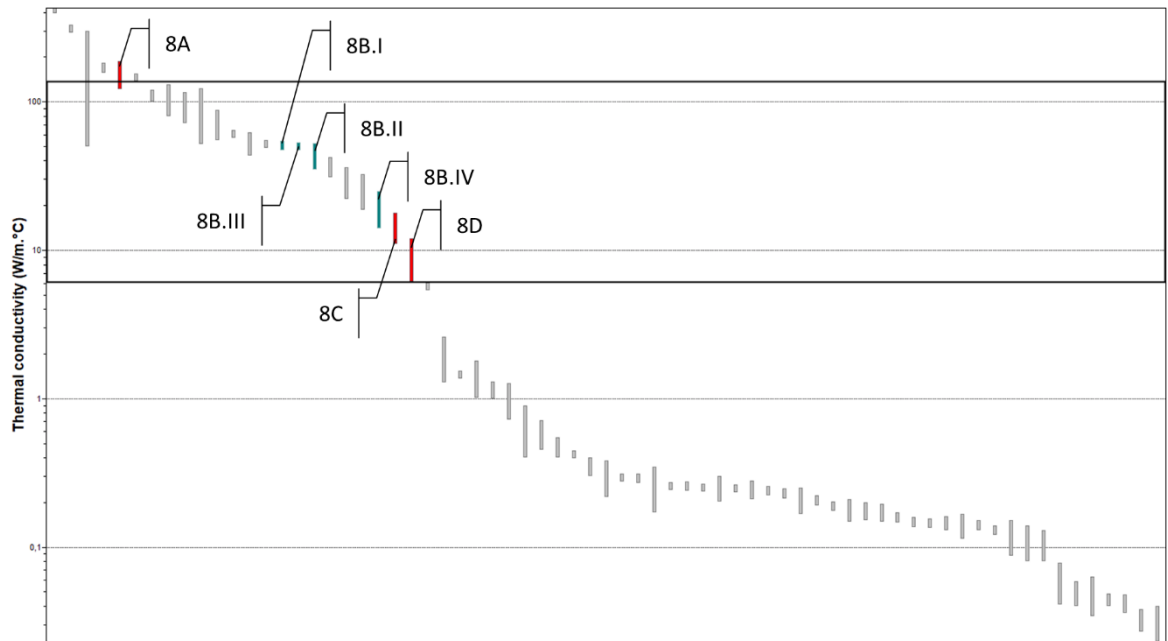
Figure 4.7: Thermal conductivity bar chart [ANSYS GRANTA]
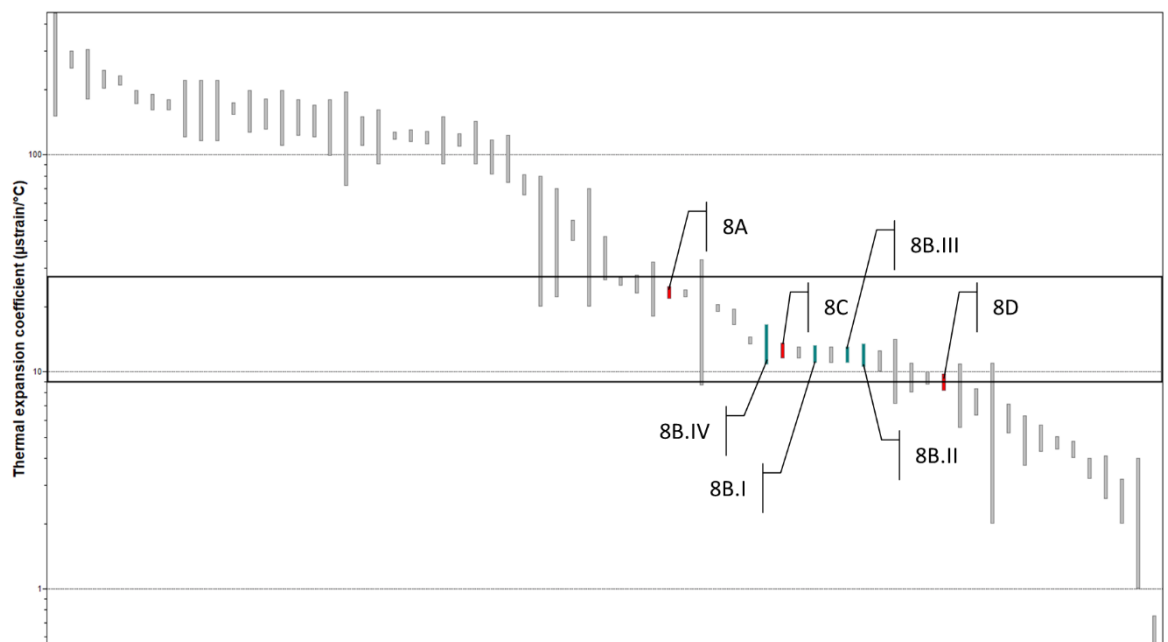
Figure 4.8: Thermal expansion coefficient bar chart [ANSYS GRANTA]
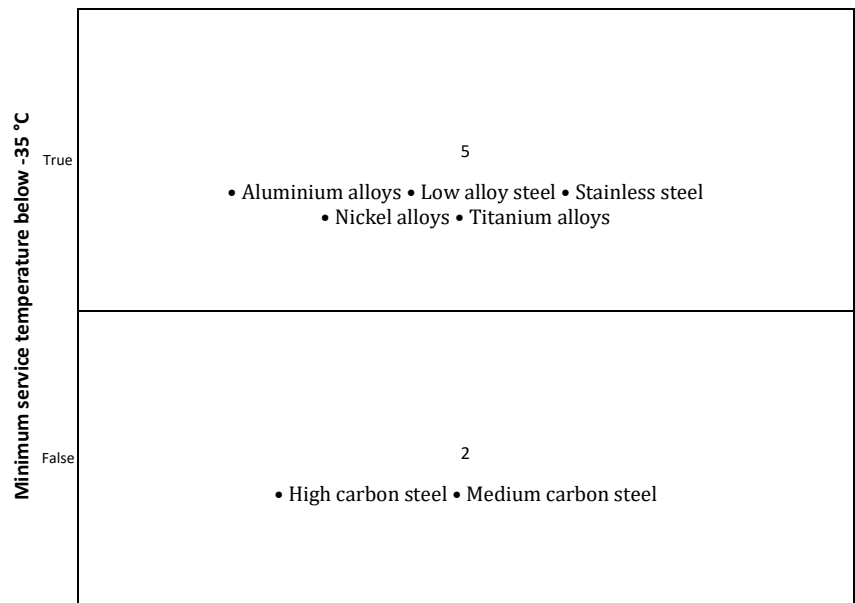
Figure 4.9: Minimum service temperature chart [ANSYS GRANTA]
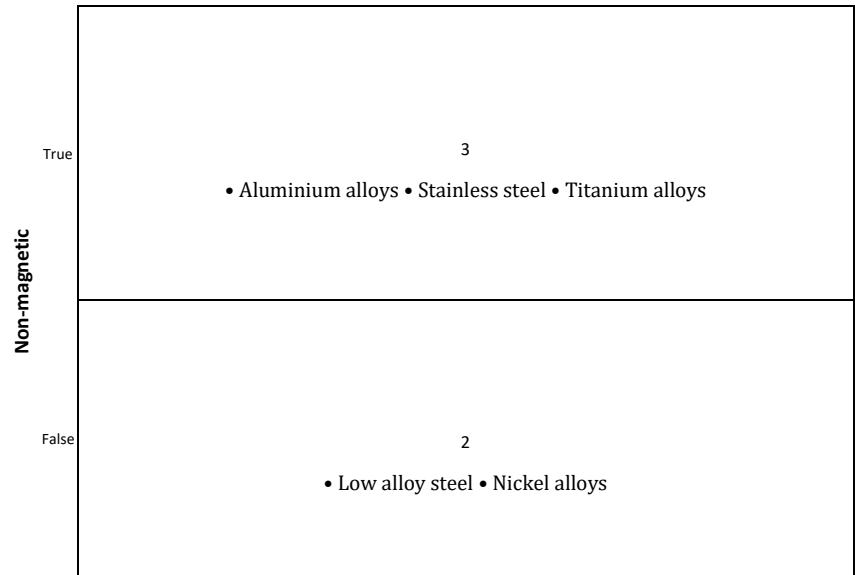
Figure 4.10: Magnetic chart [ANSYS GRANTA]

Conclusions

From the results obtained, next we will proceed to quantitatively compare the three remaining materials of the selection described above.

Table 4.7: Comparative analysis of general, thermal, and mechanical properties of stainless steel, aluminium alloys and titanium alloys at 20 °C [1] [ANSYS GRANTA]

		Stainless steel	Aluminium alloys	Titanium alloys
Density	kg/m^3	7850	2770	4620
Thermal conductivity	$W/m \cdot °C$	15.1	148.62	21.9
Thermal expansion coefficient	$10^{-6}/°C$	17	23	9.4
Minimum service temperature	$°C$	-196	-270	-273
Young's modulus	GPa	193	71	96
Tensile yield strength	MPa	207	280	930
Tensile ultimate strength	MPa	586	310	1070
Price	$€/kg$	2.8	2.3	20.4

Based on the values detailed in Table 4.7, a ranking will be established:

On the first place we find **titanium alloys**, since price is an unimportant objective to meet, and this material meets the mechanical imposed restrictions the best.

On second place we find **stainless steel**. Despite being the most rigid material (with a higher Young's modulus) it meets the rest of the requirements cost-effectively. Then, it can be used instead of titanium for the 3, 6, 9 & 12 o'clock wedges and a sliding/ hinged version the intermediate ones, in which a mechanism allowing sliding surfaces already exists.

Finally, aluminium alloys are not going to be considered in this study because they do not meet the thermal conductivity criteria.

In conclusion, 3, 6, 9 & 12 o'clock wedges will be built with stainless steel and intermediate wedges with titanium or stainless steel.

---

[1] These values given for the different properties are at 20 °C. However, the operating temperature will be -35 °C and these properties may change. In this preliminary phase of the project this modification will not be considered.

4.3.   Maximum Permissible Force, Dispersion and Characteristic Values

As already stated in section 4.1.1, the calorimeter will be positioned horizontally to be assembled and vertically during its lifetime. In each of these positions, different actions will intervene, defining the main function of the wedges.

Below, a detailed study of the actions that are operating in each model is presented and a series of preliminary calculations of the possible reactions are developed.

4.3.1.   Assembly Position (Horizontal)

The assembly and installation processes are summarised in the following four stages:

a) Electromagnetic calorimeter assembly and tooling
b) Hadronic calorimeter assembly and tooling
c) Final assembly
d) Installation and tooling

Of these, b) and c) are of special interest and studied in depth. Firstly, we are developing each of the assembly stages, describing the expected loads (Figure 4.11). Secondly, in order to find the maximum permissible force in the assembly position, we are evaluating the reactions.
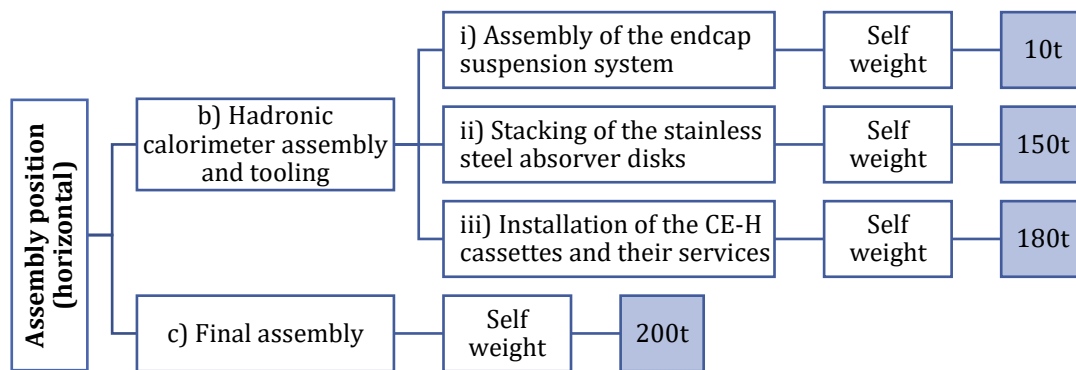
Figure 4.11: Definition of the loads acting on the HGCal structure in the assembly position

Hadronic Calorimeter Assembly and Tooling
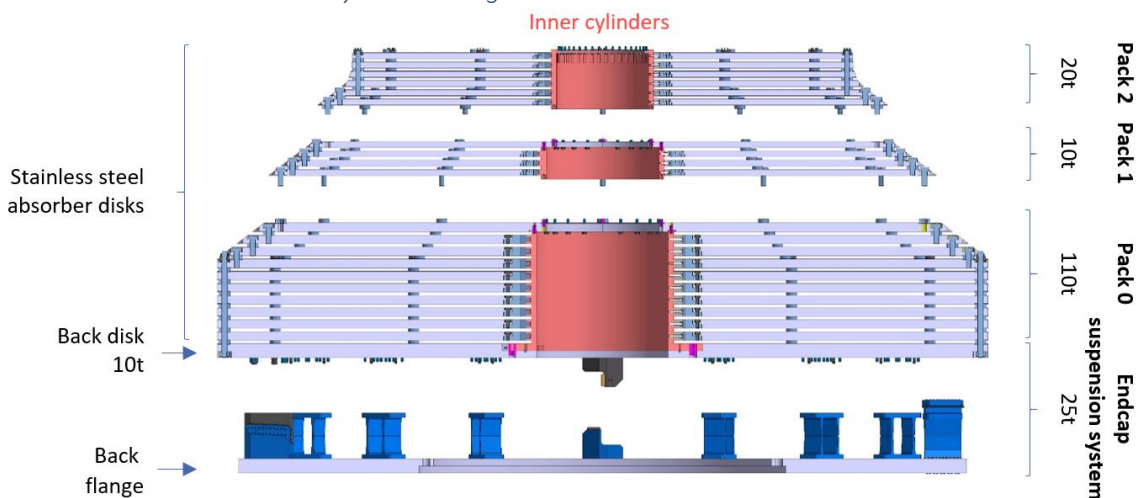
Figure 4.12: Load distribution throughout the CE-H structure

Construction of the hadronic calorimeter can be divided into several major stages:

i)   Assembly of the endcap suspension system
ii)   Stacking of the stainless steel absorber disks
iii)   Installation of the CE-H cassettes and their electrical and optical services

Mainly simple tooling is used. All components, procured from industry, will be fully inspected, and measured upon receipt and prior to assembly. Afterwards, it proceeds according to the following sequence:

Assembly of the endcap suspension system

1) The back flange is placed on the assembly table, and the intermediate and the first pair of 3 & 9 o'clock wedges are pinned and bolted.
2) The second pair of 3 & 9 o'clock wedges is placed and the back plate is lowered along two guiding shafts attached to the back flange and passing through 12 and 6 o'clock tie rod holes. Then, it is noticed that **14 wedges are supporting a total weight of 10 tons.**
3) Pin holes are drilled into intermediate wedges, and dowel pins and tightened bolts are inserted to fix them to the back disk. After the plate is set and bolted, 12 & 6 o'clock wedges can be installed but not fixed.
4) Dowel pins and tightened bolts are inserted to fix 3 & 9 o'clock wedges to the back disk. 12 & 6 o'clock wedges are fixed tightening the bolts.
5) The support ring is attached, and the combined assembly is inspected and measured.

(1)   (2)

(5)
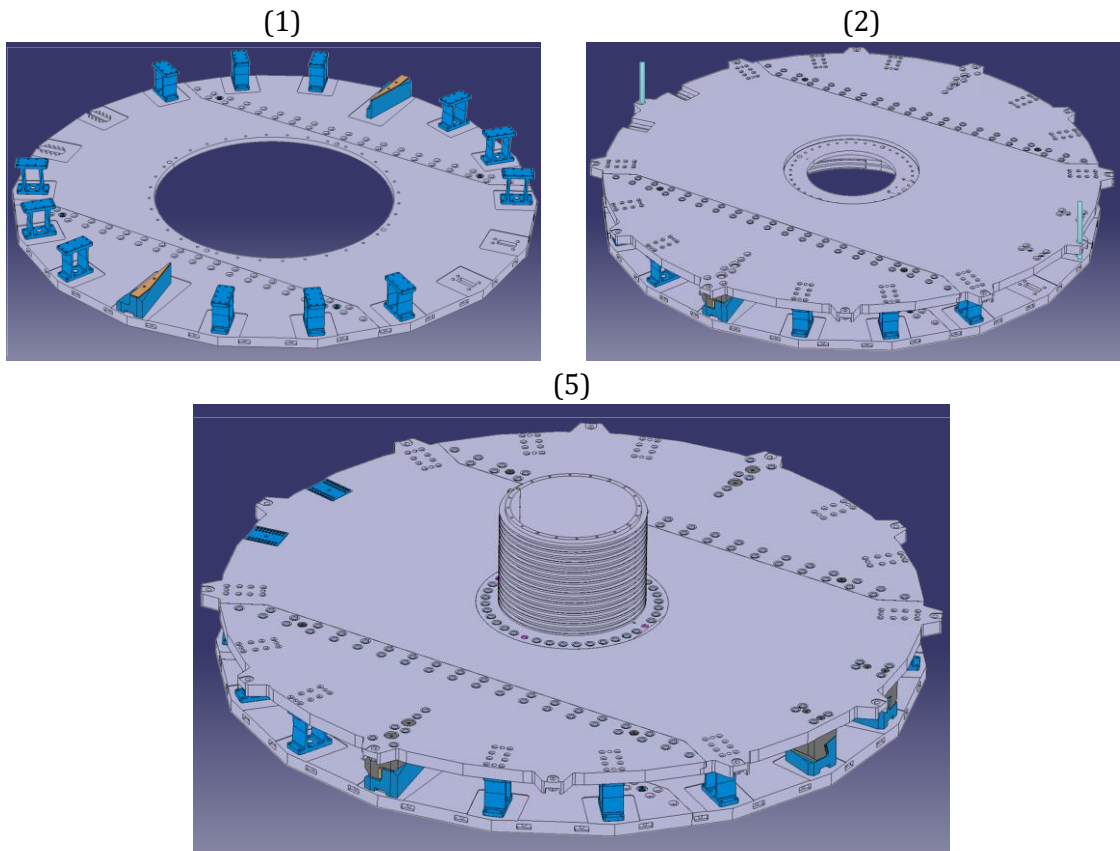
Figure 4.13: Assembly of the endcap suspension system. Steps 1, 2 and 5

Stacking of the stainless steel absorber disks

Repeating the following steps Pack 0, 1 and 2 are assembled, adding to the structure a total of 150 tons. In this case, however, there will be 18 wedges instead of 14:

6) The split ring is installed.
7) Spacers are fitted and the absorber central part is lowered along two guiding shafts attached to the back flange and passing through 12 and 6 o'clock tie rod holes. Pin holes are drilled, and dowel pins and tightened bolts are inserted to fix the plate.
8) Absorber ears are aligned and fixed to the central part.

Finally,

9) A complete inspection is carried out and a detailed set of mechanical measurements is established to ensure compliance with all mechanical and cleanliness requirements.

For the dis-assemble process, Pack 0 will need a complete disassembly. However, for Pack 1 & 2 only the ears have to be removed, thanks to the pyramid design. Then, there is no need to dis-assemble the central part of the pack for transport.
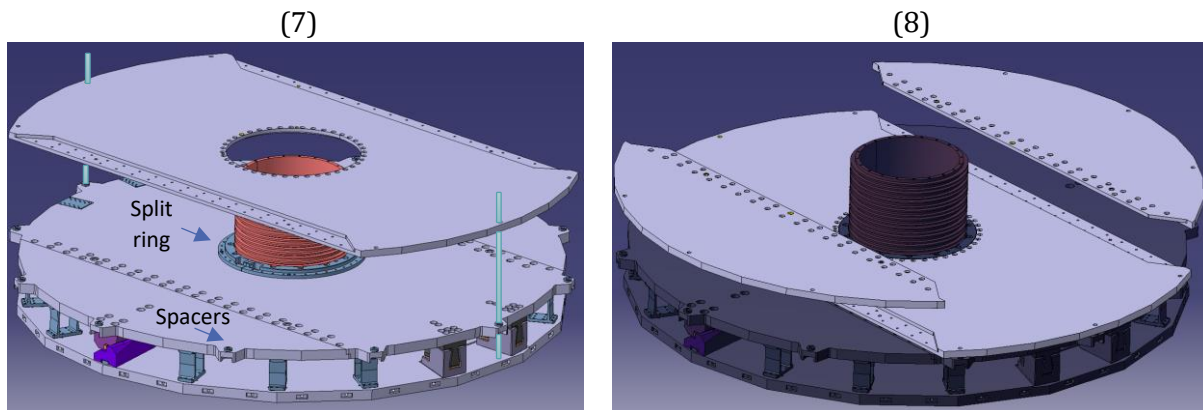
Figure 4.14: Assembly of stainless steel absorber disks. Steps 7 and 8

Installation of the CE-H cassettes and their electrical and optical services

An extension of the work platform is required to provide the radial space to position the cassettes prior to insertion.

Cassettes are inserted and all services are connected sequentially in 60° sectors. This is done for all layers except for the first CE-H cassette, since the absorber layer behind is the CE-E back disk and it is not present at this point. This last layer will be installed after the CE-E is mounted to the front of the CE-H.

After the connection of the services to each cassette pair, the integrity of the connections and the functioning of the cassette is verified since the services of subsequent layers will lie on top of each other and "trap" the cassette. The CO_2 cooling manifolds cannot be installed at this stage, since they cover the full thickness of the HGCal including the CE-E, which is not present.
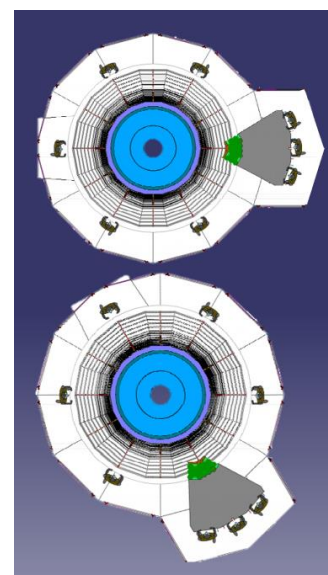
Figure 4.15: Installation of the CE-H cassettes

Final Assembly

In this stage, the CE-E is mounted on the front of the CE-H and the **total weight of 200 tons is supported by 18 wedges**. Then, the CE-E electrical and optical services, and the CO_2 cooling manifolds for the whole endcap are installed; the thermal screen is installed, and the cold-warm feedthrough is closed; CO_2 cooling is connected, and a complete cold test is performed.

CE-E
(20 t)

CE-H
(180 t)
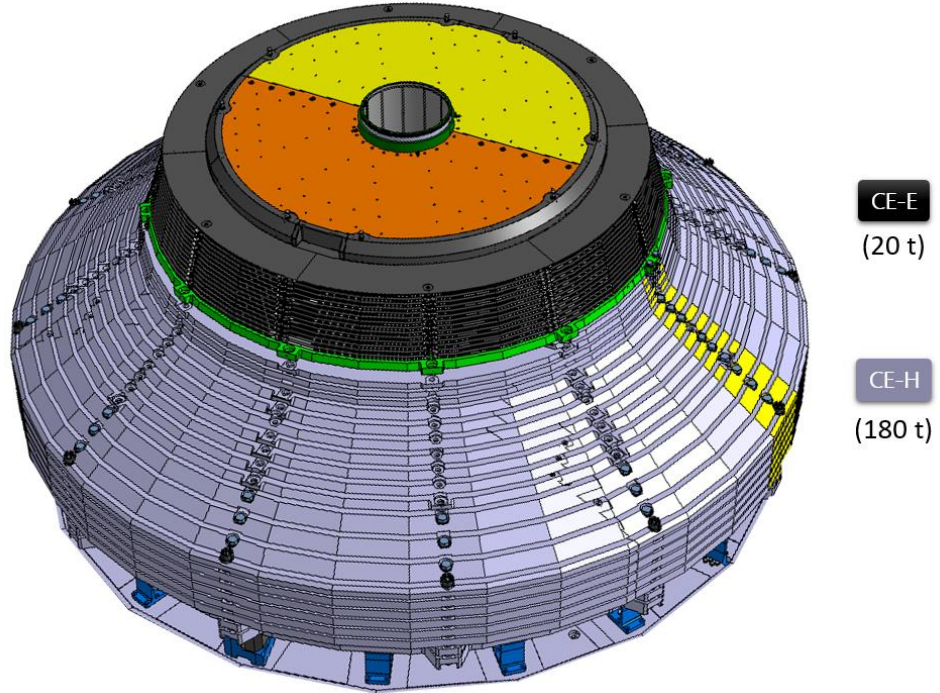
Figure 4.16: Final assembly

Conclusions

Based on the diagram in Figure 4.11 and the sentences highlighted in bold throughout the text, we focus on two cases in which the force could be maximum:

1) **14 wedges** are supporting a total weight of **10 tons**.

$$F_{hw_1} = 10{,}000 \, kg \cdot 9.806 \, \frac{m}{s^2} = 98.06 \, kN \qquad \text{(Eq. 4.6)}$$

$$F_{hw,i_1} = \frac{98.06 \, kN}{14} = 7 \, kN\!/_{wedge} \text{ with } 0 < i \le 14 \qquad \text{(Eq. 4.7)}$$

2) **18 wedges** are supporting a total weight of **200 tons**.

$$F_{hw_2} = 200{,}000 \, kg \cdot 9.806 \, \frac{m}{s^2} = 1961.2 \, kN \qquad \text{(Eq. 4.8)}$$

$$F_{hw,i_2} = \frac{1961.2 \, kN}{18} = 109 \, kN\!/_{wedge} \text{ with } 0 < i \le 18 \qquad \text{(Eq. 4.9)}$$

In conclusion, we determine from these previous calculations that the maximum permissible force is:

$$\boldsymbol{F_{hw}} = F_{hw_2} = 200{,}000 \, kg \cdot 9.806 \, \frac{m}{s^2} = 1961.2 \, kN \qquad \text{(Eq. 4.10)}$$

$$\boldsymbol{F_{hw,i}} = F_{hw,i_2} = \frac{1961.2 \, kN}{18} = \boldsymbol{109 \, kN\!/_{wedge}} \text{ with } 0 < i \le 18 \qquad \text{(Eq. 4.11)}$$

4.3.2.   Operation Position (Vertical)
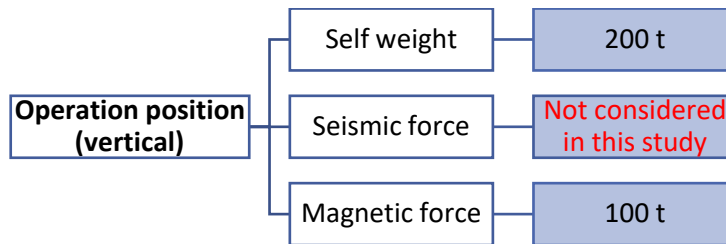
Figure 4.17: Definition of the loads acting on the HGCal structure in the operation position

As schematised in Figure 4.17, in the **operation position (vertical)**, three loads act on the system.

Self-weight creates a shear force and a bending moment respectively offset by 3 & 9 o'clock and 12 & 6 o'clock wedges. The total estimated weight is **200 tons** and it is distributed as indicated in Figure 4.11, Figure 4.12 and Figure 4.16.

The **seismic load** is an inertia force that acts on a construction structure and its magnitude and distribution continually change in time, from the start of the vibration. 6 o'clock wedges must cancel the force out. Nevertheless, in **this study it is not considered**.

The **magnetic force** will pull the whole structure towards the centre of the CMS. It is produced by the induced magnetic field and manufacturing defects, which affect the magnetic permeability of the chosen non-magnetic materials. Its value depends mainly on the relative magnetic permeability of the stainless steel parts and, after some complex magnetic simulations with TOSCA, it has turned out that with a relative permeability of 1.05, all the absorbers together add an integral force of **100 tons** to the system in the beam direction.

Ideal Situation

The ideal situation is the one in which the intermediate supports do not exist, and the shear force and the bending moment are compensated by 3 & 9 o'clock and 12 & 6 o'clock wedges, respectively. In addition, there will be a magnetic load of 100 t.

The following Figure 4.18 represents the loads and their respective reactions, calculated below (Eq. 4.12-15).
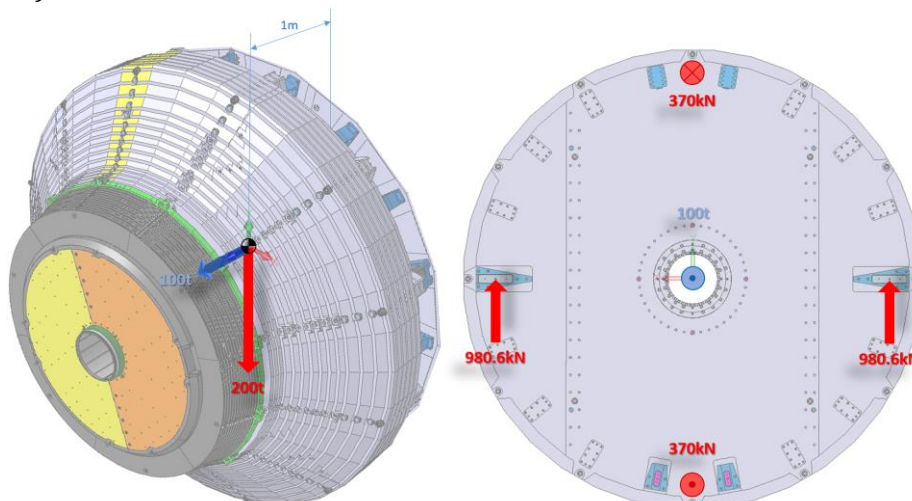
Figure 4.18: (Left) Loads' representation. (Right) Reactions' representation

$$F_{vw} = 200,000 \ kg \ \cdot 9.806 \ \frac{m}{s^2} = 1961.2 \ kN$$

<div align="right">(Eq. 4.12)</div>

$$\boldsymbol{F_{sf,3} = F_{sf,9} = \frac{F_{vw}}{2} = 980.6 \ {}^{kN}\!/_{wedge}}$$

<div align="right">(Eq. 4.13)</div>

$$M_{vw} = F_{vw} \cdot 1 \ m = 1961.2 \ kN \cdot m$$

<div align="right">(Eq. 4.14)</div>

$$\boldsymbol{F_{bm,12} = F_{bm,6} = \frac{M_{vw}}{\phi} = \frac{1961.2 \ kN \cdot m}{5.3 \ m} = 370 \ {}^{kN}\!/_{wedge}}$$

<div align="right">(Eq. 4.15)</div>

Real Situation

Due to the designed assembly method, in addition to 12, 3, 6 & 9 o'clock wedges, we have the intermediate ones. This modifies forces distribution, lightening the total load supported by the main wedges.

The Focus of the Study

In conclusion, the focus of the study will be to approach the ideal situation, optimising the intermediate wedges so that they barely support efforts in the operating position.

4.4. Preliminary Design and Prototype Construction

4.4.1. Preliminary Design

The preliminary design of the intermediate wedges is the one imposed by the department (Figure 4.19, Annex A.1). However, to simplify the model for its preliminary study, it has been decided to eliminate the drilled holes (Figure 4.20, Annex A.2). They will be redefined once the optimal design has been established.
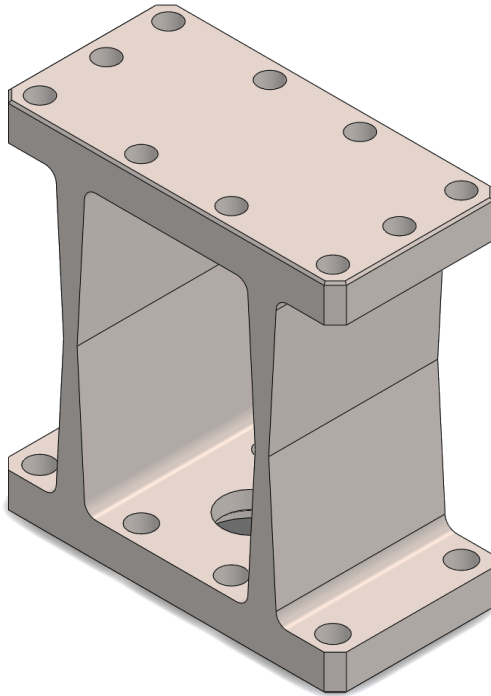
Figure 4.19: Original intermediate wedges (with bolts)   *Figure 4.20: Original intermediate wedges (without bolts)*
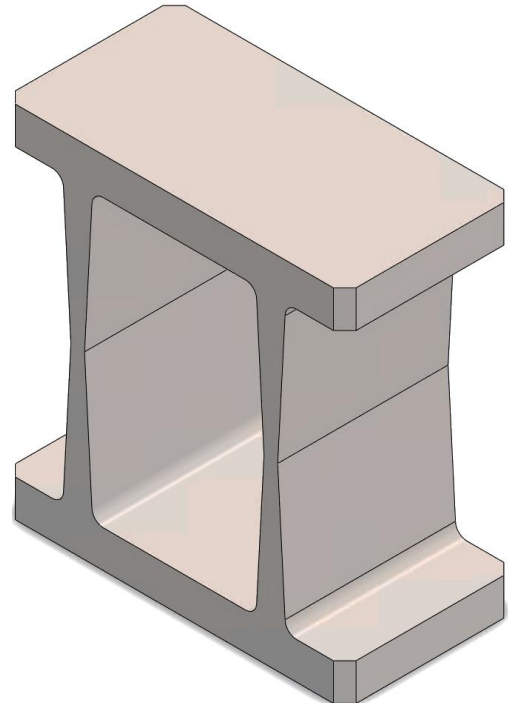
4.4.2.   Prototype Construction

For the moment, all types of wedges are designed to be manufactured through **CNC machining** because it provides highly accurate parts with tight tolerances and excellent material properties. In the next section, as explained in [15], we are going to describe its basics, how to design parts, the most popular materials and finishes, and some cost reduction tips.

4.4.2.1.   The Basics

CNC (Computer Numerical Control) machining is a **subtractive manufacturing technology**: parts are created by removing material from a solid block (blank or workpiece) using a variety of cutting tools.

In addition, it is a **digital manufacturing technology**: it produces high-accuracy parts with excellent physical properties directly from a CAD file. Due to the high level of automation, CNC is price-competitive for both one-off custom parts and medium-volume productions.

The basic CNC process can be divided into 3 steps. Firstly, the engineer designs the CAD model of the part. Secondly, the machinist turns the CAD file into a CNC program (G-code) and sets up the machine. Finally, the CNC system executes all machining operations with little supervision, removing material and creating the part.

Types of CNC machines

CNC Machining	3 axis	**Milling machines** — manufacture parts with relatively simple geometries, excellent accuracy and at low costs. The workpiece is held stationary while tools rotate at high speed and are attached to a spindle, which can move along 3 linear axes.
		Turning/ Lathering machines — have the lowest cost per unit but are only suitable for part geometries with rotational symmetry. The workpiece is held on the spindle while rotating at high speed and the tool just moves along polar directions (radially and lengthwise).
	Multi axis	**Indexed 3+2 axes** — manufacture parts quickly and with very high accuracy by using features that do not align with one of the main axes. During machining, the cutting tool can only move along three linear axes. Between operations the bed and the toolhead can rotate.
		Continuous 5 axis — manufacture parts with highly complex, 'organic' geometries and smooth contours, but at high costs. The cutting tool can move along three linear and two rotational axes relative to the workpiece. All five axes can move at the same time.
		Mill-turning — combine the benefits of CNC turning and CNC milling into a single system to manufacture complex parts at a lower cost than other 5-axis CNC systems.

4.4.2.2.   Materials for CNC Machining
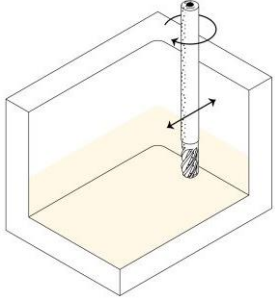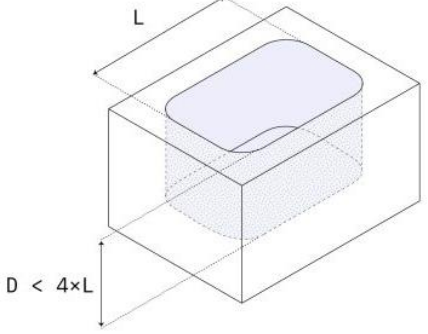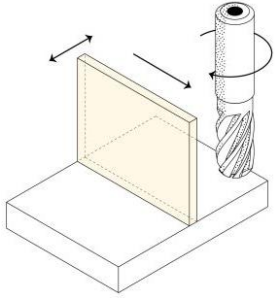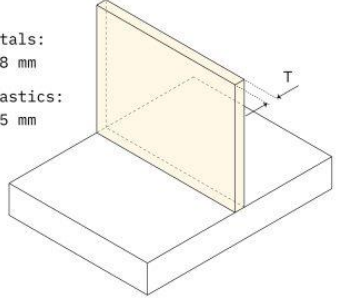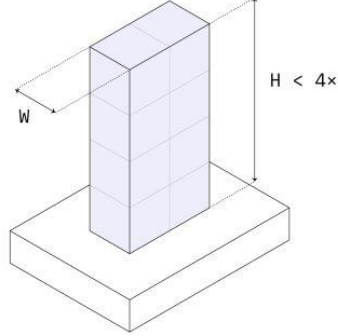
Almost every material can be CNC machined. The most common examples include metal and plastic. Foam, composites and wood can also be machined.
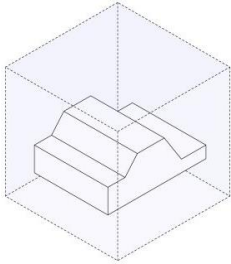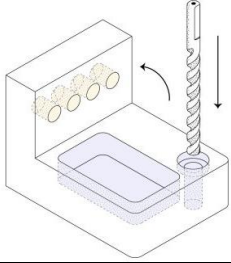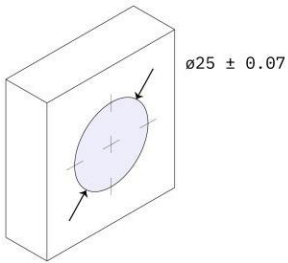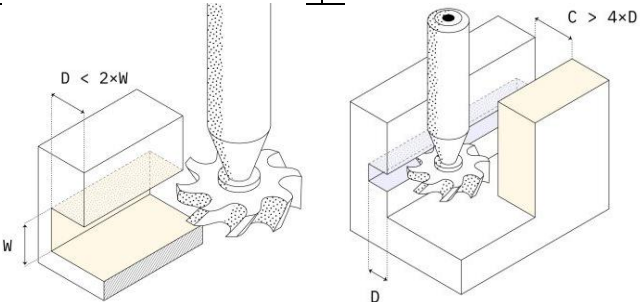
Focusing on the two materials chosen for the study, we notice that the machining cost for stainless steel is lower than for titanium alloys.

4.4.2.3. Design for CNC Machining

The design restrictions in CNC machining are a natural result of the mechanics of the cutting process and in particular:

DESIGN RESTRICTIONS			ACTIONABLE DESIGN RULES	
Tool geometry		Most CNC machining cutting tools have a cylindrical shape with a flat or spherical end, restricting the part geometries that can be produced.	**Internal edges**	**Recommended:** larger than ⅓ of the cavity depth. **Feasible radius:** Edges on the floor of a cavity should be either sharp or have a 0.1 – 1 mm radius.
Tool access		Surfaces that cannot be reached by the cutting tool, cannot be CNC machined.	**Holes**	**Recommended diameter:** standard drill bit sizes (conical floor). Holes with a non-standard diameter will be machined with an end mill tool (flat floor). They should be treated as cavities. **Min. diam. recommended:** 2.5 mm **Min. diam. feasible:** 0.5 mm **Recommended depth:** 4 times the DIA **Max. depth:** 10 times the DIA
			Threads	**Recommended length:** 3 times the DIA **Recommended size:** M6 or larger **Feasible size:** M2

Tool stiffness		Like the workpiece, the cutting tool can also deflect or vibrate during machining. This results in looser tolerances and even tool breakage.	**Cavities, pockets & non-standard diameter holes**		**Recommended depth:** 4 times the cavity width **Feasible depth:** 10 times the tool diameter or 25 cm
Workpiece stiffness		Due to the cutting forces and the temperatures developed during machining, it is possible for the workpiece to deform or vibrate.	**Minimum wall thickness**		**Recommended:** 0.8 mm (for metals) **Feasible:** 0.5 mm **Recommended:** 1.5 mm (for plastics) **Feasible:** 1.0 mm
			Tall features		**Recommended max. ratio:** height/ width < 4

ACTIONABLE DESIGN RULES			
General settings	**Maximum part size**		**CNC milling:** 400 mm x 250 mm x 150 mm (typically) **CNC turning:** Ø 500 mm x 1000 mm (typically) Very large CNC machines can produce parts with dimensions up to 2000 mm x 800 mm x 1000 mm. 5-axis CNC machining systems typically have a smaller build volume.
	Workholding		The geometry of a part determines the way it will be held on the CNC machine and the number of setups required. This has an impact on the cost, but also the accuracy of a part. For example, manual repositioning introduces a small, but not negligible, positional error. This is a key benefit of 5-axis versus 3-axis CNC machining.
	Tolerances		**Standard:** ± 0.125 mm (.005'') **Feasible:** ± 0.025 mm (.001'') Tolerances should be defined on all critical features, but **DO NOT** over-tolerance. If no tolerance is specified in the technical drawing, then the standard ± 0.125 mm will be held.
Undercuts			Undercuts can be machined using special T-shaped, V-shaped or lollipop-shaped cutting tools. **Recommended width:** 3 mm to 40 mm **Max. Depth:** 2 times the width **Recommended min. clearance:** 4 times the depth

5. Finite Element Method

When it comes to carry out the numerical model of the wedges, we will use the **Finite Element Method** (FEM). On the one hand, it will lead to the analysis of forces, stresses, and strains in order to meet the requirements. On the other hand, it will allow us to optimise their form maximising efficiency, defined as the relationship between maximum strength and the weight of the wedges.

ANSYS Workbench software will used for the simulation. Then, in order to obtain realistic results from the model, correct boundary conditions, idealisations, and a suitable mesh must be implemented.

Mainly three types of analysis will be carried out: the Static Structural, the Eigenvalue Buckling and the Steady-State Thermal. This leads to the creation of three models. Two of them, *Original model* (Figure 5.1) and *Simplified model* (Figure 5.2), for the Static Structural analysis. The remaining one, in which one intermediate wedge is isolated (Figure 5.3), for the Eigenvalue Buckling and Steady-State Thermal analyses.

In this chapter, only the *Original* and *Isolated* models will be explained. The *Simplified* model will be developed in the section 7.1.3.1, since it is a simplification of the *Original* model created for the hinged version of the intermediate wedges.

The *Original* and *Isolated* models mainly differ in the model limits, boundary conditions, idealisations and mesh size.
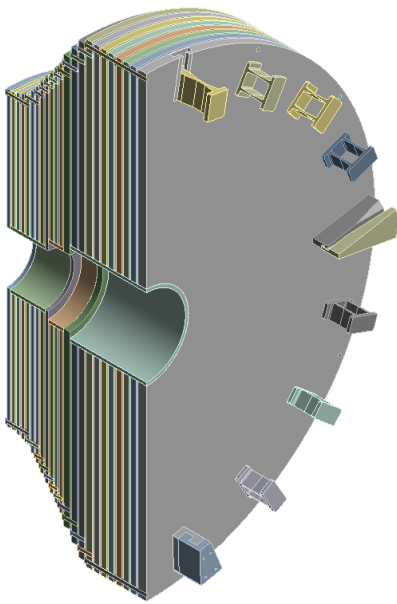
Figure 5.1 : Original model   *Figure 5.2 :* Simplified model   *Figure 5.3 :* Isolated model
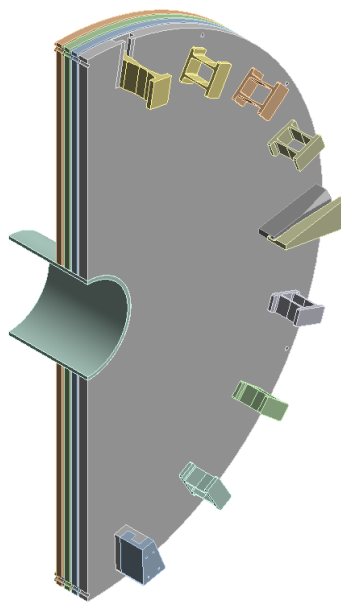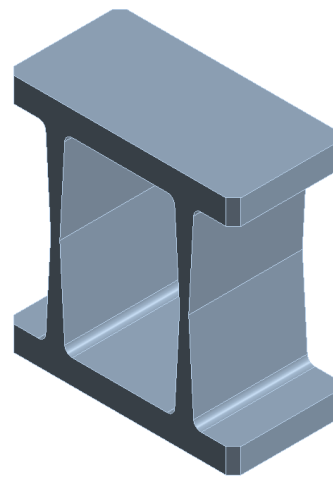
5.1.   Model Limits and Boundary Conditions. Idealisations

5.1.1.   Original Model

The *Original* model is the one used in the Static Structural analysis to evaluate the forces, stresses, and strains of the fixed intermediate wedges.

5.1.1.1.   Model Limits

As a limit of the model, we have considered the HGCal endcap represented by the CE-H absorber's structure without the back flange and cassettes (that will be represented as distributed mass elements). This means that tie rods, bolts, pins, spacers, inner cylinders, absorbers and wedges will be the only parts incorporated into the model. In addition, the CE-E will be simplified as a remote force.

5.1.1.2.   Boundary Conditions

The boundary conditions will define how the intermediate wedges will behave in relation to its environment. Table 5.1 shows how geometries are related to each other and its immediate surroundings. Also, together with Table 5.2, it is specified how these relationships are defined in ANSYS: type, value, and processing time.

Table 5.1: Geometries' relationships and ANSYS definition

	CE-E	CE-H						
		Tie rods	Bolts	Pins	Spacers	Inner cylinders	Absorbers /Cassettes	Wedges
Remote force	Self-weight							
Acceleration		Self-weight						
		Magnetic force						
Thermal condition		Thermal condition						
Bolt pretension		Pretension						
Bonded connection		back disk	back absorbers	absorbers	back absorbers	absorbers	inner cylinders	back disk
Frictional connection (0.2)		absorber 15	front absorbers/ CE-E backdisk		front absorbers/ CE-E backdisk			
Frictionless connection								*12, 3, 6 & 9*
Fixed support								back flange

Table 5.2: ANSYS definition of the type, value, and processing time of the forces in the system

Steps	CE-E	CE-H						
		Tie rods	Bolts	Pins	Spacers	Inner cylinders	Absorbers /Cassettes	Wedges
0) Preload		280 kN	M36: 280 kN M30: 180 kN	0 kN				
1) + Lock		True						
2) + Gravity acceleration		Y: -9.806 m/s²						
3) + Remote force	Y: -200 kN							
4) + Magnetic acceleration		Z: 5.5 m/s²						
5) + Thermal condition		-35 °C						

Forces' definition

The definition of the forces acting on the system is divided into 5 steps:

1) **Pretension (preload + lock).** When a load is applied to a joint containing a tightened bolt it does not sustain the full effect of the load but usually only a small part of it. Then, maintaining a high initial bolt preload is essential to ensure that a bolted joint will survive. [16] Depending on the geometry, the value changes and is calculated as half of the existing maximum preload.

2) **Gravity acceleration.** According to our coordinate system, a negative acceleration is set to simulate gravity.

3) **Remote force.** For simplifying the model, the CE-E is represented by a force applied to the centre of gravity of the part. As the weight of the CE-E is estimated to be around 20 t, the force will have a value of approximately 200 kN.

4) **Magnetic acceleration.** As a result of the induced magnetic field and manufacturing defects, a magnetic force of 100 kN is created. This means that if we place the stainless steel structure horizontally, its fictitious weight would decrease from 180 t to 100 t. Then,

$$100\ t \cdot 9.81\ \frac{m}{s^2} = 180\ t \cdot a_m \Rightarrow \boldsymbol{a_m = 5.5\ \frac{m}{s^2}} \qquad (Eq.\ 5.1)$$

5) **Thermal condition.** It is determined since the whole structure is cooled down to -35 ℃.

Connections

Four types of connections are described in this model:

- **Bonded.** Specifies that no sliding or separation between faces or edges is allowed [17].
- **Frictional.** Defines contact where the surfaces can freely slide in the tangential direction relative to each other. It is mandatory to enter a friction coefficient. [17]
- **Frictionless.** If the friction coefficient is zero [17].
- **Fixed support.** Blocks all degrees of freedom so that the selected part of the model will not be able to move at all [18]. In this case, this condition is imposed only on the wedges, which are fixed to the back flange.

5.1.1.3. Idealisations

Several idealisations have been considered in order to analyse the model in a simpler way and without the conclusions being significantly affected.

First of all, the HGCal model has been simplified by imposing the **symmetry condition**, and **reducing** the number of **geometries** and **boundary conditions** (Figure 5.4).

On the one hand, the Endcap Timing Layer (ETL), the Particle Moderator (PM) and the CE-E are represented by a force applied to the centre of gravity of the group. According to Saint-Venant's principle, "the difference between the effects of two different but statically equivalent loads become very small at sufficiently large distances from load" [19]. Then, the system can be summed up in a point of application. In addition, the force must be uniform and constant.

On the other hand, some joints, the Muon Chambers (ME0), the brackets, the flexible ring and the thermal screen do not appear in the model because they do not play an important role in the analysis.

Finally, cassettes are defined as a distributed mass in their corresponding absorbers, and the back flange is replaced by a fixed support condition.

Second of all, in this preliminary design of the intermediate wedges, it can be considered that the **state of the stresses** is flat. However, it is possible that the already designed wedges have a complex 3D geometry. Therefore, making this idealisation will no longer make sense (see section 6.1.2).

To conclude, all **deformations** computed by the program are **elastic**. Nevertheless, in reality when the elastic limit is exceeded, the $\sigma - \varepsilon$ curve loses its linearity.

A	Tie rods Pretension
B	Bolts Pretension
C	Pins Pretension
D	Gravity + Magnetic Acceleration
E	CE-E Weight Remote Force
F	Thermal condition
G	Symmetry condition
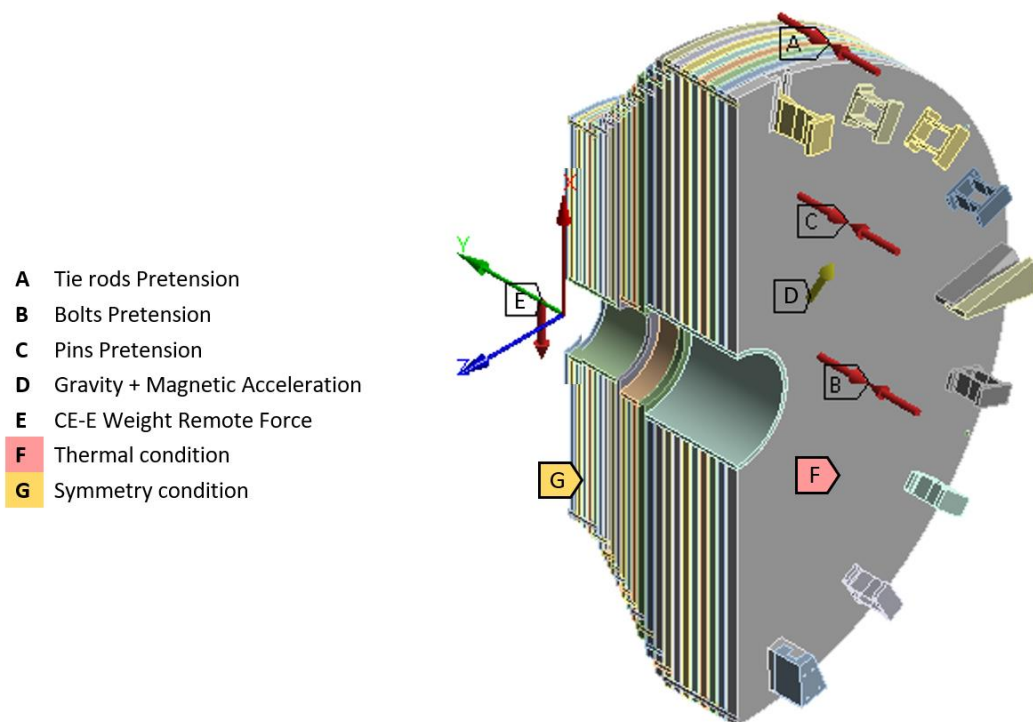
Figure 5.4 : Represented geometries, applied forces and symmetry condition [ANSYS]

5.1.2.   Isolated Model

The *Isolated* model is the one used in the Eigenvalue Buckling and Steady-State Thermal analysis to evaluate the load multiplier and energy dissipated by a piece.

5.1.2.1.   Model Limits

As a **limit of the model**, an isolated intermediate wedge has been considered.

5.1.2.2.   Boundary Conditions

Eigenvalue Buckling hyperstatic analysis

Several buckling analyses can be defined to check if the slender shape of the arms will withstand a certain amount of compression force. Nevertheless, the most extreme is the one in which only three wedges (because three points define a plane) support the whole weight of the structure in the assembly position.

Numerically talking, it means that the isolated intermediate wedge will have to support a compression force of 653,730 N or 67 t (Eq. 5.2).

$$A = \frac{200e + 003\,kg \cdot 9.806\,{}^{m}/_{s^2}}{3} = 6.5373e + 005\,N \qquad \text{(Eq. 5.2)}$$

Steady-State Thermal analysis

The Steady-State Thermal analysis has been created to calculate the amount of energy dissipated through an isolated intermediate wedge.

Concerning the boundary conditions, it is assumed that all the surfaces except the one in contact with the back disk cooled down to $-35\,°C$ are subjected to convection with air at room temperature.
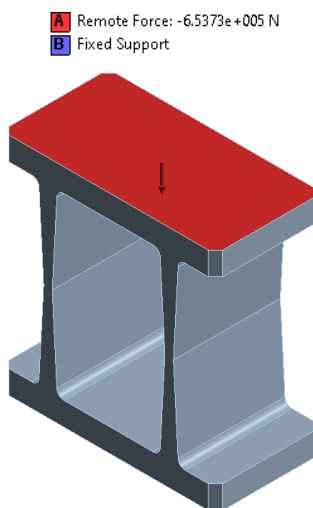
Figure 5.5 : Eigenvalue Buckling analysis [ANSYS]   *Figure 5.6 :* Steady-State Thermal analysis [ANSYS]
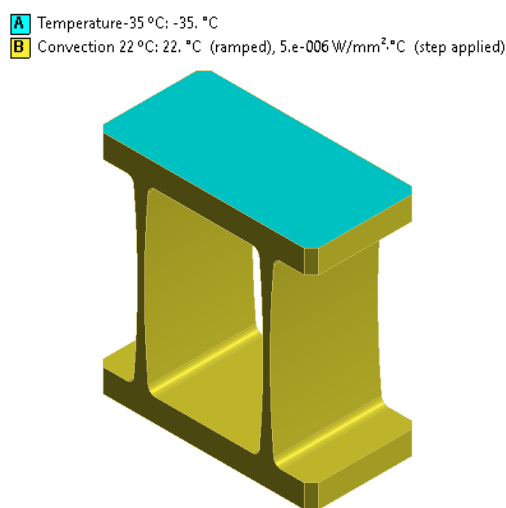
5.1.2.3.   Idealisations

In this case, the model has been reduced to a part. Therefore, the boundary conditions are applied to surfaces, simplifying the entire model into a Remote Force or a Temperature condition. In addition, the state of the stresses and deformations will remain as in the original model.

5.2. Model Features: Finite Element Type, Materials' Model and Mesh

5.2.1. Finite Element Type

Firstly, due to the geometry of the piece, a 3D solid mesh will be created.

Secondly, as a result of a technical limitation of the software and in order to be able to refine those areas where critical results appear, a mesh of **quadrilateral interpolated tetragonal elements** needs to be defined (Figure 5.7). Moreover, a smaller element size will be achieved by saving calculations.
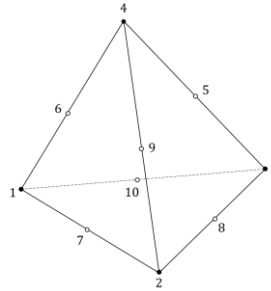
Figure 5.7: Quadratic tetrahedron with 10 nodes

5.2.2. Materials' Model

Ideally the material has to be **linear**, **elastic** and **isotropic**. In other words, when a force is applied, the material has to deform linearly and, when it stops, it returns to its initial state. Besides, the properties do not depend on the direction in which they are examined (Table 4.7).

5.2.3. Mesh

The **mesh** is decisive in defining the results of the simulation. A denser mesh provides more accurate results, but needs more computational time. In contrast, a sparse mesh provides a time-efficient result, but it is less accurate. Our goal is to find the best compromise between these two aspects.

Then, we have to decide the overall **mesh density**. Starting from a sparse mesh, the size of the elements has been progressively reduced until the results of the simulation have ceased to vary and converged towards the exact solution. These tests have always been done with the same requests by comparing the equivalent Von Mises stress for the same point (Figure 5.8).
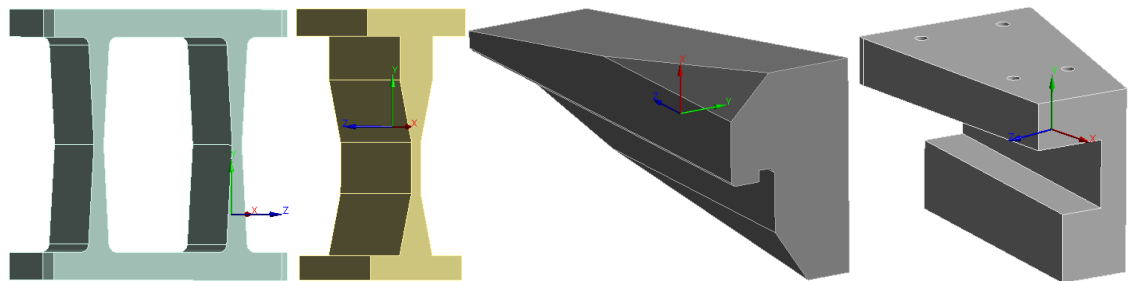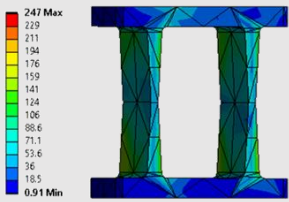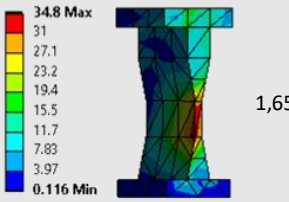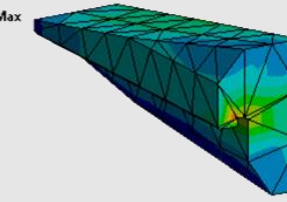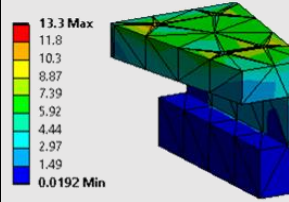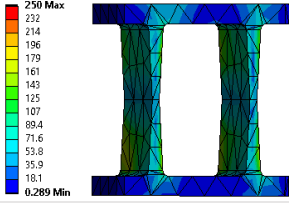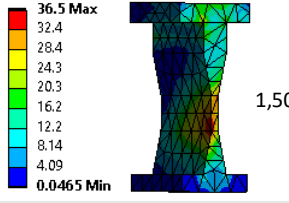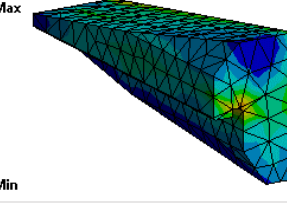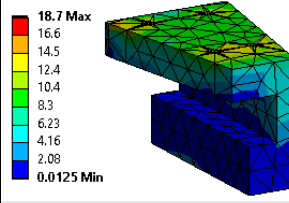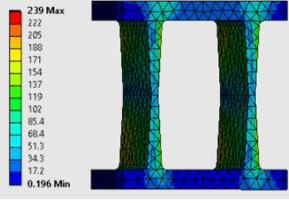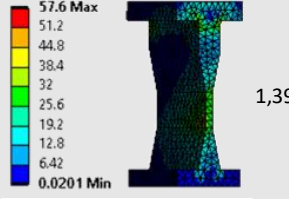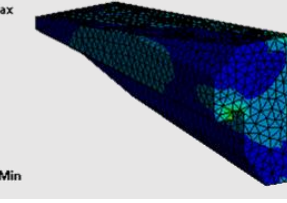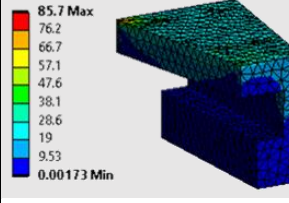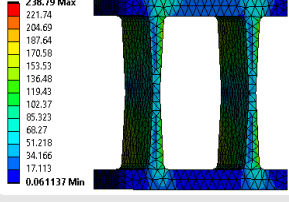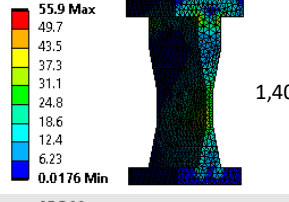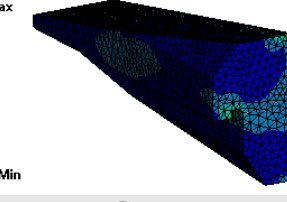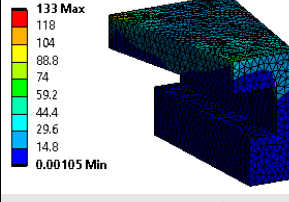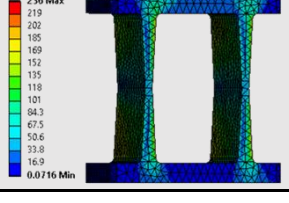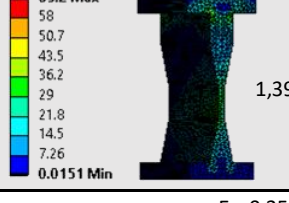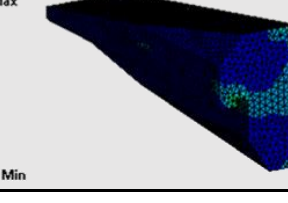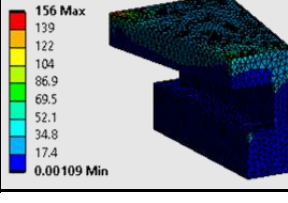
Figure 5.8: Study point of the different wedges (intermediate, 12, 3 & 9 and 6 o'clock) [ANSYS]

The criterion for deciding how much the elements' size needs to be reduced is to be able to stabilise the first 2 digits of the obtained stress at the study point. Table 5.3 shows for each mesh size the Equivalent Stress Distribution and the Stress probe of the four types of wedges.

Table 5.3: Iterations to determine mesh density [ANSYS]

Mesh size [mm]	Intermediate wedges		12 o'clock wedges		3&9 o'clock wedges		6 o'clock wedges	
	Equivalent Stress Distribution	Stress probe [Pa]	Equivalent Stress Distribution	Stress probe [Pa]	Equivalent Stress Distribution	Stress probe [Pa]	Equivalent Stress Distribution	Stress probe [Pa]
100		4,34E+07		1,65E+07		3,05E+07		6,22E+05
50		5,45E+07		1,50E+07		2,87E+07		7,91E+05
20		5,40E+07		1,39E+07		3,20E+07		1,86E+06
15		5,29E+07		1,40E+07		3,40E+07		2,08E+06
13		5,24E+07		1,39E+07		3,45E+07		2,14E+06
	E= 0,9124%		E= 0,3517%		E= 1,5018%		E= 2,8895%	

From the results, we conclude that an element size of **15 mm** will be used for the four types of wedges. Firstly, in the subsequent mesh decrease, approximating the results, the first 2 digits of the stress probe have remained constant. Secondly, the relative errors (Eq. 5.3) between the mesh size of 15 mm and the one of 13 mm are negligible.

$$E = \frac{\left| \sigma_{eq,13} - \sigma_{eq,15} \right|}{\sigma_{eq,13}} \cdot 100$$

(Eq. 5.3)

After running a first analysis with this mesh size, refinements are required in the areas where the maximum stresses are found to predict the exact value.

5.3. Maximum Displacement Under Nominal Load. Validity of the Linearity and Small Displacement Hypothesis

5.3.1. Maximum Displacement Under Nominal Load

Figure 5.9 shows the total deformation distribution of the wedges. In particular, it is observed that the intermediate wedges are the most deformed because they lack degrees of freedom in the radial direction (they are fixed to the back disk and the back flange).The maximum value reached is 2.6233 mm.
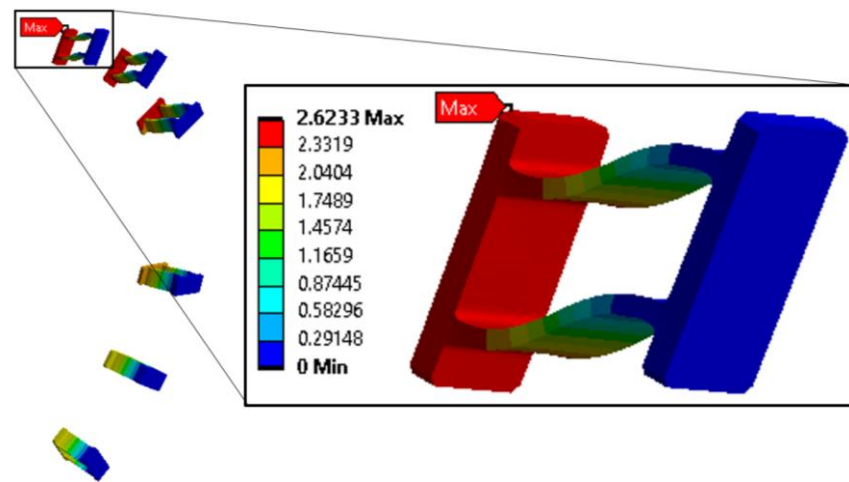
Figure 5.9: Total deformation [mm] distribution of the wedges [ANSYS]

5.3.2. Validity of the Linear and Small Displacement Hypothesis

Geometrically, wedges can behave in a non-linear way. Therefore, when evaluating the linear hypothesis, it will be necessary to validate that the displacements are small enough compared to the wedges' dimensions. This can be done in two ways:

1) **Intuitively**, it can be verified that, compared to the dimensions of the piece, the maximum displacement of 2.6233 mm is negligible.
2) **Analytically**, it can be validated by comparing the results of a linear analysis with a nonlinear one. The nonlinear analysis consists of an iterative calculation updating the geometry, and redefining the direction of the force, which will rotate with the part. Specifically, the equivalent Von Mises stress values are being compared at the same point it was used to determine the mesh size (Figure 5.8). These are the obtained results:

- With linear hypothesis: 238.79 MPa
- Without linear hypothesis: 242.92 MPa

$$E = \frac{|242.92 - 238.79|}{242.92} \cdot 100 = 1.70\%$$

(Eq. 5.4)

This discrepancy is small enough to allow the use of the small deformation hypothesis and thus reduce the required calculation time.

6. Result Analysis

6.1. Operational Position

6.1.1. Displacement Field. Evaluation of Maximum Displacement Under Nominal Load

As seen above, Figure 5.9 shows the wedges' total deformation distribution. Below, in Figure 6.1, the directional deformation distribution of the wedges is presented.

As it could be predicted, displacements are smaller near the back flange and larger close to the back disk mainly due to the thermal condition. In addition, an asymmetry in the results among the wedges located between 12 and 3 o'clock, and those found between 3 and 6 o'clock can be observed. This happens because the endcap is not completely fixed by the back flange and part of the structure gives way, moving the axis of rotation below the imaginary line drawn between 3 & 9 o'clock wedges.

In conclusion, the maximum offset is 2.6233 mm, which represents 0.87% of the total width of the intermediate wedges.
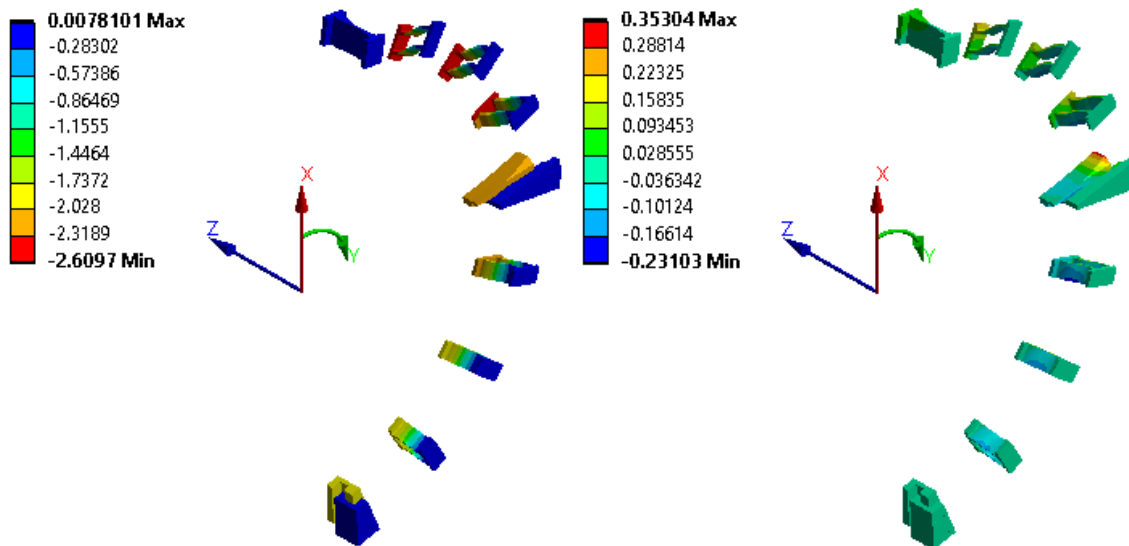
Figure 6.1: Directional deformation [mm] of the wedges. (Right) Thermal condition – X Axis or Radial component, negative is towards the centre. (Left) Magnetic condition – Z Axis or Axial direction, positive is towards the interaction point [ANSYS]

6.1.2.   Principal Stress Distributions

By observing the principal stress distributions, we will know which regions of the part are under tension and compression. For the whole analysis, the selected instant is the one in which the stresses are maximum, i.e. the last one.

In general, from the images, a **symmetrical distribution** of the stresses can be observed. On the one hand, the areas under pure traction or compression are concentrated in the depth, specifically in the rounded edges and surroundings (Figure 6.2 and Figure 6.3). On the other hand, at the bases, most elements are under traction and compression at the same time.

Finally, in Figure 6.4 a distortion and a 3D phenomenon can be seen. Consequently, it is shown that the flat state of stresses cannot be assumed even in the preliminary design.
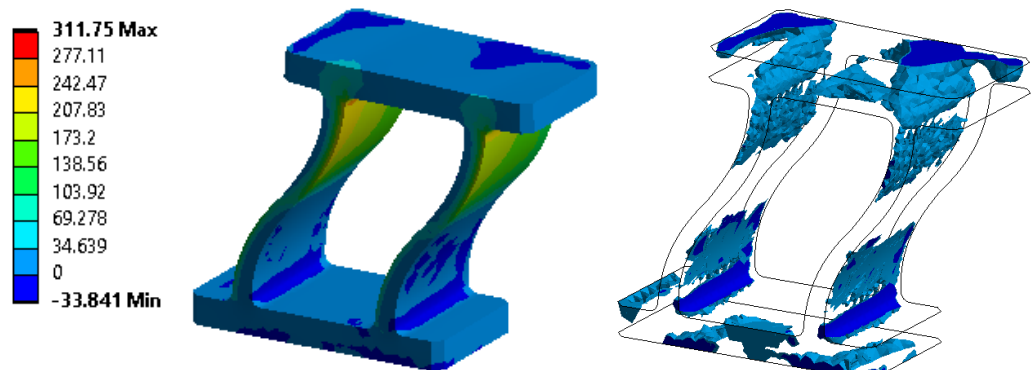
Figure 6.2: (Left) Maximum Principal Stress [MPa] distribution. (Right) Compressed areas ($\sigma_I \leq 0$) [ANSYS]
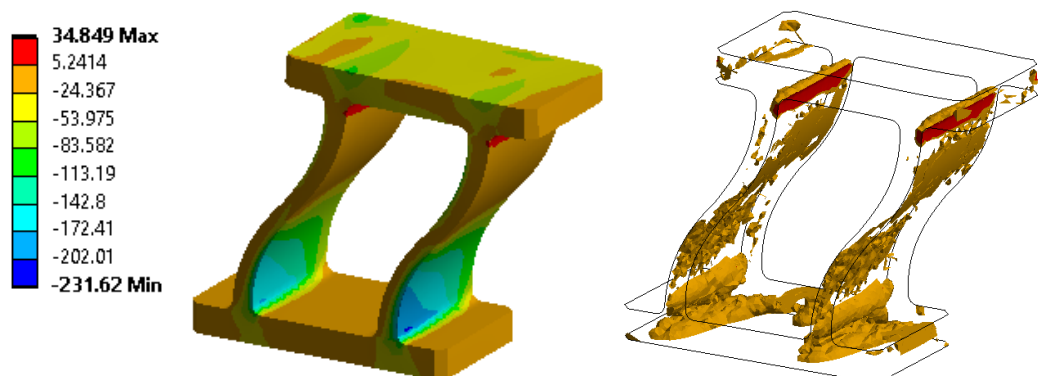
Figure 6.3: (Left) Minimum Principal Stress [MPa] distribution. (Right) Areas under traction ($\sigma_{III} \geq 0$) [ANSYS]
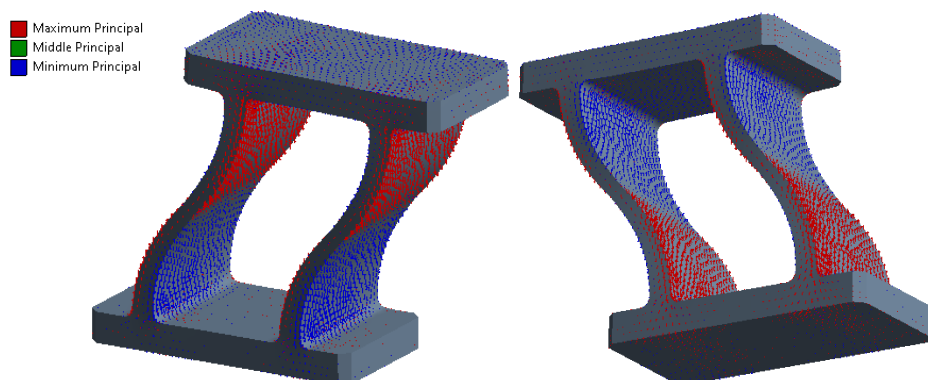
Figure 6.4: Vector Principal Stress [ANSYS]

6.1.3.   Equivalent Stress Distribution

On the one hand, titanium is a ductile material. This rules out Rankine's failure criterion, which only applies to brittle materials.

On the other hand, between choosing the Tresca-Guest criterion and the **Von Mises** one, we finally opted for the latter, because the angular shape of Tresca's criterion in the space of stresses does not reflect well the complexity and variability of materials' behaviour [20].
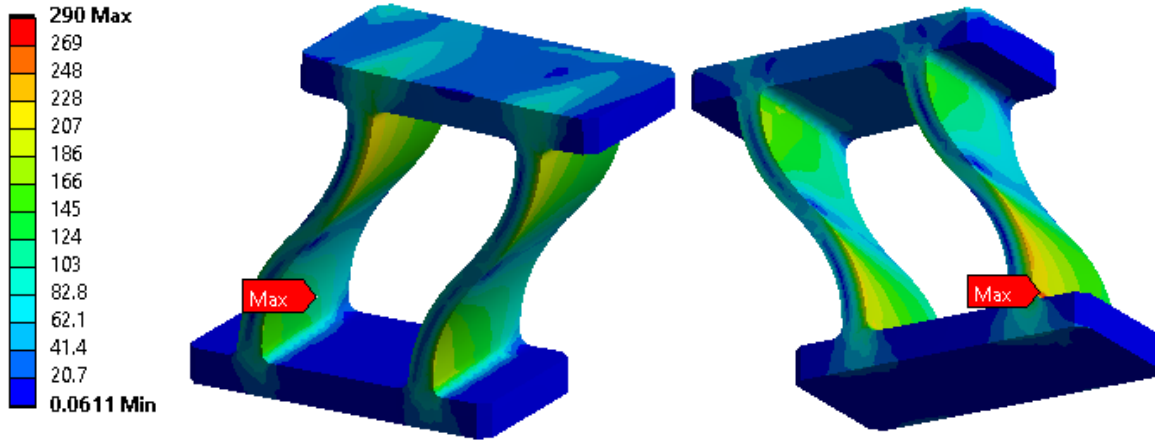
Figure 6.5: Equivalent Stress [MPa] Distribution (Von Mises criteria) [ANSYS]

As shown in Figure 6.5 and confirming the results above, the areas of the wedges where the maximum stress is concentrated are the rounded edges subjected to traction.

6.1.4.   Failure Criteria

The maximum equivalent stress of the preliminary design is 290 MPa, a value below the tensile yield strength limit of our material (930 MPa). Then, the safety factor is defined as follows:

$$\gamma_s = \frac{930}{290} = \mathbf{3.2}$$

(Eq. 6.1)

A value slightly above the established limits.

6.1.5.   Force Reaction

In the next section, firstly, the loads in x, y and z for all wedges were calculated based on the applied conditions (Figure 6.6).

On the one hand, we verify that the theoretical values of the gravity and magnetic forces correspond to those obtained from the analysis with a relative error of less than 1% (Eq. 6.3-4).

On the other hand, we observe that as we had predicted in section 4.3.2, due to the existence of the intermediate wedges, the total load supported by the main wedges (3 & 9) would lighten and they will only withstand 64.5% of the total weight (Eq. 6.2). As already said, one of the goals of the optimisation is to decrease the action of the weight on the intermediate wedges, as they have not been designed for supporting vertical loads.

$$\frac{\boldsymbol{Total\ weight}}{\boldsymbol{percentage}} = \frac{638110}{988286} \cdot 100 = \mathbf{64.5\%}$$

(Eq. 6.2)

x [N]	y [N]	z [N]
3832.7	1389.3	-45602
2489.9	1152.5	-94045
2614.7	1174.5	-83340

x [N]	y [N]	z [N]
36738	26645	-93140
36829	26894	-159170
15786	61485	-171860

x [N]	y [N]	z [N]
43346	57269	-38950
44978	59904	-89351
14400	86335	-93024

x [N]	y [N]	z [N]
30242	86923	-105430
28672	84089	-159220
-10103	94871	-155070

x [N]	y [N]	z [N]
0	621960	0
0	623920	-61219
0	638110	-64587

x [N]	y [N]	z [N]
-30305	91741	110590
-31492	93752	55731
-70760	83880	65035

x [N]	y [N]	z [N]
-41870	57927	31767
-39794	54976	-16012
-70734	28765	-23884

x [N]	y [N]	z [N]
-40110	30866	14034
-39334	30423	-40247
-57826	-5957.6	-29609

Gravity
+ Magnetic force
+ Thermal condition

x [N]	y [N]	z [N]
-60723	13721	126740
-58920	13338	65226
4867.5	-220.17	58028

Figure 6.6: Forces reactions for all wedges based on the applied conditions (gravity, gravity + magnetic force, gravity + magnetic force + thermal condition)

$$F_g = \sum_i y_{g,i} = 988441 \Rightarrow E = \frac{|980600 - 98441|}{980600} = 0.8\% \qquad \text{(Eq. 6.3)}$$

$$F_m = \sum_i y_{g,i} - y_{m,i} = 498316 \Rightarrow E = \frac{|495000 - 498316|}{495000} = 0.67\% \qquad \text{(Eq. 6.4)}$$

Secondly, it will be checked that the intermediate wedges behave as a double fixed beam.

In Figure 6.7, comparing the forces reaction resultants in both bases of the intermediate wedges, it was calculated that there is only a 0.09% of relative error.

In Figure 6.8, comparing the moment reaction x, y and z components, it can be calculated that there is a maximum existing relative error of 3.2%.

$$M_{x1} = M_{x2} + R_{y2} \cdot L = 7639100 + (-44414) \cdot 316.5 = -6417931 \, N \cdot mm \Rightarrow E = 0.2\% \quad \text{(Eq. 6.5)}$$

$$M_{y1} = M_{y2} - R_{x2} \cdot L = 15209000 - 45355 \cdot 316.5 = 854142.5 \, N \cdot mm \Rightarrow E = 3.2\% \qquad \text{(Eq. 6.6)}$$

$$M_{z1} = M_{z2} = -9082.3 \, N \cdot mm \Rightarrow E = 0.01\% \qquad \text{(Eq. 6.7)}$$

x [N]	y [N]	z [N]
-45184	44315	171750

$R_2 = 183210\ N$

$R_1 = 183040\ N$

x [N]	y [N]	z [N]
45355	-44414	-171870
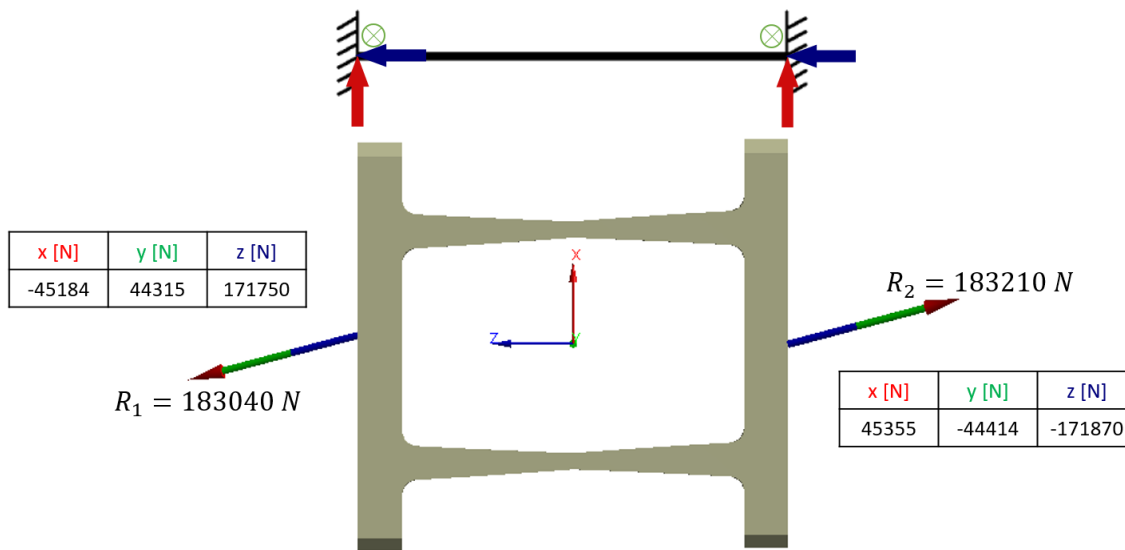
Figure 6.7: Double fixed beam model. Force reactions [ANSYS]

$M_1 = 6462800\ N \cdot mm$

$M_2 = 17020000\ N \cdot mm$

x [N·mm]	y [N·mm]	z [N·mm]
6402400	-881480	9082.2

x [N·mm]	y [N·mm]	z [N·mm]
7639100	15209000	-9082.3

$L = 316.5\ mm$
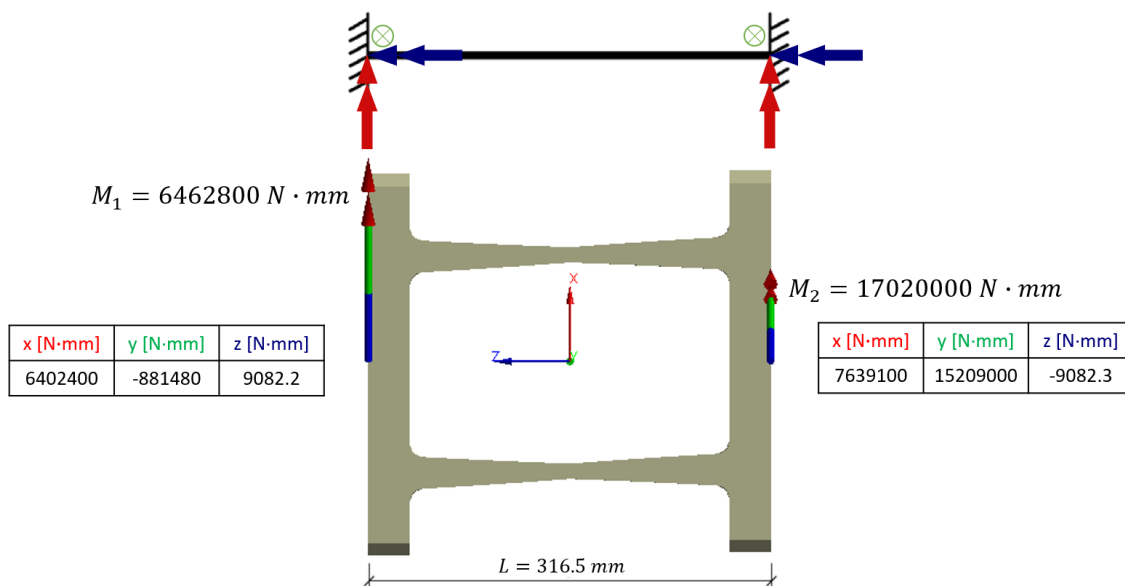
Figure 6.8: Double fixed beam model. Moment reactions [ANSYS]

6.1.6.   Thermal Analysis

On one side, the temperature distribution represented in Figure 6.9 shows that the temperature of the intermediate wedge varies from $-35\ ^\circ C$ to $7.4\ ^\circ C$.

On the other side, the piece only dissipates 52.34 W. This means that, in total, all the intermediate wedges will dissipate 628 W (Eq. 6.8).

$$\boldsymbol{Total\ energy\ dissipated} = 12 \cdot 52.34 = \boldsymbol{628\ W} \qquad \text{(Eq. 6.8)}$$
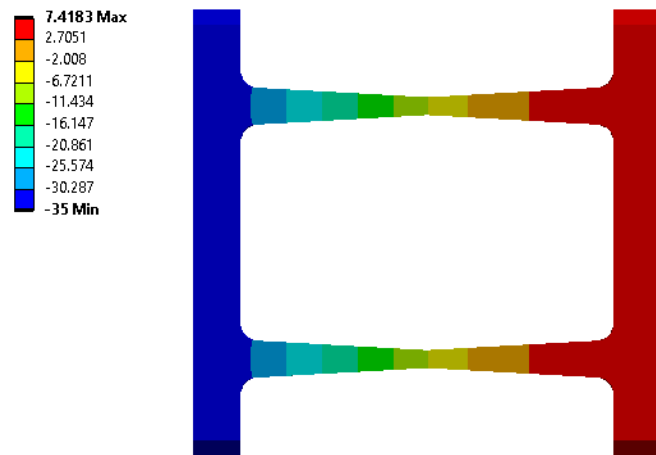
Figure 6.9: Temperature [°C] distribution [ANSYS]

6.2.   Assembly Position

6.2.1.   Buckling Analysis

The buckling analysis defines the load multiplier, a parameter used to calculate the buckling force. For this preliminary design, the load multiplier is 5.2282 and the buckling force is $3.4178e + 006\ N$ (Eq. 6.9) or $350\ t$. This will most likely never happen, but when the situation arrives the total deformation of the intermediate wedges will be the one shown in Figure 6.10.

$$\textbf{\textit{Buckling force}} = 5.2282 \cdot 6.5373e + 005\ N = \mathbf{3.4178e + 006\ N} \qquad \textit{(Eq. 6.9)}$$
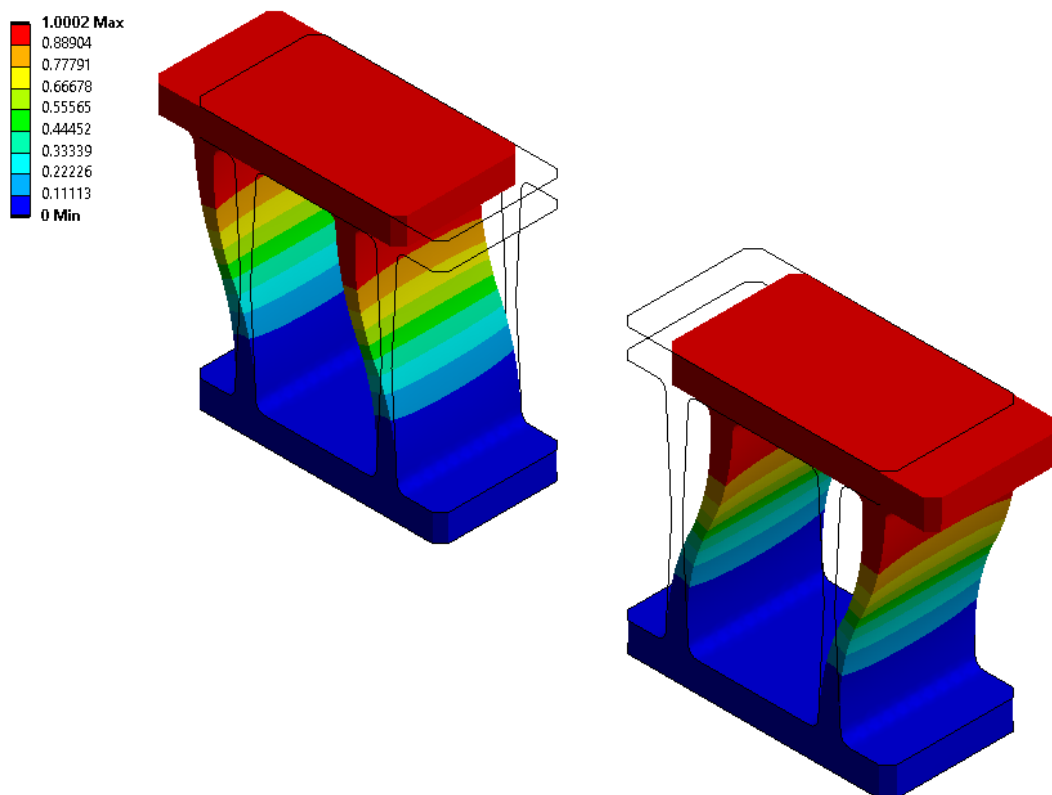
Figure 6.10: Buckling total deformation [ANSYS]

7. Design Optimisation

7.1. Design Optimisation Process

The main challenge of this project is to create an optimal configuration of the wedges for both the operational (vertical) and the assembly (horizontal) position. Optimal means that it has to complete the basic functions described in the section 4.1.1 without suffering permanent plastic deformation or buckling.

In the following Figure 7.1, magnified in the Annex B, the four different developed versions are shown: totally fixed, totally hinged, fixed-hinged and sliding. Pondering the pros and cons, the chosen configuration is the one in which fixed and hinged intermediate wedges are interspersed, because the plastic permanent deformation is not significant, they only take a 19% of the total weight and they will not buckle.
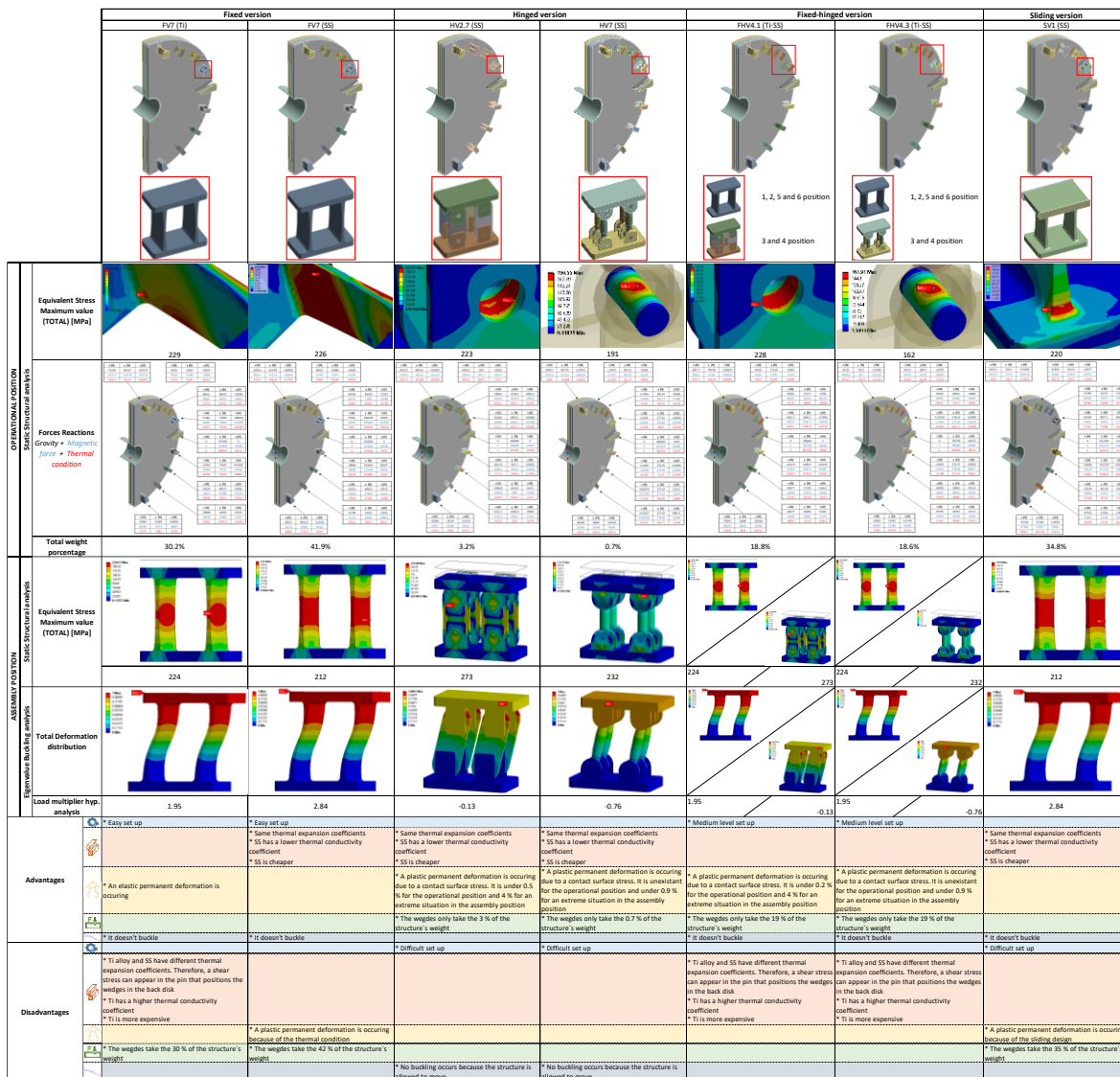
Figure 7.1: All versions comparison [ANSYS]

7.1.1. Hybrid Configuration Analysis

First of all, it is meant to find the hybrid configuration that achieves the best results. With this purpose, fixed (FV7) and hinged (HV2.7) intermediate wedges are symmetrically interspersed in the positions shown in Figure 7.2.

Analysing the six resultant configurations represented in Figure 7.3 it can be noticed that the maximum equivalent stress value is located in the 3rd or 4th intermediate wedge, and it is similar to the one of the totally hinged / fixed configuration. Numerically talking, the maximum relative errors are the ones expressed in (Eq. 7.1) and (Eq. 7.2). This means that the shapes of the fixed and hinged intermediate wedges can be optimised independently.

$$E_{max} = \frac{223 - 217}{223} \cdot 100 = 2.69\% \qquad \text{(Eq. 7.1)}$$

$$E_{max} = \frac{229 - 243}{229} \cdot 100 = 6.11\% \qquad \text{(Eq. 7.2)}$$

In addition, it is observed that the best configurations are the ones in which the fixed intermediate wedges are close to the vertical position and the hinged ones are near 3 & 9 o'clock wedges (FHV2, FHV3 and FHV4).

In conclusion, the chosen configuration is the **FHV4** because it is the one with less intermediate hinged wedges. On one side, this will facilitate the assembly. On the other, in case that the 3 & 9 o´clock wedges fail, the more intermediate fixed wedges there are, the better since they can take vertical loads.
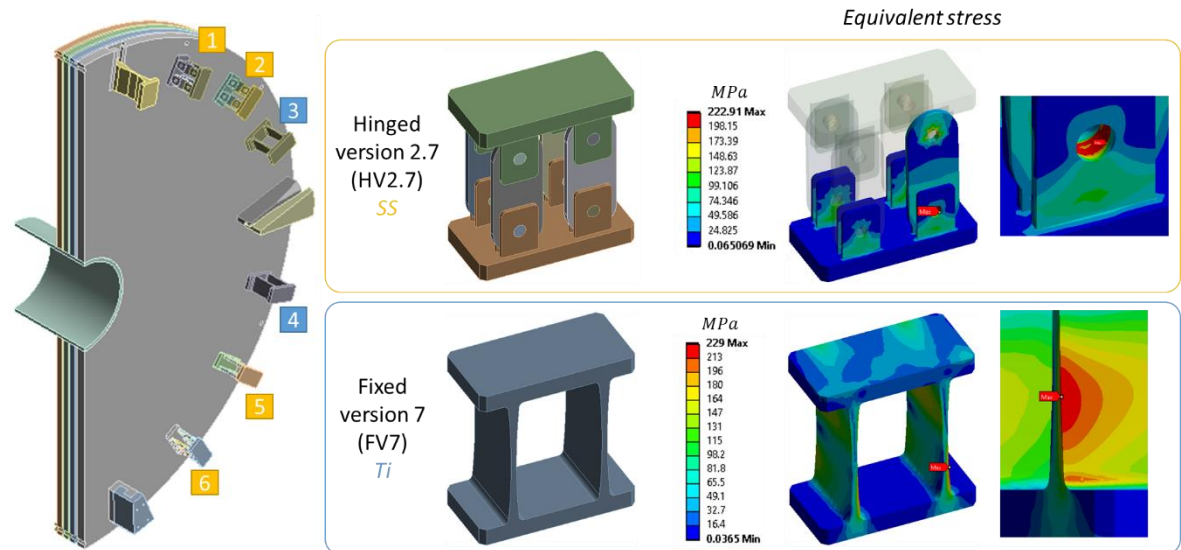
Figure 7.2: Hybrid configuration analysis settings [ANSYS]
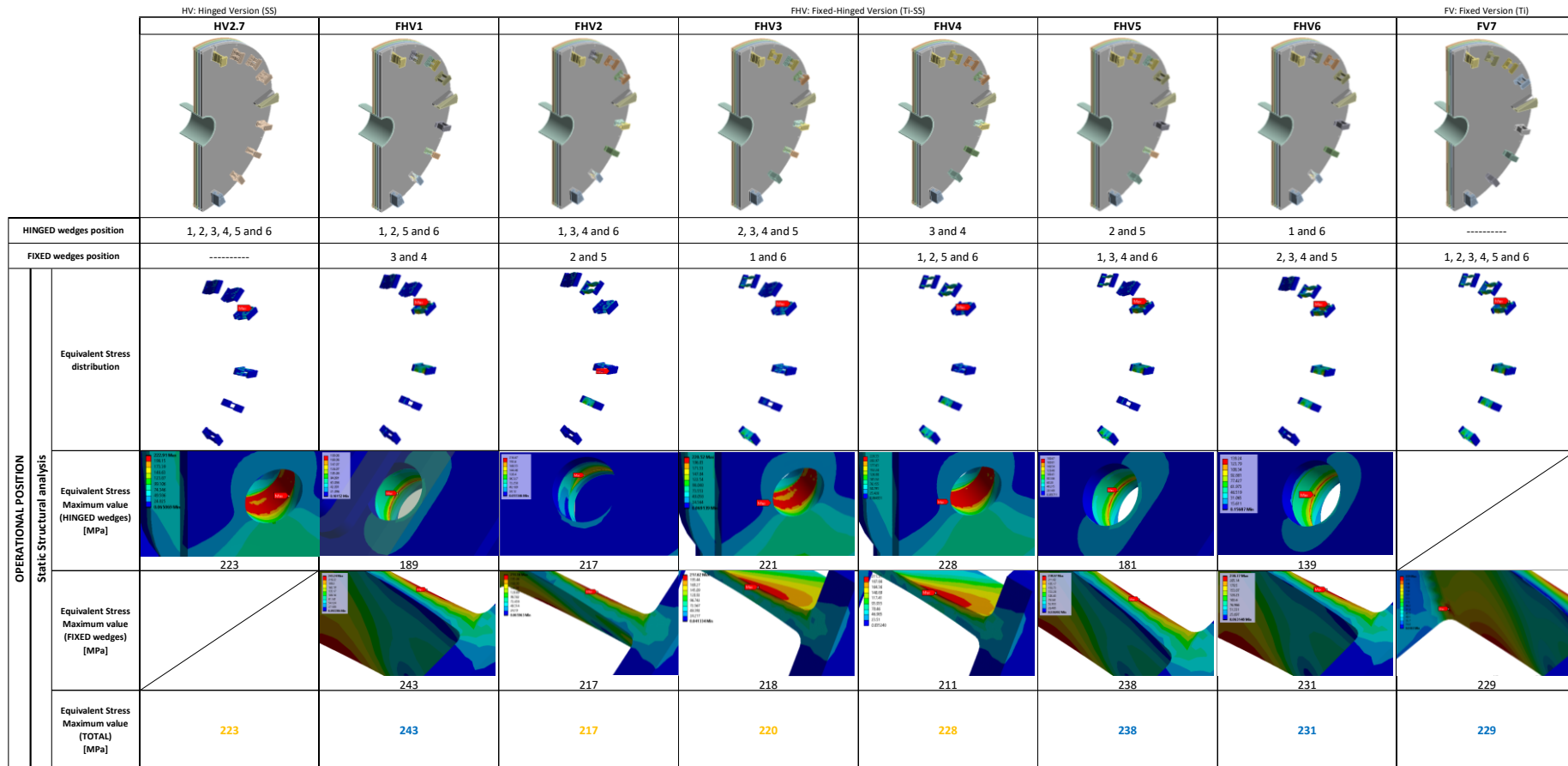
Figure 7.3: Hybrid configurations comparison [ANSYS]

7.1.2. Fixed Version Optimisation

Keeping the original volume of the piece ($300\ mm \times 316.5\ mm \times 150\ mm$) and the dimensions of the base ($42.5\ mm$ and $32.5\ mm$), the shape, thickness and fillet radius of the arms have been modified.

Summarised in Figure 7.4 and deepened in Annex C, it can be seen that, for lowering the equivalent stress maximum values, firstly arms become slimmer and curved. Secondly, the fillet radius becomes larger for spreading the stress. Finally, a third arm that lowers the stresses and reinforces the piece from buckling is added.

Comparing the static structural and buckling results, the chosen version of the fixed wedges is **FV7**, since it has one of the best result combinations and is easier to assemble.
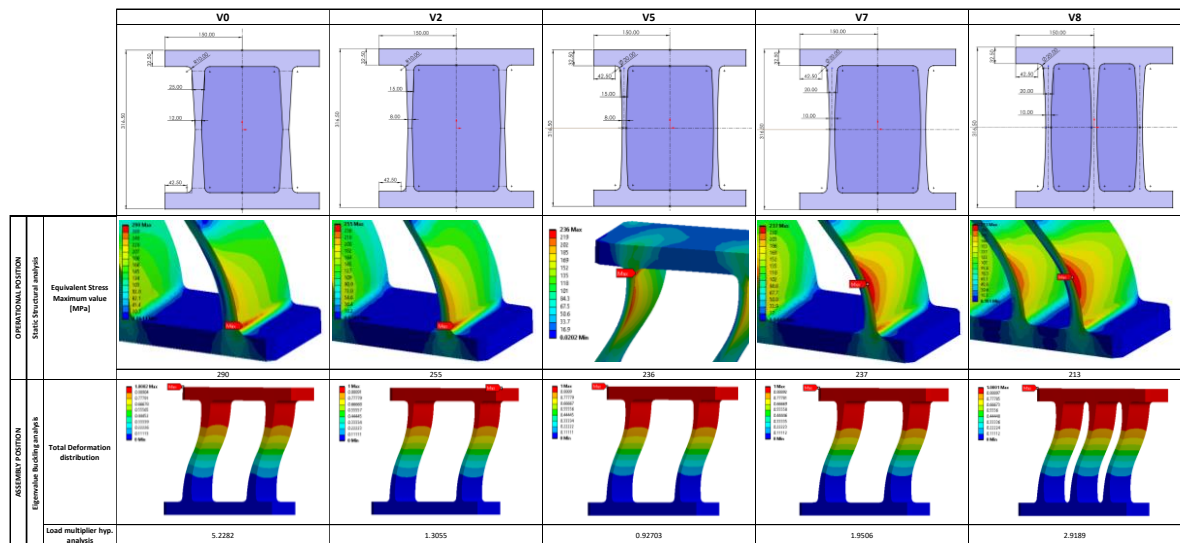
Figure 7.4: Fixed version optimisation [ANSYS]

7.1.3. Hinged Version Optimisation

7.1.3.1. Simplified hinged model

Initially, the main difference between the original ANSYS model and the hinged one was that the number of connections increased by 144 units. This caused an unknown error (Figure 7.5) related to the computational time.
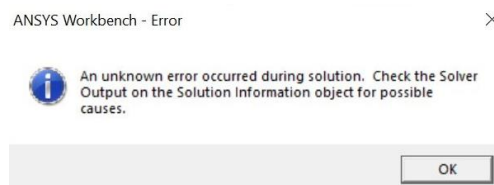
Figure 7.5: ANSYS Workbench – Error [ANSYS]

A reduction of the number of elements (new mesh) allowed to run the analysis. Nevertheless, the time to solve the model was over two hours. To minimise it and speed up the optimisation process, several simplified models were created. In the following tables (Table 7.1, Table 7.2 and Table 7.3) a comparison of the models is shown. The number of absorbers is varying from one model to another. The comparison parameters are the total deformation and equivalent stress maximum values.

Table 7.1: Comparison of the different models with the original fixed version (V0) of the intermediate wedges
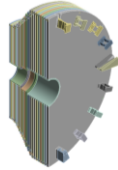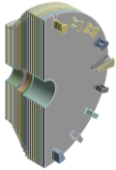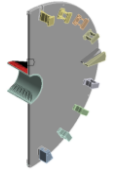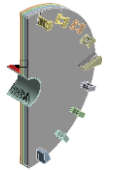
	Original model (original mesh)	Original model (new mesh)	Simplified 2 model (original/ new mesh)	Simplified 3 model (original/ new mesh)	Submodel (original/ new mesh)
Total deformation max. value	2.6233	2.6696	2.5303 / 2.4444	2.6043 / 2.5668	2.623 / 2.6709
Relative error	0.000%	1.765%	3.545% / 8.436%	0.724% / 3.851%	0.011% / 0.049%
Equivalent stress max. value	239	248	337 / 331	235 / 242	244 / 253
Relative error	0.000%	3.766%	41.004% / 33.468%	1.674% / 2.419%	2.092% / 2.016%
Time to Solve	40m 26s	22m 58s	19m 47s / 3m 17s	25m 15s / 4m 18s	5m 11s / 54s
Comments	Reference	The new mesh shows accurate results	E > 5%	The original mesh shows more accurate results	Both meshes show accurate results, but the new mesh is solved faster

Table 7.2: Comparison of the different models with the first hinged version (HV1) of the intermediate wedges
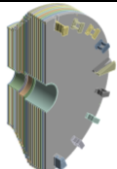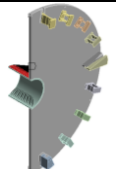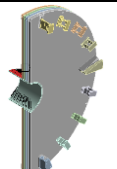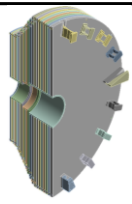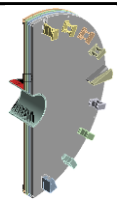
	Original hinged model	Simplified 2 hinged model	Simplified 3 hinged model	Hinged submodel
Total deformation max. value	3.2467	3.2195	3.1028	2.951
Relative error	0.000%	0.838%	4.432%	9.108%
Equivalent stress max. Value	605	577	546	484
Relative error	0.000%	4.628%	9.752%	20.000%
Equivalent stress probe value	137.89	69.591	135.13	158.83
Relative error	0.000%	49.532%	2.002%	15.186%
Time to Solve	2h 1m 25s	4m 16s	5m 30s	1m 10s
Comments	Reference. Only running with Workbench 2019	E > 5%	E > 5%	E > 5%

ETSEIB

CMS

Table 7.3: Comparison of the different models

	Original hinged model	Simplified 2 hinged model	Simplified 3 hinged model	Hinged submodel
Model validation	Passed	Failed	Passed	Failed
Results consistency	Passed	Failed	Passed	Failed
Time to Solve	2h 1m 25s	4m 16s	5m 30s	1m 10s
Comments	Only running with Workbench 2019	E > 5%	E eq. stress max. value > 5% E probe stress < 5% E average stress < 5%	Hypothesis not verified
Verdict	Model not suitable for an optimisation process	Not valid model	Just one result is not consistent. Final model	Not valid model

Firstly, Table 7.1 compares the different models with the original fixed version (V0) of the intermediate wedges. The reference model is the "Original model (original mesh)". Compared to this, the "Original model (new mesh)", "Simplified 3 model (original/new mesh) and "Submodel (original/new mesh)" show accurate results because their relative errors are under 5% and can be considered as **valid** models.

Secondly, Table 7.2 compares the different models with the original hinged version (HV1) of the intermediate wedges. The reference model is the "Original hinged model (new mesh)". Compared to this, "Simplified 2 hinged model", "Simplified 3 hinged model" and "Hinged submodel" do not show accurate results because their relative errors are above 5%. Nevertheless, if we compare average instead of maximum stresses, "Simplified 3 hinged model" shows **consistent** results.

Finally, Table 7.3 summarises the important hints of every model. **Simplified 3 hinged model** is the only model that can be validated and shows consistent results. Compared to the original model, the time to solve is decreased 24 times.

Model Limits

As a limit of the model, we have considered the HGCal endcap represented by the CE-H absorbers' structure without the back flange, tie rods, bolts, pins and cassettes (that will be represented as distributed mass elements). This means that inner cylinder 3, absorbers 19-22, spacers 19-22 and wedges will be the only parts incorporated into the model. CE-E and the suppressed parts will be simplified as a remote force defined in Table 7.4 by a rigid remote point and two components (gravity and magnetic).

Table 7.4: Remote force definition

		Mass (t)	Centroid X (mm)	Centroid Y (mm)	Centroid Z (mm)	Gravity force (N)	Magnetic force (N)
CE-E	Total	10.198	0	1817.5	-735	-100000	56088.11
CE-H	Cassettes 1-19	8.790				-86194.7	48345
	Absorbers 1-18	54.811	4.49E-02	854.03	-1026.5	162626	82283
	Cassettes 20-22	1.819				-17837.1	10004.5
	Abs. 19-22 + wedges	25.166	-12.209	169.98	-1145.6	-246778	138413
	Total	90.586	-3.81098	638.7831	-1063.98	-888286	498223

TOTAL		100.784	-3.42536	758.0519	-1030.69	-988286	439873.5

Remote Point		73.799	0.037861	1005.168	-980.773	-723671	301460.5

Boundary Conditions

The boundary conditions specified in Table 7.5 and Table 7.6 define how the intermediate wedges behave in relation to its environment.

Table 7.5: Geometries relationships and ANSYS definition. The highlighted connections are the ones related to the spherical joints

Table 7.6: ANSYS definition of the type, value, and processing time of the forces in the system

Steps	CE-E	CE-H Tie rods	Bolts	Pins	Spacers	Inner cylinders	Absorbers /Cassettes	Wedges
1) Lock								
2) + Gravity acceleration					*Y: -9.806 m/s²*			
3) + Gravity remote force	*Y: -724 kN*							
4) + Magnetic acceleration					*Z: 5.5 m/s²*			
5) + Magnetic remote force		*Z: 301 kN*						
6) + Thermal condition					*-35 °C*			

New forces

The definition of the forces acting on the system is divided into six steps, of which two are new. For simplifying the model, the CE-E and suppressed parts of CE-H are represented by a force applied to the centre of gravity of the part (Eq. 7.3-5):

$$X = \frac{\sum_i m_i x_i}{\sum_i m_i} = \frac{10.198 * 0 + 54.811 * 4.49E - 02}{10.198 + 54.811} = 0.03 \simeq \mathbf{0} \qquad \text{(Eq. 7.3)}$$

$$Y = \frac{\sum_i m_i y_i}{\sum_i m_i} = \frac{10.198 * 1817.5 + 54.811 * 854.03}{10.198 + 54.811} = \mathbf{1005.17} \qquad \text{(Eq. 7.4)}$$

$$Z = \frac{\sum_i m_i z_i}{\sum_i m_i} = \frac{10.198 * (-735) + 54.811 * (-1026.5)}{10.198 + 54.811} = -\mathbf{980.77} \qquad \text{(Eq. 7.5)}$$

3) **Gravity remote force.** Represents the weight of the CE-E, tie rods, bolts, pins, spacers 1-18, inner cylinders 1 & 2, cassettes 1-19 and absorbers 1-18. As calculated in Table 7.4, all together means a total of 74 t or 724 kN.

5) **Magnetic remote force.** Is calculated in Table 7.4 thanks to the magnetic acceleration and the sum of all the metallic geometries' masses (tie rods, bolts, pins, spacers 1-18, inner cylinders 1 & 2 and absorbers 1-18). In total it is 301 kN.

New connections

Five types of connections are described and two of them are new:

- **No separation.** This contact setting is like the Bonded. Separation of the geometries in contact is not allowed, but the parts can slide. [17]
- **Rough.** This contact setting is similar to the Frictional and no sliding is possible when the contact is closed. [17]

Idealisations

As in the Original model, the hinged one has been simplified by imposing the **symmetry condition**, and **reducing** the number of **geometries** and **boundary conditions**. In this case, not only the ETL, PM and CE-E have been represented by a remote force, but also the tie rods, bolts, pins, spacers 1-18, inner cylinders 1 & 2, cassettes 1-19 and absorbers 1-18.

In addition, the state of the stresses and deformations will remain as in the original model.

7.1.3.2. Lug Sizing

As shown in Figure 7.6, in the hinged version of the intermediate wedges the stress is mostly concentrated around the pin. For this reason, the first step to optimise the shape of the wedges consisted of sizing the lug.
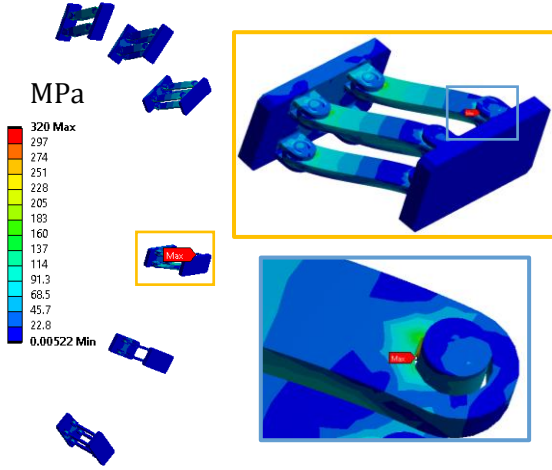
Figure 7.6: Equivalent stress distribution and maximum equivalent stress value of the intermediate hinged wedges [ANSYS]
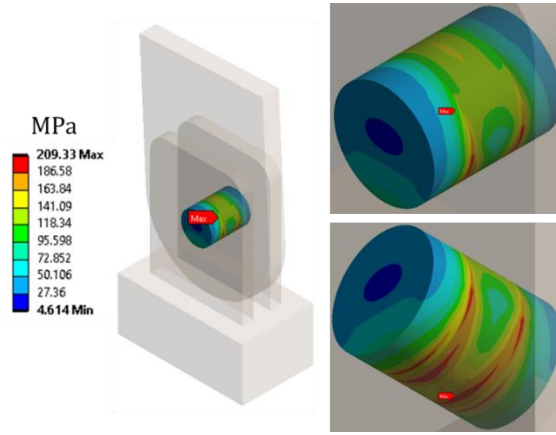
Figure 7.7: Equivalent stress distribution and maximum equivalent stress value of the pin in the lug analysis [ANSYS]

Firstly, the force applied to the joint has to be estimated. Secondly, a method to predict the stresses and lower them below $207\ MPa$ (the yield strength of stainless steel) has to be found.

On the one hand, the simplified analysis allowed sizing the lug (Eq. 7.6-11) but it can not predict the analytical maximum equivalent stress (Figure 7.7).
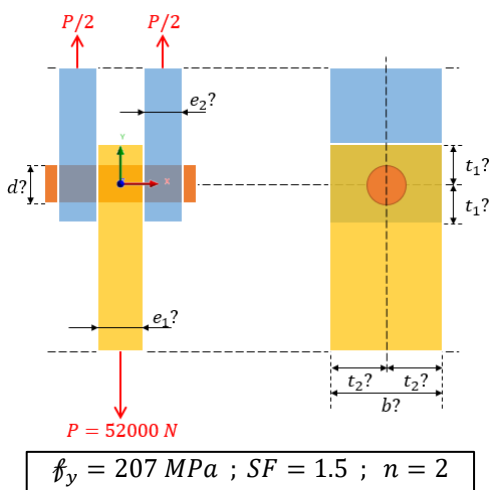
Figure 7.8: Lug dimensions and boundary conditions

- σ_{all}?
  $$\sigma_{all} = \frac{f_y}{SF} = \frac{207}{1.5} = 138\ MPa \qquad (Eq.\ 7.6)$$

- d?
  $$\tau_{xy,\,shear} = \frac{T_y}{n \cdot \frac{\pi}{4} d^2} \leq \tau_{all} = 0.65 \cdot \sigma_{all} \Rightarrow$$
  $$d_{min} = \sqrt{\frac{T_y}{n \cdot \frac{\pi}{4} \cdot \tau_{xy,\,shear}}} = \sqrt{\frac{52000}{2 \cdot \frac{\pi}{4} \cdot 0.65 \cdot 138}} = 19\ mm \qquad (Eq.\ 7.7)$$

- e_1? e_2?
  $$\sigma_{y,\,bearing} = \frac{N}{d \cdot e_1} \leq \sigma'_{all} = 2 \cdot \sigma_{all} \Rightarrow$$
  $$e_{1,\,min} = \frac{N}{d \cdot \sigma'_{all}} = \frac{52000}{19 \cdot 2 \cdot 138} = 10\ mm \qquad (Eq.\ 7.8)$$
  $$e_{2,\,min} = 0.7 \cdot e_{1,\,min} = 7\ mm \qquad (Eq.\ 7.9)$$

- t_1? t_2? b?
  $$t_1 \geq 2 \cdot d_{min} = 38\ mm \qquad (Eq.\ 7.10)$$
  $$t_2 \geq 1.5 \cdot d_{min} = 28.5\ mm \Rightarrow b = 57\ mm \qquad (Eq.\ 7.11)$$

On the other hand, the pin was modelled as a beam (Figure 7.9 and Figure 7.10) and the critical stresses were located and estimated (Figure 7.11). In this case, the calculated maximum equivalent stress was approximately the one obtained in the analysis (Figure 7.7).

<div style="display:flex">

Cantilever Beam – Uniformly Increasing Load
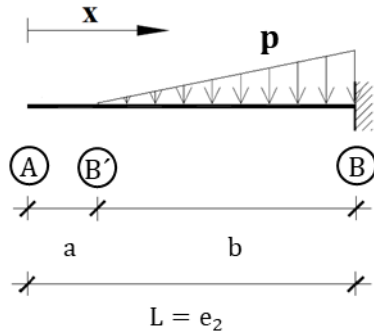
$$R_B = \frac{p \cdot b}{2}$$ *(Eq. 7.12)*
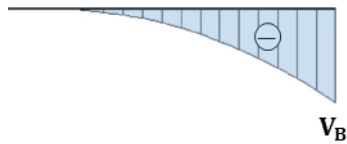
$$V_{B'B} = -\frac{p \cdot (x - a)^2}{2b}$$ *(Eq. 7.14)*

$$V_B = \frac{p \cdot b}{2}$$ *(Eq. 7.16)*
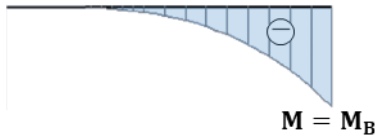
$$M_{B'B} = -\frac{p \cdot (x - a)^3}{6b}$$ *(Eq. 7.18)*

$$M = M_B = \frac{p \cdot b^2}{6}$$ *(Eq. 7.20)*

</div>

<div style="display:flex">

Simple Beam – Uniformly Distributed Load and End Moments
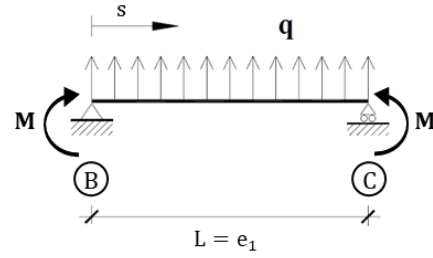
$$R_B = R_C = \frac{q \cdot L}{2}$$ *(Eq. 7.13)*
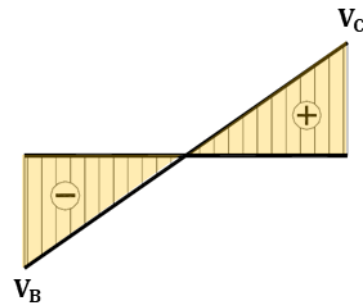
$$V_{BC} = -q \cdot \left(\frac{L}{2} - s\right)$$ *(Eq. 7.15)*

$$V_B = -V_C = \frac{q \cdot L}{2}$$ *(Eq. 7.17)*
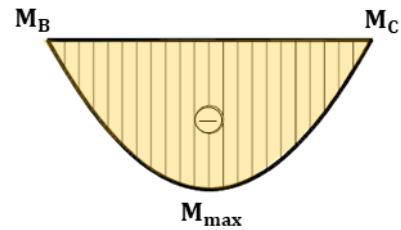
$$M_{BC} = M - \frac{q \cdot s}{2}(L - s)$$ *(Eq. 7.19)*

$$M_B = M_C = M$$ *(Eq. 7.21)*

$$M_{max} = M - \frac{q \cdot L^2}{8} \qquad para\ s = \frac{L}{2}$$ *(Eq. 7.22)*

</div>

Figure 7.9: Beam model of the pin. Formulas *[21]* and input data. The bonded part of the pin (blue) can be modelled as a cantilever beam – uniformly increasing load. The frictionless part (yellow) can be modelled as a simple beam – uniformly distributed load and end moments

$$d = 19\ mm, e_1 = 10\ mm, e_2 = 7\ mm, a = 2\ mm, b = 5\ mm, q = 4837\ \frac{N}{mm}, p = 9868\ \frac{N}{mm}$$

x [mm]	Analytical data			Theoretical data	
	N_x [N]	T_y [N]	M_z [N·mm]	T_y [N]	M_z [N·mm]
0	-60	-547	490	0	0
1	-349	-2882	1323	0	0
2	-856	-6322	1056	0	0
3	-1067	-7592	-1163	-987	-329
4	-1756	-11420	-9835	-3947	-2632
5	-2635	-15800	-17504	-8882	-8882
6	-3358	-19290	-28634	-15789	-21053
7	-5280	-25081	-40110	-24671	-41118
8	-5650	-19705	-60429	-19466	-63018
9	-5650	-17547	-78840	-14600	-80050
10	-5650	-11398	-91477	-9733	-92217
11	-5650	-5274	-99140	-4867	-99516
12	-5650	-1024	-101860	0	-101950
13	-5650	5194	-99159	4867	-99516
14	-5650	11373	-91469	9733	-92217
15	-5650	13461	-78843	14600	-80050
16	-5650	19702	-60435	19466	-63018
17	-5280	25076	-40122	24333	-41118
18	-3655	21228	-30495	15789	-21053
19	-2630	15800	-17563	8882	-8882
20	-1751	11413	-9880	3947	-2632
21	-1499	10060	-4437	987	-329
22	-855	6328	1051	0	0
23	-349	2883	1320	0	0
24	-60	547	489	0	0
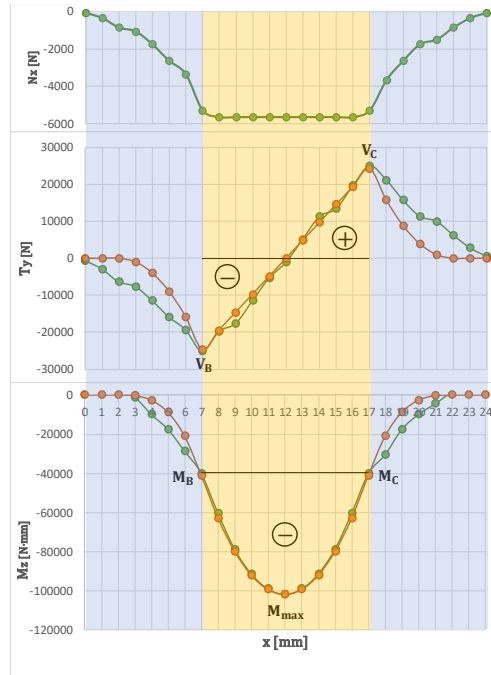
Figure 7.10: Comparison between analytical and theoretical output data, assuming to have simple bending of a beam ($T_y + M_z$). The x component of the force (N_x) is going to be ignored in this analysis because it is originated due to the change of boundary conditions (Bonded – Frictionless – Bonded) and, consequently, it is unpredictable

$$\sigma_{x,\ bending} = -\frac{M_z}{I_z} \cdot y = -M_z \cdot \frac{d/2}{\pi d^4/64} = -\frac{32}{\pi}\frac{M_z}{d^3} \qquad (Eq.\ 7.23)$$

$$\tau_{xy,\ shear} = \frac{4}{3} \cdot \frac{T_y}{\pi/4\ d^2} \qquad (Eq.\ 7.25)$$

$$\sigma_{eq} = \sqrt{\sigma_x^2 + 3 \cdot \tau_{xy}^2} \qquad (Eq.\ 7.24)$$

$x = x_B, x_C = 7\ mm, 17\ mm,\ M_z = M = -41118\ N\cdot mm,\ T_y = R_b = -24671\ N$
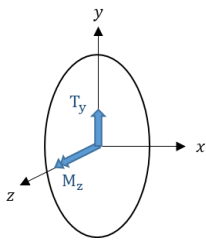
$$\sigma_{x,\ bending}\left[\frac{N}{mm^2}\right] = 61$$

$$\tau_{xy,\ shear}\left[\frac{N}{mm^2}\right] = -116$$

$$\sigma_{eq}\left[\frac{N}{mm^2}\right] = 210$$

$x = x_{s/2} = 12\ mm,\ M_z = M_{max} = -101950\ N\cdot mm,\ T_y = 0\ N$
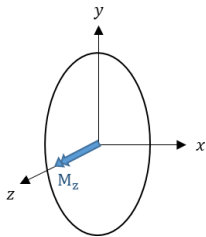
$$\sigma_{x,\ bending}\left[\frac{N}{mm^2}\right] = 151$$

$$\tau_{xy,\ shear}\left[\frac{N}{mm^2}\right] = 0$$

$$\sigma_{eq}\left[\frac{N}{mm^2}\right] = 151$$

Figure 7.11: Study of the critical sections, and bending, shear and equivalent stresses

ETSEIB   CMS

By defining the method, the dimensions of the lug (diameter of the pin and thicknesses) were changed and several attempts were made to predict the stresses (Table 7.7). Comparing theoretical (orange) and analytical (green) data, two important issues can be observed. Firstly, the analytical shear stress for $x = x_B, x_C$ is constant regardless of the diameter. Secondly, the analytical bending stress for $x = x_{1/2}$ was much higher than the predicted value. Both incongruities are due to the contact connection and unpredictable.

In conclusion, as it was impossible to lower the shear stress below 110 MPa, the maximum equivalent stress could not be lowered below 191 MPa. Therefore, a safety factor of 1.5 could not be achieved and the hinged model had to move from cylindrical to spherical joints. On the one hand, spherical hinged wedges only take traction forces. This will simplify the study. On the other hand, the value of the force is reduced. Consequently, the shear and maximum equivalent stresses will lower, and it will be feasible to build the hinged version of the intermediate wedges with stainless steel.

Based on mechanisms to be found on the market, only two options were consistent: axial joints or rod ends. However, due to the tensile and compressive force values that joints have to withstand, only rod ends can be used. Between female or male threads, the last ones were chosen because of the reduced distance between the centres of the drilled holes in the bases and the adaptability of the male thread, that can be easily cut. In the next chapter, their final design will be discussed.
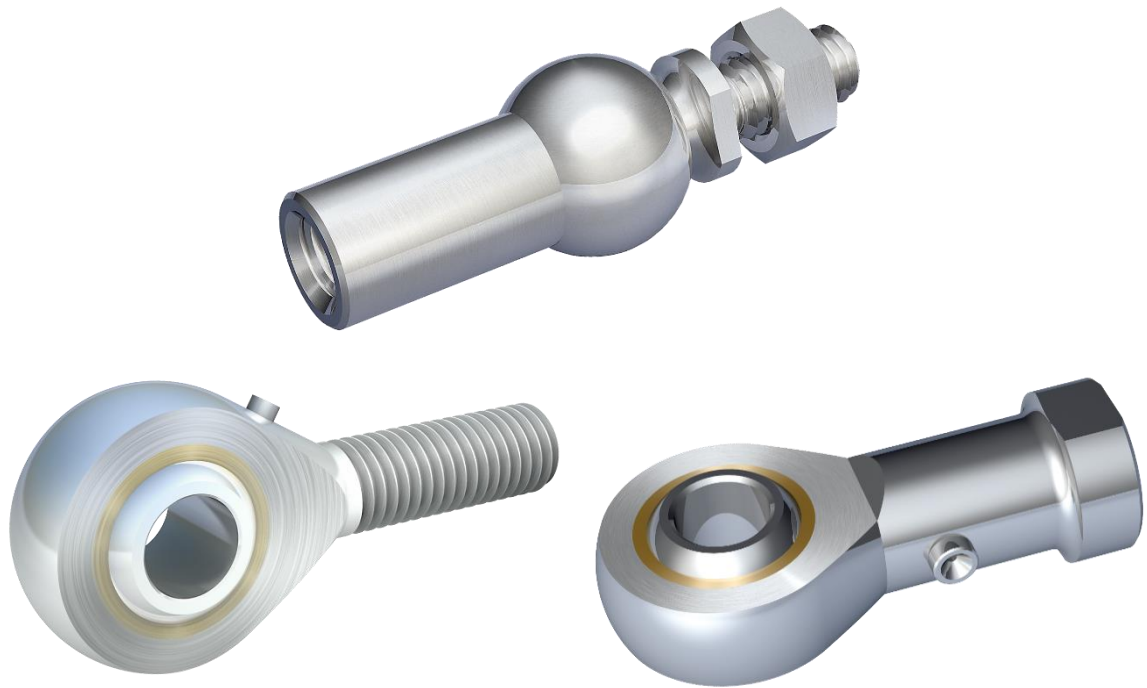
Figure 7.12: Spherical joints. (Up) Axial Joint. (Down, left) Rod end male thread. (Down, right) Rod end female thread [mbo]

Table 7.7: Pin optimisation

Version	Dimensions					Boundary conditions				Stresses results									SF
										$x = x_B, x_c$, $M_z = M$, $T_y = R_b = \frac{pb}{2}$				$x = x_{s/2}$, $M_z = M_{max}$, $T_y = 0$				
	$d\,[mm]$	$e_1\,[mm]$	$e_2\,[mm]$	$a\,[mm]$	$b\,[mm]$	$p\,\frac{N}{mm}$	$M[N\cdot m]$	$\frac{M_{max}}{[N\cdot m]}$	$q\,\frac{N}{mm}$	$\sigma_{x,\,bending}^{+}\,\frac{N}{mm^2}$	$\sigma_{x,\,bending}^{-}\,\frac{N}{mm^2}$	$\tau_{xy,\,shear}\,\frac{N}{mm^2}$	$\sigma_{eq}\,\frac{N}{mm^2}$	$\sigma_{x,\,bending}^{+}\,\frac{N}{mm^2}$	$\sigma_{x,\,bending}^{-}\,\frac{N}{mm^2}$	$\tau_{xy,\,shear}\,\frac{N}{mm^2}$	$\sigma_{eq}\,\frac{N}{mm^2}$	
2.3	19	10	7	2	5	-10400	-43333	-108333	5200	64 / 74	-64 / -45	-122 / -116	221 / 205	161 / 156	-161 / -198	0 / -8	161 / 203	0.94 / 1.01
2.4	22	9	6	2	4	-13000	-34667	-93167	5778	33 / 36	-33 / -48	-91 / -113	161 / 205	89 / 71	-89 / -171	0 / -3	89 / 207	1.28 / 1.00
2.5	25	8	6	2	4	-13000	-34667	-86667	6500	23 / 43	-23 / -44	-71 / -112	124 / 206	56 / 95	-56 / -154	0 / -2	56 / 208	1.66 / 1.00
2.6	24	10	7	2	5	-10400	-43333	-108333	5200	32 / 32	-32 / -37	-77 / -114	137 / 204	80 / 66	-80 / -197	0 / -2	80 / 182	1.52 / 1.01
2.7	24	12	7	2	5	-10400	-43333	-121333	4333	32 / 35	-32 / -37	-77 / -111	137 / 197	89 / 76	-89 / -168	0 / -3	89 / 138	1.52 / 1.05

7.2.   Final Results' Analysis

For the final results' analysis two changes have been made. Firstly, the materials have been specified and some of their properties re-defined (Table 7.8). Secondly, the 12 o'clock wedge has moved from sliding to fixed because the assembly cost and complexity is reduced, and the safety coefficient is above 2. This fact will not be discussed in the thesis because it does not belong to the study of the intermediate wedges.

Table 7.8: General, thermal, and mechanical properties of stainless steel 1.4306, 1.4034 and 1.4057, and titanium alloy grade 4 at 20 °C [1]

Geometries		Stainless steel 1.4306	Stainless steel 1.4034	Stainless steel 1.4057	Titanium alloy grade 4
		Arms, base plates and pins	Rod end - ball	Rod end- stem	Fixed intermediate wedges
Density	kg/m^3	7900	7700	7700	4510
Thermal conductivity	$W/m \cdot °C$	15	30	25	17.2
Thermal expansion coefficient	$10^{-6}/°C$	16	10.5	10.5	8.6
Young's modulus	GPa	200	215	215	105
Tensile yield strength	MPa	$R_{p0.2} = 200$ $R_{p1} = 240$	$R_{p0.2} = 400$ $R_{p1} = 480$	600	572
Tensile ultimate strength	MPa	500-700	640	800	727

7.2.1.   Operational Position

7.2.1.1.   *Displacement Field. Evaluation of Maximum Displacement Under Nominal Load*

On one side, Figure 7.13 shows wedges' total deformation distribution. On the other, Figure 7.14 represents the directional deformation distributions.

As already presented in section 6.1.1, the total deformation is mainly created because of a thermal condition. In addition to that, an asymmetry in the results is observed. The maximum offset is 2.8343 mm, which represents 0.94% of the total width of the intermediate wedges. This displacement is translated into an elastic permanent deformation for the fixed version, and movement for the hinged one.
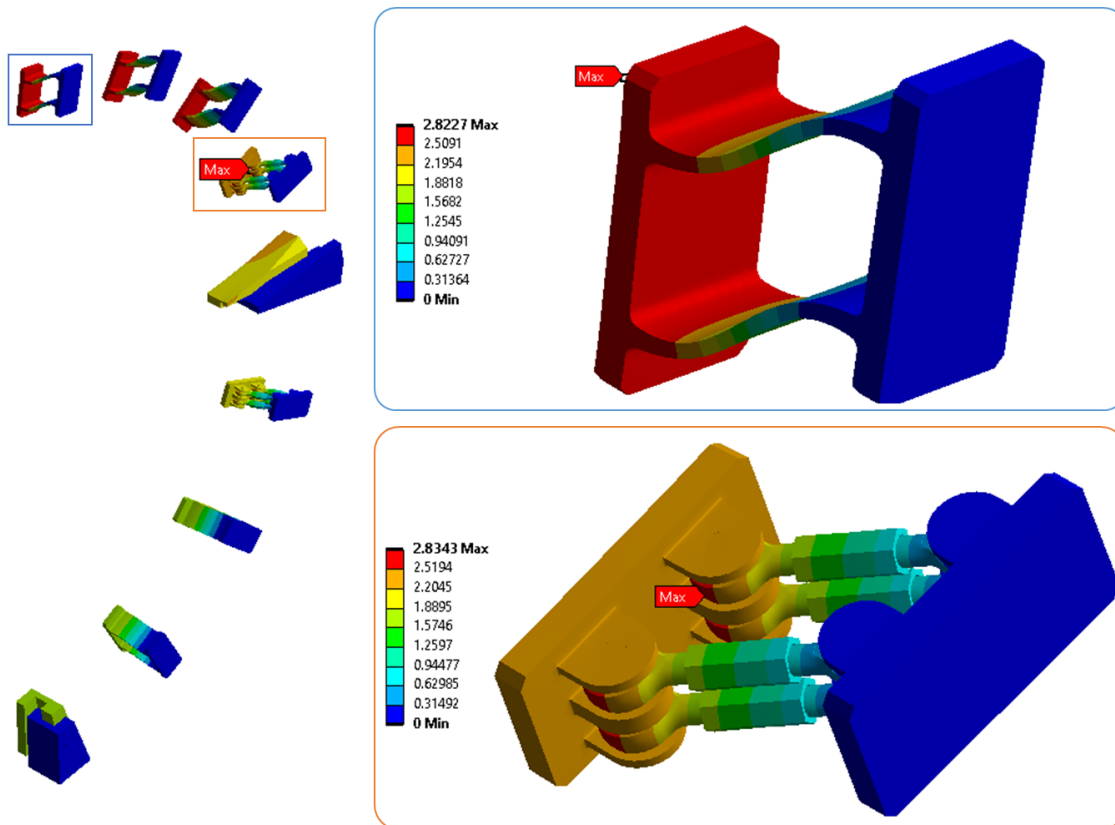
Figure 7.13: Total deformation [*mm*] distribution of the wedges [ANSYS]
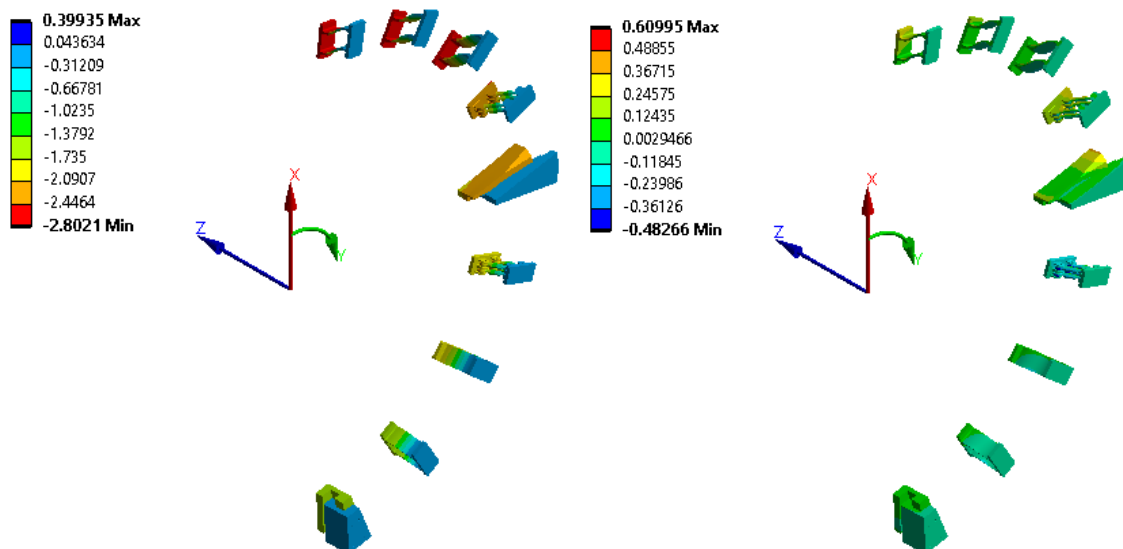
Figure 7.14: Directional deformation [*mm*] of the wedges. (Right) Thermal condition – X Axis or Radial component, negative is towards the centre. (Left) Magnetic condition – Z Axis or Axial direction, positive is towards the interaction point [ANSYS]

Fixed version

As in section 6.1.2, a **symmetrical distribution** of the stresses can be observed. On the one hand, the areas under pure traction or compression are concentrated in the depth, specifically in the rounded edges and surroundings (Figure 7.15 and Figure 7.16). On the other hand, at the bases most elements are under traction and compression at the same time. Finally, in Figure 7.17 a distortion and a 3D phenomenon can be detected again.
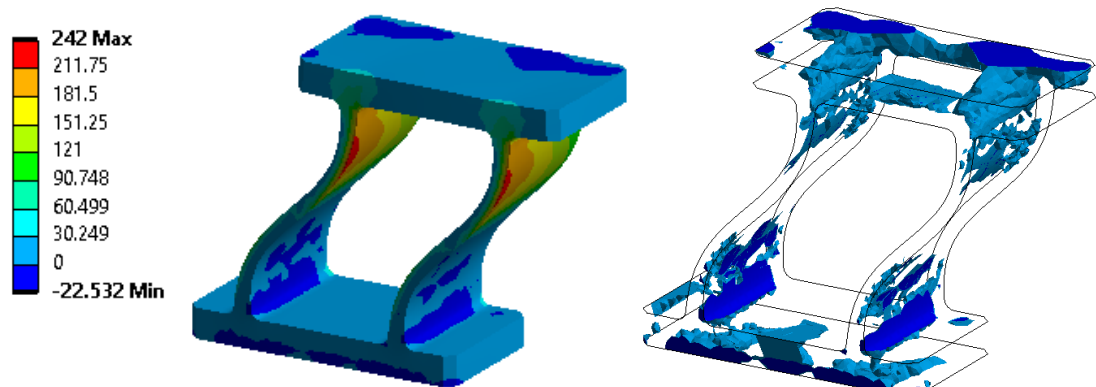
Figure 7.15: (Left) Maximum Principal Stress $[MPa]$ distribution of the fixed version, and (Right) Areas under compression ($\sigma_I \leq 0$) [ANSYS]
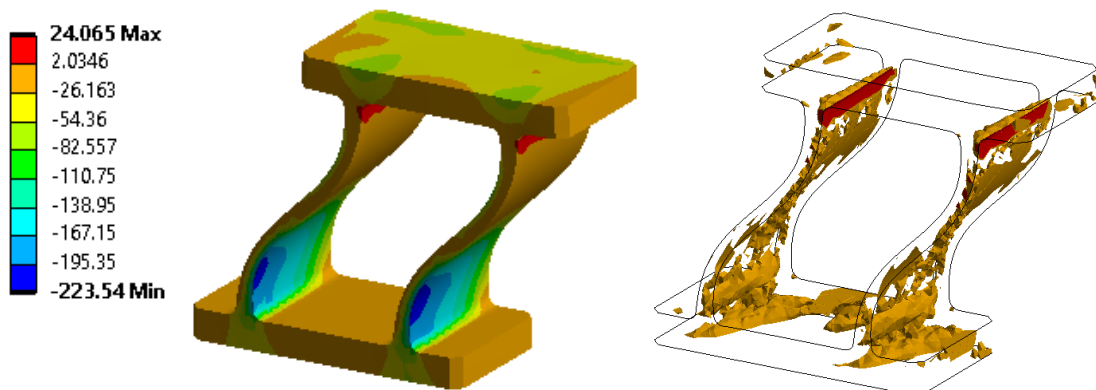
Figure 7.16: (Left) Minimum Principal Stress $[MPa]$ distribution of the fixed version, and (Right) Areas under traction ($\sigma_{III} \geq 0$) [ANSYS]
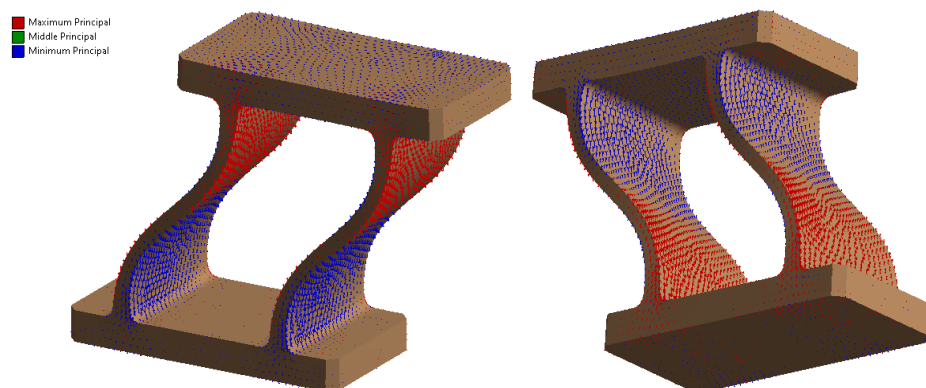
Figure 7.17: Vector Principal Stress of the fixed version [ANSYS]

Hinged version

On the one hand, in Figure 7.18 it can be observed that areas under pure compression are mainly concentrated around pins. On the other hand, in Figure 7.19 it is shown that areas under pure traction are situated around pins, arms and bases. In this case, **symmetrical** – pins – and **asymmetrical** – arms and bases – distributions of the stresses are found. This is occurring because the intermediate hinged version of the wedges is principally subjected to tensile forces. However, as pins are simultaneously connected to rod ends and lugs, they suffer traction and compression at the same time. Finally, in Figure 7.20 and same as above, a distortion and a 3D phenomenon are detected.
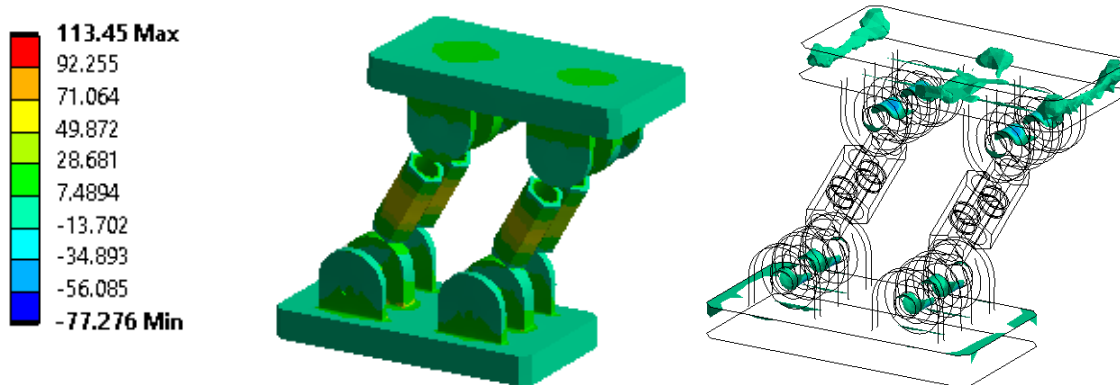
Figure 7.18: (Left) Maximum Principal Stress [MPa] distribution of the hinged version, and (Right) Areas under compression ($\sigma_I \leq 0$) [ANSYS]
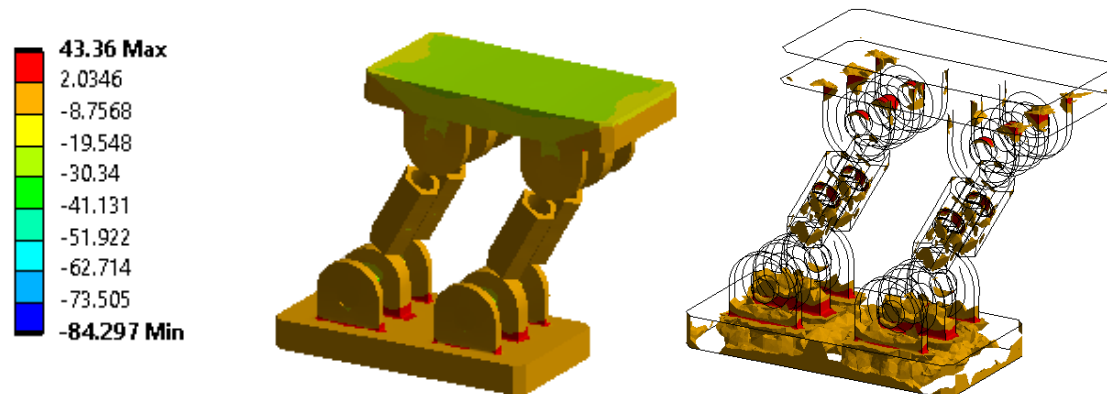
Figure 7.19: (Left) Minimum Principal Stress [MPa] distribution of the hinged version, and (Right) Areas under traction ($\sigma_{III} \geq 0$) [ANSYS]
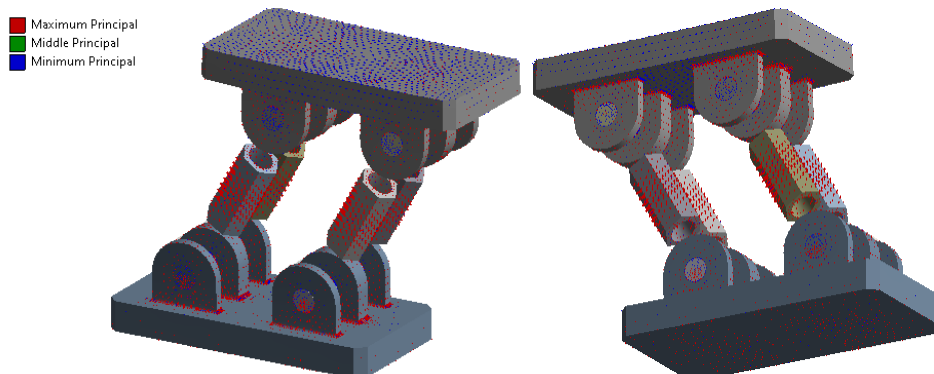
Figure 7.20: Vector Principal Stress of the hinged version [ANSYS]

7.2.1.3.   Equivalent Stress Distribution

As already justified in section 6.1.3, it was decided to use the **Von Mises** criterion to evaluate the maximum stresses of the pieces.

As shown in Figure 7.21, the areas of the **fixed wedges** where the maximum stress is concentrated have moved to the **arms,** since one of the objectives of the fixed version optimisation was spreading the stress.

Alike, in Figure 7.22, the areas of the **hinged wedges** where the maximum stress is concentrated are the **central sections of the arms**.
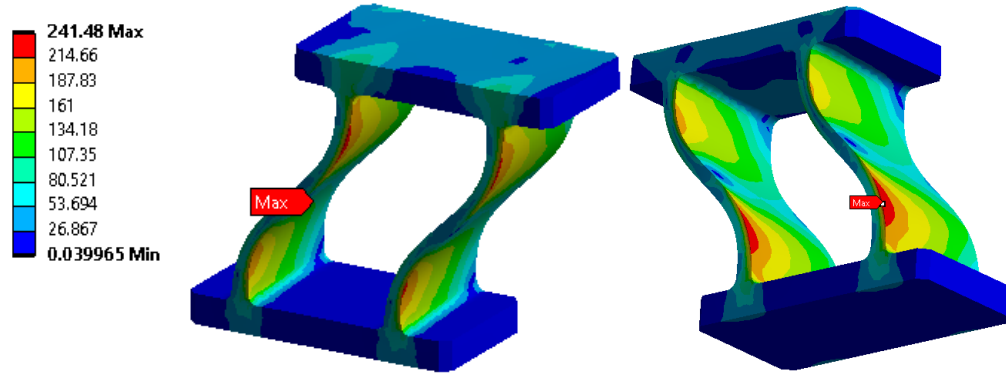
Figure 7.21: Equivalent Stress [MPa] distribution of the fixed version (Von Mises criteria) [ANSYS]
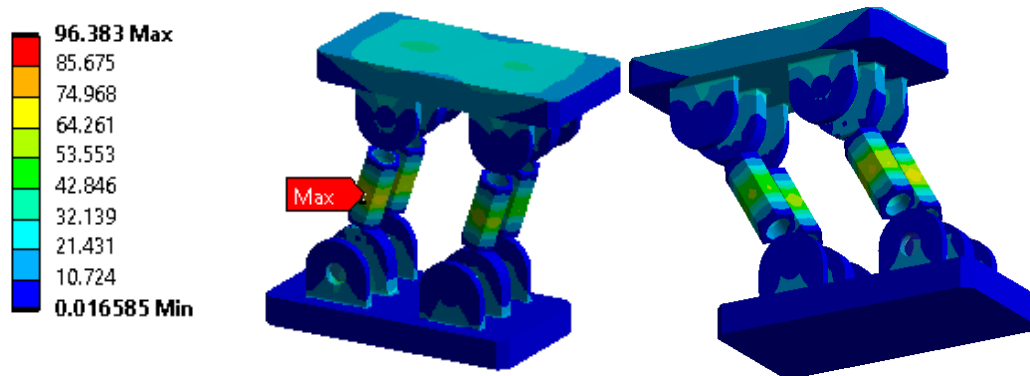
Figure 7.22: Equivalent Stress [MPa] distribution of the hinged version (Von Mises criteria) [ANSYS]

7.2.1.4.   Failure Criteria

For the **fixed wedges**, the maximum equivalent stress of the final design is 241.5 MPa, a value below the tensile yield strength limit of titanium alloy grade 4 (572 MPa). Then, the safety factor is above the established limits (Eq. 7.26).

$$\gamma_s = \frac{572}{241.5} = \mathbf{2.4}$$

(Eq. 7.26)

For the **hinged wedges**, the maximum equivalent stress of the final design is 96.4 MPa, a value below the tensile yield strength limit of stainless steel 1.4306 (200 MPa). Then, the safety factor is above the established limits (Eq. 7.27).

$$\gamma_s = \frac{200}{96.4.5} = \mathbf{2.1}$$

(Eq. 7.27)

7.2.1.5.   Force Reaction

In the next section, the loads in x, y and z are calculated for all the wedges based on the applied conditions (Figure 7.23).

On the one hand, we verify that the theoretical values of the gravity and magnetic forces correspond to those obtained by the analysis with a relative error of less than 2.3%.

$$F_g = \sum_i y_{g,i} = 988583 \Rightarrow E = \frac{|988286 - 988583|}{988286} = 0.03\% \qquad \textit{(Eq. 7.28)}$$

$$F_m = \sum_i y_{g,i} - y_{m,i} = 450048 \Rightarrow E = \frac{|439874 - 450048|}{439874} = 2.31\% \qquad \textit{(Eq. 7.29)}$$

On the other hand, we observe that as we had predicted in section 4.3.2 and proved in section 6.1.5, due to the existence of the intermediate wedges, the total load supported by the main wedges would lighten. In the preliminary design, 3 & 9 o'clock wedges supported the 64.5% of the total weight (Eq. 6.2). In the final design, they withstand the 76.6% (Eq. 7.30).

$$\begin{matrix} \textbf{\textit{Total weight}} \\ \textbf{\textit{percentage}} \end{matrix} = \frac{756590}{988286} \cdot 100 = 76.6\% \qquad \textit{(Eq. 7.30)}$$

Finally, it can be checked that the intermediate hinged wedges only take tensile loads due to the spherical joints.

x [N]	y [N]	z [N]
7655	5325.1	-109750
-1150.9	3427.3	-193580
-6008.5	20740	-212680

x [N]	y [N]	z [N]
47549	31650	-40708
47885	31648	-79392
37741	46538	-81682

x [N]	y [N]	z [N]
55601	70747	-17620
58002	73567	-57160
42595	83315	-56468

x [N]	y [N]	z [N]
-1.9916	177.56	-93135
-2.2345	176.81	-112270
-20.658	184.04	-107450

x [N]	y [N]	z [N]
0	760430	-2014.5
0	758220	-88028
0	756590	-57358

x [N]	y [N]	z [N]
-0.63751	184.44	91288
-0.48134	183.31	66251
-17.402	177.36	71066

x [N]	y [N]	z [N]
-56958	72468	19157
-55089	70235	-18324
-69605	59238	-19332

x [N]	y [N]	z [N]
-50495	33537	26497
-49865	33281	-10801
-57246	16598	-3124

x [N]	y [N]	z [N]
-62276	14064	126290
-80063	17845	43261
-20553	5195.9	16980

Gravity
+ Magnetic force
+ Thermal condition

Figure 7.23: Forces reactions for all wedges based on the applied conditions (gravity, gravity + magnetic force, gravity + magnetic force + thermal condition)

7.2.1.6. Thermal Analysis

The temperature distributions represented in Figure 7.24 and Figure 7.25 show that the temperature of the intermediate wedges varies from $-35\ °C$ to $13.7\ °C$ (fixed version) and to $18.6\ °C$ (hinged version). This means that the hinged version transfers more heat (64 W) than the fixed one (44.6 W) in case there is perfect contact between all the geometries. In total, all the intermediate wedges will dissipate 613 W (Eq. 7.31).

$$\boldsymbol{Total\ energy\ dissipated} = 2 \cdot (64 \cdot 2 + 44.6 \cdot 4) = \boldsymbol{613\ W} \qquad \textit{(Eq. 7.31)}$$
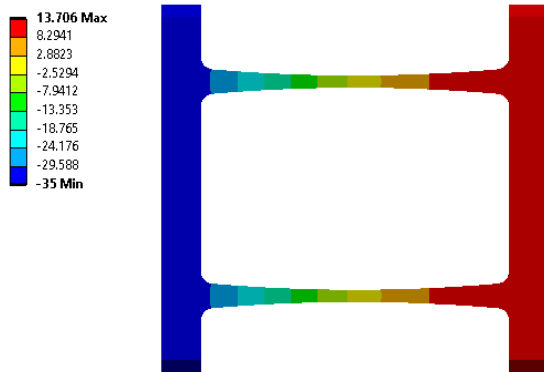
Figure 7.24: Temperature [$°C$] distribution of the fixed version [ANSYS]
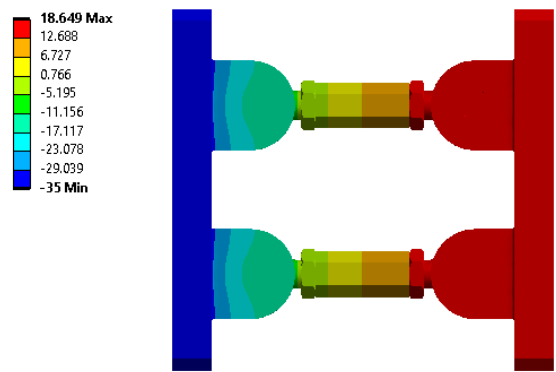
Figure 7.25: Temperature [$°C$] distribution of the hinged version [ANSYS]

7.2.2. Assembly Position

7.2.2.1. Buckling Analysis

For the final configuration, the load multiplier of the fixed version is 5.3169 and the buckling force is 1.391e+006 N (Eq. 7.32) or 140 t. The intermediate hinged wedges will never buckle but move before. This will most likely never happen but, given this situation, the total deformation of the intermediate wedges will be the one shown in Figure 7.26.

$$\boldsymbol{Buckling\ force} = 5.3169 \cdot 2.616e + 005\ N = \boldsymbol{1.391e + 006\ N} \qquad \textit{(Eq. 7.32)}$$
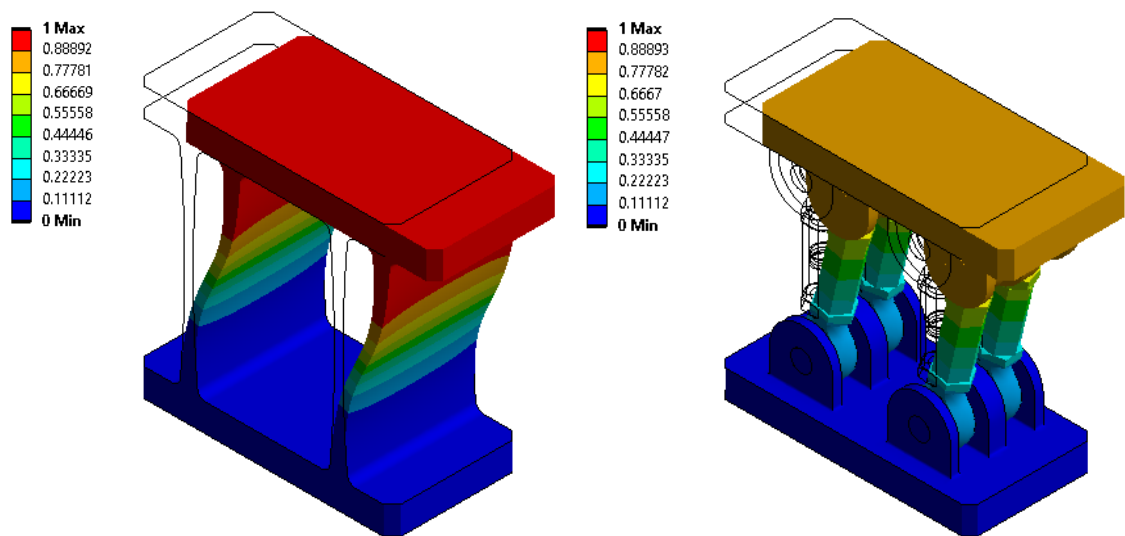
Figure 7.26: Buckling total deformation of the final designs [ANSYS]

8. Final Design and Building Process

8.1. Final Design

The final configuration of the intermediate wedges consists of two designs. The hinged version, situated near 3 & 9 o'clock wedges, and the fixed one in all other positions.

The tolerances defined in the drawings are meant to ensure that all the geometries will fit and parallelism between the bases is maintained [22] [23].

8.1.1. Fixed Version

The final design of the fixed version is an optimised three-dimensional model of the preliminary design (Figure 8.1 and Figure 8.2). The original volume of the piece ($300 \, mm \times 316.5 \, mm \times 150 \, mm$) and the dimensions of the bases ($42.5 \, mm$ and $32.5 \, mm$) were preserved. Therefore, just the shape, thickness and fillet radius of the arms have been modified.

In Annex D.1 the drawings of the piece with and without the drill holes can be found. Comparing Figure 4.19 and Figure 8.1, the distribution of the orifices changes to make it the same as the one of the hinged version.
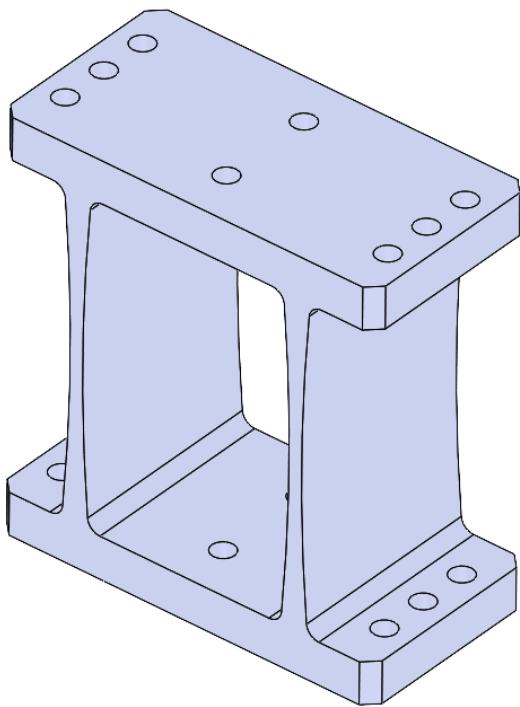
Figure 8.1: Final design of the fixed version of the intermediate wedges (with bolts)
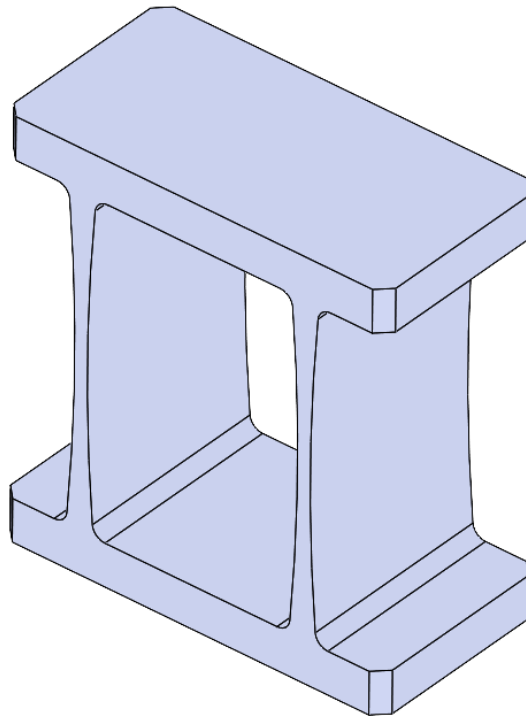
Figure 8.2: Final design of the fixed version of the intermediate wedges (without bolts)

8.1.2. Hinged Version

The final design of the hinged version is a three-dimensional model based on the assembly of four geometries: the base plates, the arms, the pins and the rod ends. The last ones will be purchased and determine several dimensions of the rest. The original volume of the piece ($300\ mm \times 316.5\ mm \times 150\ mm$) and the dimensions of the bases ($42.5\ mm$ and $32.5\ mm$) will also be preserved as in the fixed version.

8.1.2.1. Lug Sizing

The lug sizing consisted of finding a rod end inner diameter (d) and thickness (e_1) in which the maximum equivalent stress of the pin is around $100\ MPa$ or the safety coefficient is equal or greater than two. The thickness of the lug (e_2) was predefined as $10\ mm$, and the height (h) and width (b) are a function of the rod end inner (d) and outer (d_2) diameters.

$$t_1 = 1.5 \cdot d \Rightarrow h = t_1 + \left(\frac{d_2}{2} + 2\right) \qquad \text{(Eq. 8.1)}$$

$$t_2 = 1.5 \cdot d \Rightarrow b = 2 \cdot t_2 \qquad \text{(Eq. 8.2)}$$

By modelling the pin as a beam (Eq. 7.12 – 25), the dimensions of the rod end were changed until the diameter (d) and thickness (e_1) were found, in which the safety coefficient was greater than two (Table 8.1). Comparing theoretical (orange) and analytical (green) data for the final design, two important issues can be observed. Firstly, the analytical and theoretical shear stresses for $x = x_B, x_C$ are quite different. As explained in section 7.1.3.2 this is due to the contact connection. Secondly, the analytical and theoretical bending stresses for $x = x_{1/2}$ are approximately the same. In this case, contact connection does not alter the values because there is a defined tolerance of $2\ mm$.

In conclusion, the selected male threaded rod end is the one of $d = 25\ mm$ and $e_1 = 31\ mm$. It needs maintenance because the bearing shell is made of bronze instead of PTFE, a material not resistant to radiation. The rest of the components are made of stainless steel. Below, in Figure 8.3, other important characteristics can be checked, like the static basic load [24].

$d =$	25 H7 mm
$A =$	22 mm
$B = e_1 =$	31 mm
$d_1 =$	29.6 mm
$d_2 =$	60 mm
$d_3 =$	M24 x 2 FG
$l_1 =$	57 mm
$l_2 =$	124 mm
$l_3 =$	94 mm
Static basic load =	118 kN
Permissible rpm =	440
Mass =	600 g
Angle of misalignment =	15 °
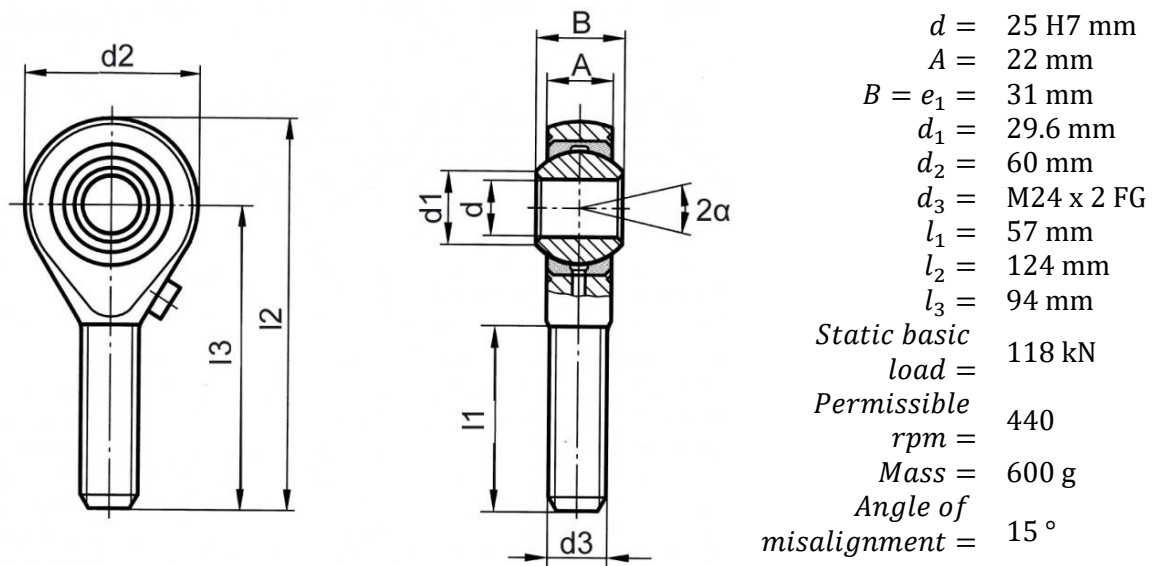
Figure 8.3: Rod end characteristics [mbo]

8.1.2.2. Drawing Description

Base plates
In Annex D.2.1, the drawing of the base plates is shown. For every intermediate hinged wedge, it will be necessary to mill two bases from a block of stainless steel. The original volume of the base was preserved ($300\ mm \times 32.5\ mm \times 150\ mm$).

On one side, six lugs of two different thicknesses (10 mm and 20 mm) were added to place four arms. The dimensions of the lug are (Eq. 8.1-2): $d = 25\ mm$, $t_1 = 37.5\ mm$, $h = 69.5\ mm$, $t_2 = 37.5\ mm$ and $b = 75\ mm$. They are spaced 35 mm so that the rod ends have a misalignment angle of 8°.

On the other side, eight holes of diameter 18 mm were drilled to place two pins and six M16 Allen bolts. The holes drilled with a high-quality tolerance are for the pins, as they have to fit tightly to position and bear the stresses. The holes for the bolts have a bigger diameter because the screws must join the wedges to the back disc and back flange without suffering any stress. The hole layout is the most optimal for clearance and pin placement.

Arms
In Annex D.2.2, the drawing of the arms is shown. For every intermediate hinged wedge, it will be necessary to lathe four of them from a 33 mm hexagonal stainless steel bar. The size of the bar was calculated so that the stress on the arm did not exceed $200\ MPa$ in the assembly position (Figure 8.4). The height was estimated based on the total height of the wedge ($316.5\ mm$), the length of the rod end's thread ($l_1 = 57\ mm$) and the thickness of the locknut ($12\ mm$). Two threads, one right-handed and the other left-handed, will house the rod ends. This system allows to thread both rod ends at the same time. To ensure their position and the total height of the wedge two locknuts per arm will be added [25]. The relief groove of $10\ mm$ facilitates the machining of the threads.

$$\sigma = \frac{F}{S} \cdot SF$$

$$\sigma = \frac{\dfrac{200e + 003 \cdot 9.81}{12 \cdot 4}}{\dfrac{3\sqrt{3} \cdot 19^2}{2} - \pi \cdot 13.5^2} \cdot 1.6$$

$$\sigma = 179\ MPa$$

(Eq. 8.3)
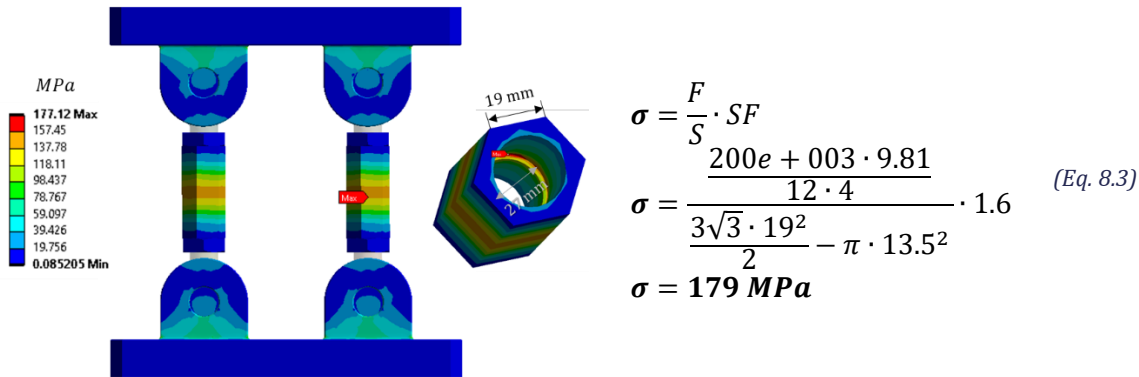
Figure 8.4: Maximum equivalent stress in the assembly position [ANSYS]

Pins / bolts with groove
In Annex D.2.3, the drawing of the bolts with groove is shown. For every intermediate hinged wedge, it will be necessary to lathe four of them from a 32 mm round stainless steel bar. All the dimensions and tolerances, except for the lengths of the pin, are the same as those of a model for sale in the same store where the rod ends will be purchased [26]. These dimensions ($110\ mm$ and $116.5\ mm$) were modified according to how much the lugs are spaced.

Finally, it will be necessary to buy four retaining rings to fix the bolts [27].

Table 8.1: Rod end sizing assuming a $F_{s/2} = 25000\ N$

Dimensions					Boundary conditions				Stresses results									SF
									$x = x_B, x_c$, $M_z = M$, $T_y = R_b = \frac{pb}{2}$				$x = x_{s/2}$, $M_z = M_{max}$, $T_y = 0$				
$d\,[mm]$	$e_1\,[mm]$	$e_2\,[mm]$	$a\,[mm]$	$b\,[mm]$	$p\,\frac{N}{mm}$	$M\,[N\cdot m]$	$M_{max}\,[N\cdot m]$	$q\,\frac{N}{mm}$	$\sigma^+_{x,\,bending}\,\frac{N}{mm^2}$	$\sigma^-_{x,\,bending}\,\frac{N}{mm^2}$	$\tau_{xy,\,shear}\,\frac{N}{mm^2}$	$\sigma_{eq}\,\frac{N}{mm^2}$	$\sigma^+_{x,\,bending}\,\frac{N}{mm^2}$	$\sigma^-_{x,\,bending}\,\frac{N}{mm^2}$	$\tau_{xy,\,shear}\,\frac{N}{mm^2}$	$\sigma_{eq}\,\frac{N}{mm^2}$	
16	21	10	2	8	-3125	-33333	-98958	1190	83	-83	-83	166	246	-246	0	246	0.84
18	23	10	2	8	-3125	-33333	-105208	1087	58	-58	-65	128	184	-184	0	184	1.13
20	25	10	2	8	-3125	-33333	-111458	1000	42	-42	-53	101	142	-142	0	142	1.46
22	28	10	2	8	-3125	-33333	-120833	893	32	-32	-44	82	116	-116	0	116	1.79
25	31	10	2	8	-3125	-33333	-130208	806	22 / 19	-22 / -13	-34 / -11	63 / 27	85 / 85	-85 / -79	0 / 2	85 / 85	2.44 / 2.43

8.2.   Building Process and Assembly

8.2.1.   Fixed Version

The fixed version of the intermediate wedges must be manufactured with a numerical control milling machine. Excess material has to be removed from a titanium alloy block of dimensions $300 \ mm \times 316.5 \ mm \times 150 \ mm$.

8.2.2.   Hinged Version

The hinged version of the intermediate wedges will result from the assembly of six geometries. Three of them will be purchased (rod ends, locknuts and retaining rings) and the rest will be machined (base plates, arms and pins). In Figure 8.5 an exploded view of the hinged version can be seen. Firstly, the rod ends will be housed in the arms. Secondly, this group will join the bases thanks to the pins.
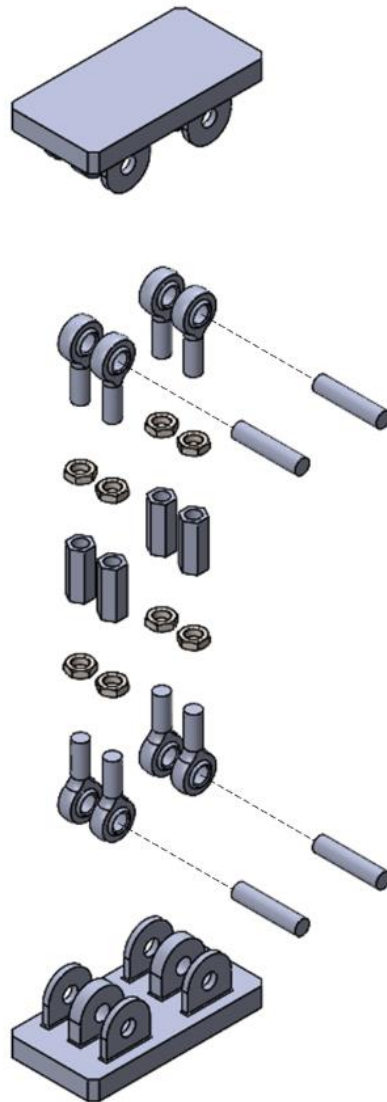
Figure 8.5: Exploded view of the hinged version

8.3.   Time Planning

This project has been developed during a year, from the beginning of March 2021 until the end of February 2022. This period only fully covers the design phase. The rest (prototyping & testing, production and assembly) will not be described in the thesis because they are not listed as objectives in section 2.3.

The design phase includes different tasks. Firstly, fundamental research about CERN, LHC, HL-LHC, CMS and HGCal was done. Secondly, the problem was defined, and the original model and preliminary design were studied. The design optimisation was carried out for several months and multiple proposals were developed and compared. To conclude, the study was focused on the final design, its result analysis and building process.

All this information is included in the thesis, written in two periods. At the beginning of the project, in parallel with the tasks of "Research and documentation" and "ANSYS model study and initial result analysis". At the end, right after the "Final design study".

Figure 8.6 represents a Gantt chart that contains the start and end dates for each phase of the project. In the case of the design phase, the periods in which the different tasks are carried out have also been specified.
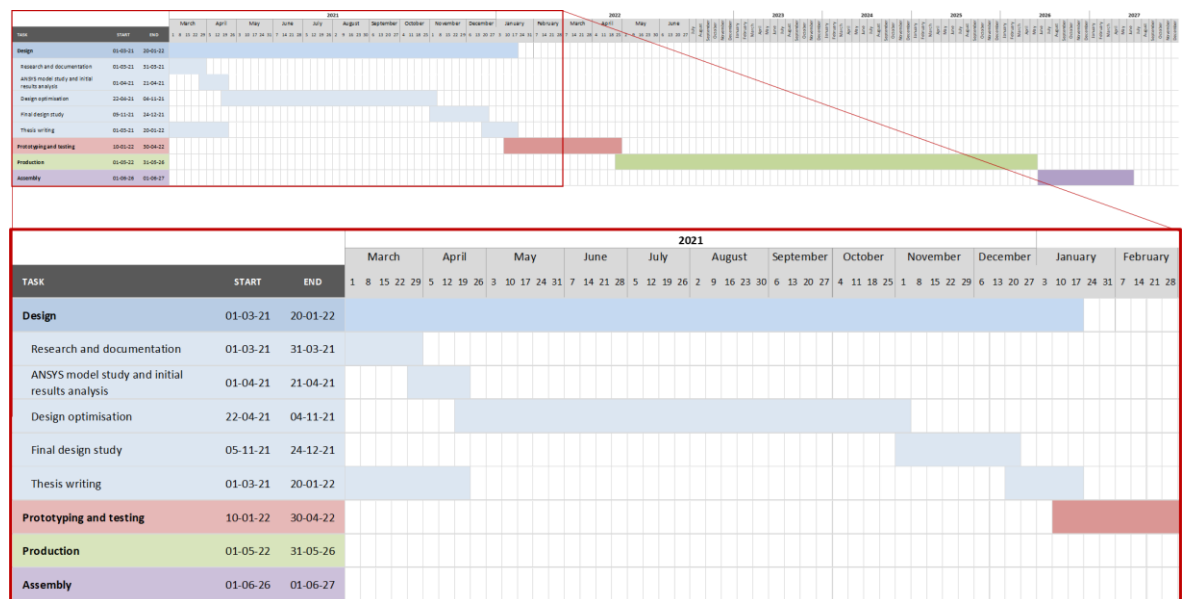
Figure 8.6: Gantt chart of the time planning

8.4.   Budget

At the time of the submission of this thesis, the project is still in the design phase. It means it is still a proposal that has to be approved and it is out of the competences of the designer to look for a company that manufactures the pieces (CERN only works with specific companies that guarantees their standards). Therefore, the cost of the project will be reduced to the cost of the study carried out by the engineer. In this case he/she is a Technical Student and his/her salary [28] is $3319 \frac{CHF}{month} \approx 20 \frac{\text{€}}{h}$ (Eq. 8.4).

$$3319 \frac{\cancel{CHF}}{\cancel{month}} \cdot 0.96 \frac{\text{€}}{\cancel{CHF}} \cdot \frac{1}{20} \frac{\cancel{month}}{\cancel{laborable\ day}} \cdot \frac{1}{8} \frac{\cancel{laborable\ day}}{h} \approx \mathbf{20\ \frac{\text{€}}{h}} \qquad (Eq.\ 8.4)$$

As it can be seen in Table 8.2-4, most of the cost of the design phase is spent on the designer's fees. However, there are also costs related to the hardware (personal computer and screen) and software (academic/ annual licenses). Finally, the total cost is 36,150 €.

Table 8.2: Human resources budget

Concept	Price/hour (€/h)	Time (h)	Cost (€)
Research and documentation	20.00	144	2,880.00
Simulation and development	20.00	1256	25,120.00
Writing	20.00	344	6,880.00
Total		**1744**	**34,880.00**

Table 8.3: Hardware and software budget

Concept	Unit cost (€/u)	Units	Cost (€)
Personal Computer (HP 840 G7 i5)	766.52	1	766.52
Screen (27" Philips)	256.49	1	256.49
SolidWorks® 2021 (Academic use)	87.13	1	87.13
ANSYS Workbench® 2020 R2 (Academic use)	0.00	1	0.00
Microsoft Office® (Annual license)	159.95	1	159.95
Total			**1,270.09**

Table 8.4: Total budget of the design phase of the project

Item	Cost (€)
Human resources	34,880.00
Tools	1,270.09
Total	**36,150.09**

8.5. Environmental Impact and Sustainability

In the next chapter, the machines considered in this project for manufacturing the pieces (mill and lathe) will be environmentally analysed. To carry out the analysis, the Life Cycle Analysis methodology (LCA) has been selected. It consists of carrying out a material and energy balance of the study system, analysing its life cycle.

To characterize the system, four stages have been defined:

- **Manufacture**. Considers the material (raw and recycled) used in the manufacture of the machines. Therefore, in the "End of life" phase, the impact of recycling these materials will not be taken into account.
- **Distribution**. Includes the energetic cost of the transport used to distribute the machines.
- **Use / maintenance**. Includes compressed air, cutting fluids and energy consumption.
- **End of life.** It is difficult to estimate the years of life of a machine, because it can be resold, remodelled, updated, etc. Therefore, only metals and plastics' recycling should be considered. Nevertheless, as already mentioned, this has been already taken into account in the manufacturing phase.

To determine the environmental impact of the system, seven environmental indicators must be taken into account:

- **Abiotic Depletion Potential (ADP)** in *Kg Sb eq*. Refers to the depletion of non-living (abiotic) resources such as fossil fuels, minerals, clay and peat.
- **Acidification Potential (AP)** in *Kg SO_2 eq*. Measures the effect of acid deposition resulting from the release of nitrogen and sulphur oxides in the atmosphere, soil and water.
- **Eutrophication Potential (EP)** in *Kg PO_4 eq*. Increased biomass production in aquatic ecosystems due to a high level of macronutrients, nitrogen and phosphorus. This induces a decrease in the oxygen content.
- **Global Warming Potential (GWP100)** in *Kg CO_2 eq*. Long-term increase in the average temperature of the Earth due to the rise of greenhouse gases (CO_2, CH_4, N_2O, and fluorinated gases). A period of 100 years is generally used.
- **Ozone Layer Depletion Potential (ODP)** in *Kg CFC-11 eq*. Involves the increase in UV-B radiation, that affects human health, environment and natural resources.
- **Human Toxicity Potential (HTP)** in *Kg 1.4 – DB eq*. Potential harm of a unit of chemical released into the environment. Includes both inherent toxicity and generic source-to-dose relationships for pollutant emissions.
- **Photochemical Ozone Creation Potential (POCP)** in *Kg C_2H_4 eq*. Impact category that accounts for the formation of ozone at the ground level of the troposphere caused by photochemical oxidation of Volatile Organic Compounds (VOCs) and carbon monoxide (CO) in the presence of nitrogen oxides (NOx) and sunlight. High concentrations of ground-level tropospheric ozone damage vegetation, human respiratory tracts and manmade materials through reaction with organic materials.

Below, the results for the milling and lathing machines will be analysed.

8.5.1.　Milling Machine

From the values in Table 8.5 and the graph in Figure 8.7, it can be observed that, on average, an 83.3% of the environmental load is originated in the "Use" stage. This means that the main environmental impact is electricity consumption.

All the values in Table 8.5 originate from a study carried out by the "*Sociedad Pública de Gestión Ambiental*" (IHOBE) in the Basque Country [29].

Table 8.5: Environmental impact contribution of the milling machine [IHOBE]

| Potentials		Units	Total	Contribution (%) of each life stage			
				Manufacture	Distribution	Use	End of life
Abiotic Depletion	(ADP)	Kg Sb eq.	5.74E+03	9.5%	2.2%	88.4%	0.0%
Acidification	(AP)	Kg SO$_2$ eq.	3.52E+03	6.5%	3.4%	90.1%	0.0%
Eutrophication	(EP)	Kg PO$_4$ eq.	2.46E+02	13.3%	6.3%	80.3%	0.1%
Global Warming (100 years)	(GWP100)	Kg CO$_2$ eq.	8.09E+05	7.4%	0.7%	91.9%	0.0%
Ozone Layer Depletion	(ODP)	Kg CFC -11 eq.	3.69E-02	5.1%	9.5%	85.4%	0.0%
Human Toxicity	(HTP)	Kg 1.4 - DB eq.	1.50E+05	25.4%	3.3%	71.2%	0.0%
Photochemical Ozone Creation	(POCP)	Kg C$_2$H$_4$ eq.	1.66E+02	21.6%	2.7%	75.7%	0.0%
			Mean	**12.7%**	**4.0%**	**83.3%**	**0.0%**
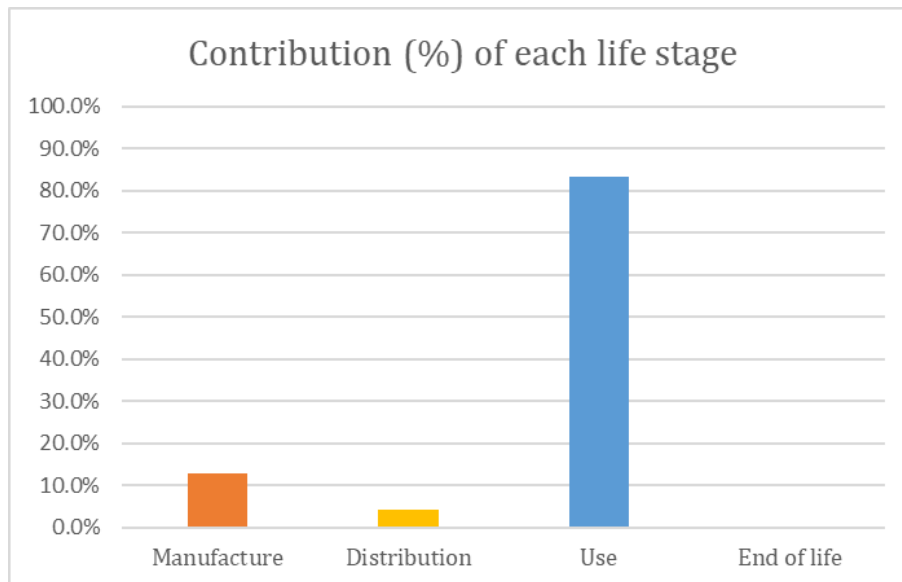
Figure 8.7: Environmental impact contribution regarding the distribution of the milling machine [IHOBE]

ETSEIB

8.5.2. Lathing Machine

From the values in Table 8.6 and the graph in Figure 8.8, it is observed that, on average, a 96.2% of the environmental load is originated in the "Use" stage. Again, this means that the main environmental impact is electricity consumption.

All the values in Table 8.6 originate from a study carried out by the "*Sociedad Pública de Gestión Ambiental*" (IHOBE) in the Basque Country [29].

Table 8.6: Environmental impact contribution of the lathing machine [IHOBE]

| Potentials		Units	Total	Contribution (%) of each life stage			
				Manufacture	Distribution	Use	End of life
Abiotic Depletion	(ADP)	Kg Sb eq.	3.28E+03	2.4%	0.6%	97.0%	0.0%
Acidification	(AP)	Kg SO_2 eq.	2.10E+03	1.6%	0.7%	97.8%	0.0%
Eutrophication	(EP)	Kg PO_4 eq.	1.55E+02	3.2%	1.3%	95.5%	0.0%
Global Warming (100 years)	(GWP100)	Kg CO_2 eq.	5.13E+05	1.7%	0.2%	98.1%	0.0%
Ozone Layer Depletion	(ODP)	Kg CFC -11 eq.	2.09E-02	1.2%	2.5%	96.2%	0.0%
Human Toxicity	(HTP)	Kg 1.4 - DB eq.	1.32E+05	4.0%	0.6%	95.5%	0.0%
Photochemical Ozone Creation	(POCP)	Kg C_2H_4 eq.	8.77E+01	6.0%	0.7%	93.3%	0.0%
			Mean	2.9%	0.9%	96.2%	0.0%
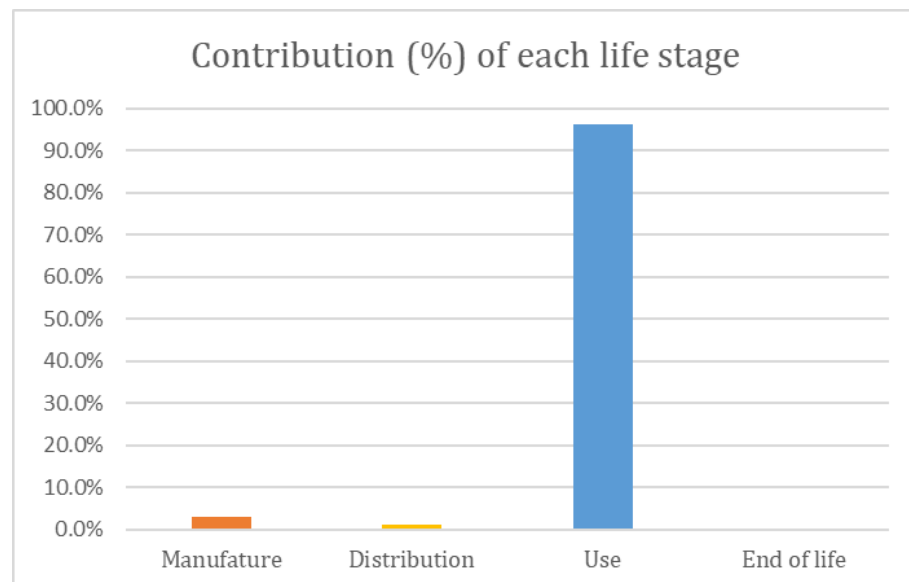
Figure 8.8: Environmental impact contribution regarding the distribution of the lathing machine [IHOBE]

9. Interpretation and Conclusion

In the last chapter of the thesis, the results will be discussed in relation to the initially proposed objectives. In addition, several tasks of the following stages of the project will be described.

9.1.   Achieved Objectives

To focus the study, at the beginning of the project, the functionality of the CMS and the HGCal were described. This allowed defining the problem, including the basic functions, operating mechanics, general requirements, regulations, and maximum permissible forces. Among others, the intermediate wedges must withstand a mass of 200 tons and 50 °C of thermal difference, maintaining parallelism between the back disk and the back flange.

Coming up next, the preliminary design, and the original and isolated ANSYS models were studied. From the obtained results, several landmarks were observed. Firstly, while evaluating the maximum displacement under nominal load, it was noticed that the maximum offset (2.633 mm) was mainly due to the thermal condition. Secondly, thanks to the principal and equivalent stress distributions, it was verified that the maximum value (290 MPa) was concentrated around the fillet radius. For working with titanium, this result was meeting the given requirements. However, if we wanted to move to stainless steel, a cost-efficient and better insulating material, this value had to be optimised. Thirdly, by checking the reaction forces, it was calculated that the vertical load supported by the main wedges (3 & 9) represented the 64.5% of the total weight. One of the optimisation goals was to increase this number, decreasing the action of the weight on the intermediate wedges. Finally, the thermal and buckling analyses revealed that the heat transfer was small enough and the fixed version of the intermediate wedges will never buckle.

Consequently, during the optimisation process, the main goal was to find an optimal configuration in which the stresses and vertical load values lowered. Comparing four different versions of the intermediate wedges, it was proven that a hybrid configuration of hinged (near 3 & 9 o'clock) and fixed intermediate wedges increased the load of the main wedges by 12%. Additionally, both versions were optimised separately to improve the stresses maximum values. On the one hand, it was achieved to reduce the maximum stress value by 16% in the fixed version. On the other hand, the hinged version has been designed with stainless steel instead of titanium because the maximum stress turned out to be 96 MPa. At the end, the final versions of the fixed and hinged intermediate wedges were thoroughly analysed and several drawings were produced.

In conclusion, throughout this year I have developed a big variety of mechanical design engineering skills. On one side, I have always worked independently, leading the project organisation. My supervisor, Hubert Gerwig, settled the ideas and trials and I solely contacted him, some professors or colleagues when I had a problem or needed to make an important choice. On the other, I have produced 32 configurations of intermediate wedges, 12 ANSYS models and 19 types of FEA linear / non-linear analyses. In total, this numbers are translated into 178 CAD models, 21 drawings and 330 FEA analyses.

9.2.   Next Steps

The next steps to be taken consist of contacting different machining workshops and selecting the one that meets the required quality standards and offers a cost-efficient price to manufacture a prototype for the hinged version. Later, the piece has to pass a tensile test to validate the simulation results. In the case of the fixed version, no prototype is needed since testing would be difficult.

Moreover, the replacement of the 12 & 6 o'clock sliding wedges by the fixed version made of titanium can be studied. This will lower assembly costs and complexity.

To sum up, a lot of challenges are still ongoing and I will have the pleasure of participating in several of them. Optimisation is a never ending process of improving but once the design goals have been achieved, the results of the mechanical analyses presented in this thesis, pave the way for the construction of future prototypes for the real operation in the CMS.

Bibliography

[1]   V. Christianto and F. Smarandache, "Thirty Unsolved Problems in the Physics of Elementary Particles," *Progress in Physics,* vol. 4, pp. 112-114, October 2007.

[2]   CERN, "High-Luminosity LHC," 2021. [Online]. Available: https://home.cern/science/accelerators/high-luminosity-lhc. [Accessed 9 Mar. 2021].

[3]   M. Dodgson, D. M. Gann and A. Salter, "The Impact of Modelling and Simulation Technology on Engineering Problem Solving," *Technology Analysis & Strategic Management,* vol. 19, no. 4, pp. 471-489, July 2007.

[4]   N. J. Mourtos, "Defining, Teaching, and Assesing Engineering Design Skills," *International Journal of Quality Assurance in Engineering and Technology Education,* vol. 2, no. 1, pp. 14-30, January-March 2012.

[5]   CERN, "About CERN," 2021. [Online]. Available: https://home.cern/about. [Accessed 9 Mar. 2021].

[6]   CERN, "The Large Hardron Collider," 2021. [Online]. Available: https://home.cern/science/accelerators/large-hadron-collider. [Accessed 9 Mar. 2021].

[7]   M. Brice, "Structurae," 2008. [Online]. Available: https://structurae.net/fr/ouvrages/large-hadron-collider-lhc. [Accessed 9 Mar. 2022].

[8]   CERN, "CMS detector," 2021. [Online]. Available: https://cms.cern/detector. [Accessed 10 Mar. 2021].

[9]   P. A. e. al., "The Phase-2 Upgrade of the CMS endcap calorimeter," Meyrin, 2018.

[10]   JRC European Commission, "EN 1993: Design of steel structures," 2021. [Online]. Available: https://eurocodes.jrc.ec.europa.eu/showpage.php?id=133. [Accessed 3 Mar. 2021].

[11]   *Eurocode 3 - Design of steel structures - Part 1-5: Plated structural elements,* EN 1993-1-5, 2006.

[12]   *Eurocode 3 - Design of steel structures - Part 1-4: General rules - Supplementary rules for stainless steels,* EN 1993-1-4, 2006.

[13]   *Eurocode 3 - Design of steel structures - Part 1-8: Design of joints,* EN 1993-1-8, 2005.

[14]   *Eurocode - Basis of structural design,* EN 1990:2002+A1, 2005.

[15]   3D_HUBS, "The Complete Engineering Guide. CNC Machining," 2021. [Online]. Available: https://www.3dhubs.com/guides/cnc-machining/#getting-started. [Accessed 29 Mar. 2021].

[16] B. Eccles, "The basics of bolted joints," Fastener + Fixing Magazine, Hertfordshire, UK, November 2011.

[17] ANSYS, "Contact Definition," 2021. [Online]. Available: https://ansyshelp.ansys.com/account/secured?returnurl=/Views/Secured/corp/v202/en/wb_sim/ds_Contact_Definition.html. [Accessed 6 Apr. 2021].

[18] ANSYS, "Fixed Supports," 2021. [Online]. Available: https://ansyshelp.ansys.com/account/secured?returnurl=/Views/Secured/corp/v202/en/wb_sim/ds_Fixed_Supports.html?q=fixed%20support. [Accessed 6 Apr. 2021].

[19] Educate, "Saint Venant's principle," 2020. [Online]. Available: https://educatech.in/saint-venants-principle/. [Accessed 10 Apr. 2021].

[20] R. Christensen, "Failure Criteria," 13 June 2019. [Online]. Available: https://www.failurecriteria.com/misescriteriontr.html. [Accessed 16 Apr. 2021].

[21] UA, *ANEJO: Prontuario básico de estructuras simples,* Alicante: UA, 2009.

[22] ISO, *ISO 2768-1,* Genève: ISO, 1989.

[23] ISO, *ISO 2768-2,* Gèneve: ISO, 1989.

[24] mbo, "Shop. Rod ends / Pivoting bearing. Rod ends K series needs maintenance," 2022. [Online]. Available: https://www.mbo-osswald.de/en/shop/rod-ends-din-iso-12240-4-din-648-k-series-high-performance-version-stainless-steel-male-thread/185564812025000. [Accessed 4 Jan. 2022].

[25] mbo, "Shop. Accessories. Nuts," 2022. [Online]. Available: https://www.mbo-osswald.de/en/shop/nuts-din-439/180004390024000. [Accessed 7 Jan. 2022].

[26] mbo, "Shop. Bolts (suitable for clevises)," 2022. [Online]. Available: https://www.mbo-osswald.de/en/shop/bolts-with-groove-for-retaining-rings-din-471-suitable-for-clevises/107943050025000. [Accessed 7 Jan. 2022].

[27] mbo, "Shop. Retainers. Retainers for shafts with groove," 2022. [Online]. Available: https://www.mbo-osswald.de/en/shop/retaining-rings-din-471/100004710250000. [Accessed 7 Jan. 2022].

[28] CERN, "Salary conditions and career progression," [Online]. Available: https://careers.cern/salary-conditions-and-career-progression. [Accessed 8 Jan. 2022].

[29] IHOBE, "Capítulo 3. Diagnóstico ambiental del sector," in *Guías sectoriales de ecodiseño. Máquina herramienta*, Bilbao, Basque Country, IHOBE, 2010, pp. 27-32.

.